POLITECNICO DI TORINO

Master's Degree in Communications and Computer Networks Engineering (CCNE)

Master's Degree Thesis

Advanced signal processing techniques for GNSS signals quality analysis

Supervisors

Prof. Fabio DOVIS

Dr. Alex MINETTO

Dr. Andrea NARDIN

Candidate

Lorenzo SCIACCA

July 2024

Summary

Global Navigation Satellite System (GNSS) is expected to play a growing role in enhancing the autonomy of space missions by providing positioning and timing information to spacecraft. However, when operating at significant distances from Earth, such as for example throughout Moon Transfer Orbits (MTOs), GNSS signals are typically faint. Therefore, ensuring the reliable acquisition and tracking of the GNSS signals becomes a pressing concern.

This work investigates and implements signal processing techniques to evaluate and visualize distortions in ranging signals with a low signal-to-noise ratio (SNR), focusing on processing short batches of signal samples. Specifically, this thesis aims to introduce some techniques to visualize the shape of the chips, of the periodic Direct Sequence Spread Spectrum (DSSS) ranging codes utilized in GNSS, in the time domain. In particular, it is introduced the implementation of a technique capable of enhancing the observability of the ranging codes also when only short batches of signal samples are available. This will be done by reducing the effects of the noise on the signal by averaging several code epochs together, exploiting the periodic nature of the ranging codes utilized in GNSS. It is important to clarify, that the techniques discussed in this work are not designed to enhance receiver sensitivity. These methods are not signal preconditioning techniques intended to facilitate the acquisition or tracking of the signal. Indeed, to obtain the desired signal observables, it is necessary to evaluate the Doppler shift values and the code phase in advance. Receiver sensitivity can be enhanced through proper high-sensitivity techniques. In this thesis, the implementation of an acquisition stage capable of performing high-sensitivity acquisition in extreme environments is also discussed.

The power of the noise experienced by a typical GNSS receiver on the surface of the Earth is about 4,000 times greater than the power of the signal, within a 20 MHz bandwidth. Such a receiver incorporates an acquisition stage based on a correlator. The acquisition stage conducts searches in both the Doppler and code shift domains. The values of the shift of the received code relative to the local code, along with the Doppler shift that results in the largest correlation peak, can be considered estimates of these quantities. This method typically allows to deal

with low values of SNR by extending the coherent integration time, so the length of the correlated sequences. The correlator is utilized in a GNSS receiver to get a first approximation of the Doppler and delay values, prompting these quantities to the tracking stage, that will exploit multiple correlators to track the code shift and the Doppler values.

Signal distortions can alter the shape of the correlation peak, resulting in inaccurate evaluations of the aforementioned parameters. Although the correlation peak is directly involved in the measurements performed by GNSS receivers, studying the shape of the received signal's code, instead, may provide a more effective analysis of the signal distortion, as described in [1].

The application of GNSS for space missions, especially lunar exploration, is still largely unexplored. While GNSS technology has advanced for terrestrial and near-Earth use, its effectiveness and challenges for lunar missions are still being studied. The upcoming Lunar GNSS Receiver Experiment (LuGRE) aims to be the first to test GNSS navigation feasibility in lunar transfer orbit and on the lunar surface. The LuGRE mission is a collaborative effort involving NASA (National Aeronautics and Space Administration), the Italian Space Agency (ASI), Qascom, the company responsible for designing and developing the GNSS receiver utilized in the mission, and the NavSAS group of Politecnico di Torino. As part of the Firefly Blue Ghost Mission 1 (BGM1), the LuGRE receiver will demonstrate GNSS based positioning, navigation, and timing on Moon transfer orbit. The spacecraft will transmit observables, including pseudorange, carrier phase, and Doppler measurements, along with short batches of signal samples, to the ground. This will be done without actively assisting in the lunar lander's navigation.

To study short sample batches, lasting only a few hundred milliseconds, it is essential to efficiently process all available data. The proposed process begins with a high-sensitivity acquisition stage that evaluates the Doppler shift, Doppler rate, and data bits modulating the ranging code. The acquisition process can be extended to the entire signal by performing it in chunks. This method, executed with fine frequency resolution, allows for an evaluation of the Doppler shift and Doppler rate of the signal. After demodulating the received signal using a linear chirp to account for the Doppler rate evaluated in the previous step, an averaging process is employed to reduce the impact of noise. By accumulating entire code epochs together, this process produces a single code epoch with an increased signal-to-noise ratio (SNR). From this result it is also possible to extend the averaging to the single chip, by obtaining an estimate of the shape of the chip transition. This last approach can be applied to a vast variety of GNSS signals, anyway the analysis reported in this work focuses mainly on the GPS C/A signal. Additionally, the implementation proposed, differently from the solutions found in literature, does not require to implement a tracking loop to evaluate the Doppler shift over time, this may reduce the complexity of the processing method.

The proposed technique shows promising results, the distortions introduced in the signal are clearly visible, in this thesis are also shown some results obtained by comparing an observable derived from the obtained chip shape estimate with an empirical model. The analysis of the anomalies and the design of a detection mechanism can be the subject for future research, in particular the output of the proposed technique may be employed to identify the nature of the possible distortions affecting and signal, and possibly characterize the cislunar environment. This technique is now integrated into the state-of-the-art GNSS MATLAB receiver developed by the NavSAS group.

Acknowledgements

I would like to express my sincere gratitude to my supervisors, Alex Minetto and Andrea Nardin, for guiding me into this world. Their expertise and support have been invaluable throughout this journey.

I extend my thanks to Professor Fabio Dovis, for his insightful guidance and encouragement. His knowledge and advice have greatly contributed to the completion of this thesis.

A special thanks goes to all the members of the NavSAS group for their precious feedback, which has been instrumental in refining my work. In particular, I am grateful to Mehr Iman Ebrahimi for the precious help with the signal recording.

Lastly, I would like to thank my friends and my parents for their unwavering support and encouragement. Their belief in me has been a constant source of motivation.

Table of Contents

List of Tables IX

List of Figures X

Acronyms XVII

1 Introduction 1
- 1.1 Introduction to Global Navigation Satellite Systems (GNSS) 1
- 1.2 GNSS Architecture 3
  - 1.2.1 Control Segment 3
  - 1.2.2 Space Segment 3
  - 1.2.3 User Segment 3
- 1.3 Radio navigation in GNSS 4
- 1.4 GNSS Signal in Space 9
  - 1.4.1 GPS signals 11
  - 1.4.2 Galileo Signals 14
- 1.5 Signal propagation 17
  - 1.5.1 Doppler 18
  - 1.5.2 Multipath 19
- 1.6 The GNSS receiver 20
  - 1.6.1 The antenna 20
  - 1.6.2 Front end 21
  - 1.6.3 The acquisition stage 22

2 Averaging and Dithering techniques 26
- 2.1 Physical signal integrity 26
- 2.2 Averaging 29
  - 2.2.1 Addressing the Doppler Effect 30
  - 2.2.2 Sampling Strategies: Real-time sampling 32
  - 2.2.3 Sampling Strategies: Dithered Sampling 33
  - 2.2.4 Dithering and Averaging hybridization 36

2.2.5 Chip Domain Observable 38
2.2.6 Chip Domain Observable vs. Correlator 42

3 Averaging technique implementation 46
3.1 GNSS in space 46
3.2 Requirements and architecture 50
3.3 Acquisition stage 51
3.3.1 Coherent integration in presence of bit transitions 52
3.3.2 Acquisition in presence of a large Doppler shift on the code 54
3.3.3 Acquisition in presence of a large Doppler rate 56
3.3.4 Complete acquisition scheme 58
3.4 Data bit removal and Doppler shift estimation 60
3.5 Averaging stage 63
3.6 Chip Domain Observable (CDO) generation 65

4 Experimental results 68
4.1 Averaging Technique: Results 68
4.2 CDO: general results 70
4.3 Two ray multipath simulation 73
4.4 CDO of signals affected by multipath 76
4.5 Method for CDO Analysis 79

5 Conclusions 87

A References 89

List of Tables

1.1 Orbital parameters for some GNSS systems. Data source: ESA [7], U.S. DoD [8], China Satellite Navigation Office [9]. 3
1.2 L1 signal parameters. 12
1.3 Parameters of the signals transmitted on E1. 17

3.1 Parameters of the HEO orbit simulated in [54] 48

4.1 Overview of the datasets acquired with the aforementioned setup. . 76
4.2 Estimated values of C/N0 and f_D for different PRNs. Dataset: A. . 77
4.3 Description of the parameters selected for the generation of the CDO, obtained processing the dataset A. 80

List of Figures

1.1 Graphical illustration of the pseudorange concept. 5
1.2 Representation of the positioning problem involving two transmitters and a user considering the range measurement errors. Source: Navipedia [12] 8
1.3 Positioning Scenarios with Different Satellite Geometries. Source: Navipedia [13] 9
1.4 GNSS frequency bands. Source: ESA [14] 9
1.5 Example of GNSS broadcast signal, not to scale. 11
1.6 GPS C/A parameters visualization. 13
1.7 Simplified GPS modulation scheme. 13
1.8 A representation of the components of a generic BOC modulated signal, not to scale. 15
1.9 A graphical representation of one CBOC period for a) the $E1b$ component and b) the $E1c$ component. T_c represents the chip period. 16
1.10 A graphic detailing the different areas of GNSS coverage. Source: NASA [17]. 18
1.11 A pictorial representation of the multipath effect. 20
1.12 A pictorial representation of the effect of multipath on the correlation peak at the correlator. Source: [18]. 20
1.13 Normalized circular correlation of a GPS C/A code, with its own replica delayed by 512 chips. 23
1.14 The FFT-based correlator. 24
1.15 Example of the CAF obtained correlating a synthetic GPS C/A signal, sampled on 8 bits at 16.368 MHz, whit a local code replica. $C/N0$: 50 dBHz. 25

2.1 Oscilloscope capture of the signal obtained using the Camp Parks antenna in 1993. The C/A and P(Y) code rising edges (top and bottom part of the Figure respectively) of a healthy satellite (SV 26, left) are compared with those of the faulty SV 19 (right). Source: A. Mitelman [28] 27

2.2 Example of comparison between the correlation peak and chip shape of a GPS C/A signal, both in nominal conditions (blue) and in presence of an anomaly in the signal (red). Source: [1] 28
2.3 The code averaging concept, not to scale. 29
2.4 Sampling an ideal code with a sampling frequency which is a integer multiple of the code rate. 33
2.5 Sampling the Doppler shifted code with a sampling rate which is a multiple of the nominal code rate. 34
2.6 Pictorial representation of the Dithered sampling, also known as virtual sampling. 35
2.7 Sample relabeling 37
2.8 Pictorial representation of the averaging process utilizing the code phase bins. All the samples, from different epochs are mapped to the corresponding code phase bins. 39
2.9 Diagram of a possible averaging implementation. 40
2.10 Example of dithered (virtual) sampling. 41
2.11 Pictorial representation of the Chip Domain Observable estimation. In this case only the falling edges of the PRN code are accumulated together. 41
2.12 Pictorial representation of the computation of the correlation value obtained aligning the local code replica a[n] with the received signal r[n]. 43
2.13 Averaging of N_{avg} code epochs and correlation of the averaged output with the ideally shifted local code replica. 44
2.14 Example of difference between the correlation R_{coh}, achieved by extending the coherent integration time to 50 code epochs, and the correlation R_{avg}, obtained by averaging 50 code epochs and then performing the correlation. The input signal is a GPC C/A code affected by noise with $\sigma_n^2 = 10$ 45

3.1 Number of tracked signals (blue), and radial distance (red). Source: [46] 47
3.2 C/N_0 of the received signals as a function of time near apogee. Source: [46] 47
3.3 Estimated Link budget along the LuGRE mission trajectory. Source: [47] 48
3.4 Doppler rate, histogram of the values obtained simulating a HEO orbit. Source: [54]. 49
3.5 Values of Doppler shift vs. time. Simulation of a HEO orbit. Source: [54]. 49

3.6 Simulated Doppler rate for a terrestrial user as a function of the elevation angle θ. Source [55] 49
3.7 Simulated Doppler rate for a airborne user as a function of the elevation angle θ. Source [55] 49
3.8 Doppler shift rate vs. elevation angle θ. Source: [55]. 50
3.9 Diagram of the proposed processing technique. 52
3.10 A graphical representation of the computation of the correlation value obtained when the received signal and the local code replica are ideally aligned in the time domain, but affected by a bit transition. Segments of the signals are highlighted in different colors to indicate data bits with opposite signs. 53
3.11 A graphical representation of the computation of the correlation value obtained when the received signal and the local code replica are ideally aligned in the time domain but exhibiting opposite polarity. The output of the correlator considered in the CAF is typically squared. 53
3.12 Pictorial representation of the circular correlation in presence of bit transitions. The code is represented by blue or green lines indicating bit polarity. The bits are reported in black. 54
3.13 Comparison between the number of possible bits and the reduced set obtained without considering the sign and the circular shift. . . 55
3.14 Visual representation of the correlation value computation process, performed aligning the received signal r[n] and the local code replica a[n] from the beginning, when the received signal has a chip rate lower than the nominal rate due to the presence of the Doppler shift. 56
3.15 Comparison between the correlation function R^2 obtained with and without the code Doppler shift compensation. GPS C/A signal, sampled at 25 MHz, quantized on 8 bits. 57
3.16 Maximum correlation value R^2 for the shown Doppler and Doppler rate values, with resolutions of 2.5 Hz and 10 Hz/s, respectively. The coherent integration time T_{coh} is 60 ms. 59
3.17 Maximum correlation value R^2 for the shown Doppler and Doppler rate values, with resolutions of 2.5 Hz and 10 Hz/s, respectively. The coherent integration time T_{coh} is 100 ms. 59
3.18 Schematic view of the proposed acquisition stage. 60
3.19 Resolution of the sign ambiguity. 61
3.20 Pictorial representation of the search space reduction principle. The green and blue lines, C_1 and C_2, represent the optimal carriers found by the acquisition stage for the first and second signal blocks, respectively. 62

3.21 Demodulation of the whole received signal performed utilizing a linear chirp with initial phase shift $\hat{\phi}_0$. 63
3.22 Graphical representation of the code averaging process. The relabeled samples from different code epochs are overlapped and mapped to the corresponding code-phase bins, the sum of the values in each bin represent the sample of the de-noised code epoch with the corresponding code phase. 64
3.23 Pictorial representation of the chip domain observable generation process starting from a generic input signal s[n]. The red curve represents the sliding mean of the overlapped samples. 65
3.24 Example of a possible chip domain observable obtained processing the output of the code averaging process. The samples of the chip transitions of the code obtained averaging N code epochs are reported in blue, while the sliding mean of the obtained samples is reported in red. Original signal: GPS C/A, Bin width: 0.5 *samples*, sliding window length: 400 samples, f_s of the original signal: 25 MHz, $C/N0$ of the original signal: 60 dBHz. 66

4.1 Real and imaginary component of the first 300 samples of the signal with normalized amplitude, before the processing. 69
4.2 The first 0.03 ms of the average code epoch (GPS C/A 1 ms) obtained as output from the averaging process. Input $C/N0$ = 60 dBHz, T_{acc} = 200 ms, f_s = 25 MHz, f_D = 500 Hz, $f_{D,rate}$ = 0 Hz/s. 69
4.3 The first 0.03 ms of the average code epoch (GPS C/A 1 ms) obtained as output from the averaging process. Input $C/N0$ = 50 dBHz, T_{acc} = 200 ms, f_s = 25 MHz, f_D = 500 Hz, $f_{D,rate}$ = 0 Hz/s. 70
4.4 The first 0.03 ms of the average code epoch (GPS C/A 1 ms) obtained as output from the averaging process. Input $C/N0$ = 50 dBHz, T_{acc} = 600 ms, f_s = 25 MHz, f_D = 500 Hz, $f_{D,rate}$ = 0 Hz/s. 70
4.5 The first 0.03 ms of the average code epoch (GPS C/A 1 ms) obtained as output from the averaging process. Input $C/N0$ = 45 dBHz, T_{acc} = 300 ms, f_s = 25 MHz, f_D = 500 Hz, $f_{D,rate}$ = 0 Hz/s. 71
4.6 Chip domain observable obtained processing the output of the code averaging stage. Original signal: GPS C/A, $C/N0$: 50 dBHz, f_s: 25.575 MHz, T_{acc}: 300 ms, Bin width: 0.5 samples, Doppler shift: 0 Hz 71
4.7 Chip domain observable obtained processing the output of the code averaging stage. Original signal: GPS C/A, $C/N0$: 50 dBHz, f_s: 25.575 MHz, T_{acc}: 300 ms, Bin width: 0.2 samples, Doppler shift: 2500 Hz 72
4.8 Description of the setup utilized to obtain a real GNSS signal. . . . 72

4.9 Chip domain observable, rising edge. Input signal: GPS C/A, PRN 21, f_D ≈ -1180.5 Hz, $C/N0$ ≈ 49 dBHz, f_s: 25 MHz, Bin width: 1 sample, Sliding mean window: 400 samples, $T_{acc} = 300$ ms. 73
4.10 Chip domain observable, rising edge. Input signal: GPS C/A, PRN 3, f_D ≈ 1983 Hz, $C/N0$ ≈ 44 dBHz, f_s: 25 MHz, Bin width: 1 sample, Sliding mean window: 400 samples, $T_{acc} = 300$ ms. 74
4.11 Chip domain observable, rising edge. Input signal: GPS C/A, PRN 22, f_D ≈ -71.3 Hz, $C/N0$ ≈ 38 dBHz, f_s: 25 MHz, Bin width: 1 sample, Sliding mean window: 400 samples, $T_{acc} = 300$ ms. 74
4.12 A visual representation of the expected impact of two-ray multipath on the chip shape. 75
4.13 Setup employed for the multipath injection. 75
4.14 CDO comparison. $f_s = 25$ MHz, ADC: 16 bit, $f_D \approx -1180.5\ Hz$, PRN: 21, Sliding mean window: 400 samples, bin width = 1 sample, $T_{acc} = 300\ ms$. 77
4.15 CDO comparison. $f_s = 12.5$ MHz, ADC: 16 bit, $f_D \approx -1294.5\ Hz$, PRN: 21, Sliding mean window: 400 samples, bin width = 1 sample, $T_{acc} = 300\ ms$. 78
4.16 CDO comparison. $f_s = 5$ MHz, ADC: 16 bit, $f_D \approx -1479.5\ Hz$, PRN: 21, Sliding mean window: 400 samples, bin width = 1 sample, $T_{acc} = 300\ ms$. 78
4.17 CDO comparison. $f_s = 25$ MHz, ADC: 16 bit, $f_D \approx 2431.2\ Hz$, PRN: 17, $C/N0$ ≈ 41.7 dBHz, Sliding mean window: 400 samples, bin width = 1 sample, $T_{acc} = 300\ ms$. 79
4.18 CDO comparison. $f_s = 25$ MHz, ADC: 16 bit, $f_D \approx -71.3\ Hz$, PRN: 22, $C/N0$ ≈ 38 dBHz, Sliding mean window: 400 samples, bin width = 1 sample, $T_{acc} = 300\ ms$. 79
4.19 $\hat{D}$: forward finite difference of the CDO A2, smoothed with a sliding mean with window $Win_D:\ 0.015 \cdot T_{chip}$. 81
4.20 $\hat{D}$: forward finite difference of the CDO A2, smoothed with a sliding mean with window $Win_D:\ 0.025 \cdot T_{chip}$. 81
4.21 $\hat{D}$: forward finite difference of the CDO A2, smoothed with a sliding mean with window $Win_D:\ 0.05 \cdot T_{chip}$. 82
4.22 Comparison between the model $\bar{D}(CDO\ A4)$ and $\hat{D}(CDO\ A4)$. CDO A4, multipath-free. 82
4.23 Comparison between $\hat{D}$, $\bar{D}$ and the residual. CDO A1 84
4.24 Comparison between $\hat{D}$, $\bar{D}$ and the residual when multipath is present. CDO A1M, multipath. 84
4.25 Comparison between $\hat{D}$, $\bar{D}$ and the residual. CDO A2 85
4.26 Comparison between $\hat{D}$, $\bar{D}$ and the residual. CDO A2M, multipath. 85
4.27 Comparison between $\hat{D}$, $\bar{D}$ and the residual. CDO A3. 86

4.28 Comparison between $\hat{D}$, $\bar{D}$ and the residual. CDO A3M, multipath. 86

Acronyms

A-GNSS
  Assisted GNSS

ADC
  Analog to Digital Converter

AGC
  Adaptive Gain Control

ASI
  Agenzia Spaziale Italiana

BDS
  BeiDou Navigation Satellite System

BOC
  Binary Offset Carrier

CAF
  Cross Ambiguity Function

CASM
  Coherent Adaptive Subcarrier Modulation

C/A
  Coarse Acquisition

CBOC
  Composite Binary Offset Carrier

CDMA

Code Division Multiple Access

DSSS

Direct Sequence Spread Spectrum

FFT

Fast Fourier Transform

GEO

Geostationary Orbit

GDOP

Geometric Diluition of Precision

GNSS

Global Navigation Satellite System

GPS

Global Positioning System

GPST

GPS Time

GST

Galileo System Time

HAS

High Accuracy Service

ICAO

International Civil Aviation Organization

IF

Intermediate Frequency

IFFT

Inverse Fast Fourier Transform

IGSO

Inclined Geo-Synchronous Orbit

IOC

Initial Operational Capability

IRNSS

Indian Regional Navigation Satellite System

ITU

International Telecommunication Union

LNA

Low Noise Amplifier

LuGRE

Lunar GNSS Receiver Experiment

MEO

Medium-Earth Orbit

NASA

National Aeronautics and Space Administration

OS

Open Service

PNT

Positioning Navigation and timing

PPS

Precise Positioning Service

PRN

Pseudo Random Noise

PRS

Public Regulated Service

QZSS
: Quasi-Zenith Satellite System

RNSS
: Radionavigation Satellite Service

SAW
: Surface Acoustic Wave

SIS
: Signal In Space

SNR
: Signal to Noise Ratio

SV
: Space Vehicle

TAI
: International Atomic Time

TMBOC
: Time Multiplexed Binary Offset Carrier

TOA
: Time of Arrival

UERE
: User Euivalent Range Error

USNO
: United States Naval Observatory

UTC
: Coordinated Universal Time

VGA
: Variable Gain Amplifier

Chapter 1

Introduction

This chapter introduces the Global Navigation Satellite System (GNSS) and its fundamental working principles. It provides an overview of the GNSS architecture, and the signals utilized for satellite radio navigation. Section 1.1 begins with a brief introduction to the available GNSS systems, followed by a description of their typical architecture. In Section 1.3, the basic principles of radio navigation are explained within the context of the Time of Arrival (TOA) ranging paradigm, along with a detailed overview of the typical GNSS ranging signals. The subsequent section, 1.5, delves into the propagation of GNSS signals. The structure of the thesis is as follows: Chapter 1 introduces the main working principles of GNSS and describes the signals transmitted by GNSS satellites. Chapter 2 reviews the relevant literature and elucidates the key concepts behind the averaging technique. It includes a theoretical comparison of the SNR gain obtained through accumulation methods versus conventional correlation techniques. Chapter 3 details the implementation of the proposed averaging technique, outlining the features of the processing steps involved. Chapter 4 presents the results obtained from processing both synthetic and real GNSS signals using the proposed technique. This chapter also includes the results from emulating multipath effects by combining two real GNSS signals received by different antennas, with one signal propagated through a delay line. Furthermore, the results obtained with the introduction of multipath are compared to those obtained without it.

1.1 Introduction to Global Navigation Satellite Systems (GNSS)

The term radio navigation refers to the process of determining a position or obtaining information related to position for navigation purposes by utilizing the propagation properties of radio waves [2]. Among radio navigation systems, Global Navigation

Satellite Systems (GNSS) provide positioning, navigation, and timing (PNT) services on a global basis. GNSS is a general term for any satellite constellation that offers these services, indeed, there are four GNSS systems available, which are:

- **GPS**: NAVSTAR Global Positioning System; the pioneering GNSS system, was initiated by the U.S. Department of Defense in December 1973 and developed by the U.S. Air Force to provide precise location and timing information globally [3]. Initially intended for military use, the NAVSTAR Global Positioning System expanded its scope to include civilian applications from 1983 onwards [4].

- **Galileo**: the European Union's GNSS system; it operates entirely under civilian authority. In December 2016, Galileo reached the Initial Operational Capability (IOC) phase, marking the start of its provision of initial services [5]. Designed to be interoperable with other GNSS systems, such as GPS, Galileo improves global navigation capabilities and ensures redundancy.

- **GLONASS**: Globalnaya Navigazionnaya Sputnikovaya Sistema; the GNSS system of the Russian federation.

- **BeiDou**: the BeiDou Navigation Satellite System (BDS) was developed by the People's Republic of China over a similar timeframe as Galileo. The BeiDou constellation comprises satellites with three distinct types of orbits: Medium-Earth Orbit (MEO), Inclined Geo-Synchronous Orbit (IGSO), and Geostationary Orbit (GEO). While MEO satellites are utilized by other GNSS systems as well, the inclusion of IGSO and GEO satellites in BeiDou enhances coverage in the Asia-Pacific region.

Furthermore, it is worth mentioning that other regional navigation satellite systems exist, such as the Indian Regional Navigation Satellite System (IRNSS) and the Japanese Quasi-Zenith Satellite System (QZSS), which provide coverage over defined areas.

All the aforementioned systems offer services for civilian use, as well as public regulated and military services. Each type of service can provide varying levels of accuracy, integrity, and robustness against potential threats.

The growing importance of GNSS is evident from the significant increase in both device shipments and installed bases projected over the next decade. Shipments of GNSS devices are expected to rise from nearly 1.6 billion units in 2023 to more than 2.2 billion units by 2033 [6], driven primarily by the Consumer solutions, automotive, and aviation segments.

1.2 GNSS Architecture

Given the structure of the presented systems, a common architectural scheme for GNSS can be identified. This typically includes three segments, which are: Control Segment, Space Segment and User segment.

1.2.1 Control Segment

The Control Segment provides continuous oversight of the satellites, monitoring their status, signal integrity, and orbital configurations. It supplies essential data for system operations to the satellites through a network of tracking stations, which monitor their orbital parameters and health. A master station processes the collected data and manages both satellite operations and the system's time scale. Once the ephemeris data and timing parameters are computed, they are transmitted to the satellites through a network of up-link stations. Multiple stations are present worldwide for redundancy and to ensure coverage.

1.2.2 Space Segment

The space segment comprises a constellation of satellites that deliver positioning services to users. The space segment solely receives data from the control segment; users do not transmit any information back to the GNSS satellites. Positioning relies on the one-way Time of Arrival concept, as described in Section 1.3.

System	GPS	Galileo	Beidou (MEO)
Orbital planes	6	3	3
Inclination Angle	55°	56°	55°
Altitude [km]	20,180	23,222	21,528

Table 1.1: Orbital parameters for some GNSS systems. Data source: ESA [7], U.S. DoD [8], China Satellite Navigation Office [9].

An overview of the orbital parameters of some GNSS systems is provided in Table 1.1.

1.2.3 User Segment

The user segment consists of the receiver and the equipment needed to solve the PVT problem. Typically, the receiver must be able to receive signals from the satellite constellation, decode the navigation message, and process the data to estimate its position. A wide variety of receivers exist; processing may occur within a single device in real-time or across multiple devices. It is also possible to store intermediate products for later enhancement of the solution through post-processing or to perform the entire processing after recording the received signal, for instance, using a Software Defined Radio (SDR).

1.3 Radio navigation in GNSS

The aforementioned systems allow users to determine their position through trilateration, by measuring the distances to various satellites. This process relies on one-way Time of Arrival (TOA) ranging, where the receiver measures the arrival time of signals sent by satellites at known times. The satellites are synchronized with a system time reference, and each system has its own unique time reference; for instance, GPS Time (GPST) is a continuous time scale set by the GPS control segment, and aligned with UTC(USNO). Galileo also has its own time reference, the Galileo System Time (GST), which is a continuous time scale synchronized with International Atomic Time (TAI) with a nominal offset of less than 50 nanoseconds.

The satellites transmit ranging codes and navigation data synchronized with the system time reference. The navigation data allows the receiver to determine the satellite's position at the time of signal transmission, while the ranging code enables the receiver to calculate the signal's transit time and thereby the distance to the satellite. This method requires the user receiver to have an onboard clock. To determine the receiver's three-dimensional location and clock offset from the system time, TOA ranging measurements must be taken from four satellites. Therefore, at least four measurements are essential to accurately calculate the user's position in three dimensions [10].

Given the following quantities:

- T_s: System time at the instant in which the signal started propagating from the satellite
- T_u : System time at which the receiver received the signal
- δt: The satellite clock's offset from system time
- t_u: The offset of the receiver clock from the reference system time
- Δt: The geometric range time equivalent
- c: The speed of light

it is possible to define the range measurement performed by the receiver as:

$$\rho = c(T_u - T_s) + c(t_u - \delta t) \tag{1.1}$$

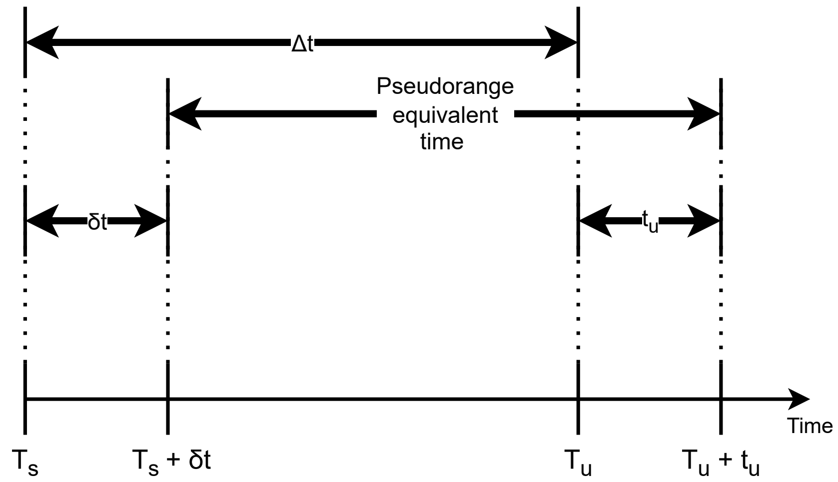

Figure 1.1: Graphical illustration of the pseudorange concept.

In GNSS, the quantity ρ is referred to as *pseudorange*, this measure differs from the geometric range due to the presence of δt and t_u, as reported in 1.1. A graphical representation of the timing relationships is shown in Figure 1.1.

Each satellite is equipped with a high performance atomic clock, anyway an offset δt will be present, this offset is characterized by a bias and a drift component. Thanks to the high stability of the clocks onboard the satellites, ground monitoring stations can accurately predict the value of δt over time. This information is then disseminated by the constellation through the navigation data. Consequently, the receiver can accurately compensate for the offset δt. By repeating this procedure for all pseudoranges, the receiver can process measurements from the visible satellites within a given constellation. Anyway, knowing the measure of the distance between the satellites and the receiver is not enough to determine the receiver position in three dimensions, in fact, the knowledge of the position of the satellites, and of the user clock bias, is necessary to obtain an estimate of the receiver position. While the satellite's position can be computed from the ephemeris contained in the navigation data broadcasted from the constellation or obtained in post-processing, as in the case of the A-GNSS [11], the user clock bias remains unknown. Therefore, it is treated as an unknown in the positioning problem.

Computing the user position in three coordinates (x_u, y_u, z_u) and the fourth unknown t_u, relying solely on GNSS, requires at least four measurements from four different satellites. The resulting system of equation can be expressed as:

$$\begin{cases} \rho_1 = \sqrt{(x_1 - x_u)^2 + (y_1 - y_u)^2 + (z_1 - z_u)^2} + b_{ut} \\ \rho_2 = \sqrt{(x_2 - x_u)^2 + (y_2 - y_u)^2 + (z_2 - z_u)^2} + b_{ut} \\ \rho_3 = \sqrt{(x_3 - x_u)^2 + (y_3 - y_u)^2 + (z_3 - z_u)^2} + b_{ut} \\ \rho_4 = \sqrt{(x_4 - x_u)^2 + (y_4 - y_u)^2 + (z_4 - z_u)^2} + b_{ut} \end{cases} \tag{1.2}$$

where b_{ut} is given by the equation 1.3, and $(x_i,\ y_i,\ z_i)$ refer to the position of the i-th satellite.

$$b_{ut} = ct_u \tag{1.3}$$

The system represented in 1.2 is nonlinear and can be addressed through linearization, specifically by computing a first-order Taylor expansion. An approximate pseudorange can be defined as:

$$\hat{\rho}_i = \sqrt{(x_i - \hat{x_u})^2 + (y_i - \hat{y_u})^2 + (z_i - \hat{z_u})^2} + \hat{b_{ut}} \tag{1.4}$$

where $(\hat{x_u}, \hat{y_u}, \hat{z_u})$ represents the approximate receiver location and $\hat{b_{ut}}$ denotes the estimate of the user time bias. Both the user position and receiver clock offset are considered to consist of an approximate component and an incremental component.

$$\begin{array}{rcl} x_u & = & \hat{x_u} + \Delta x_u \\ y_u & = & \hat{y_u} + \Delta y_u \\ z_u & = & \hat{z_u} + \Delta z_u \\ t_u & = & \hat{t_u} + \Delta t_u \end{array} \tag{1.5}$$

so the pseudorange ρ can be expressed as:

$$\rho = f(x_u, y_u, z_u, t_u) = f(\hat{x_u} + \Delta x_u, \hat{y_u} + \Delta y_u, \hat{z_u} + \Delta z_u, \hat{t_u} + \Delta t_u) \tag{1.6}$$

Performing the Taylor expansion and truncating it at the first order the expression of the i-th pseudorange becomes:

$$\rho_i = \hat{\rho}_i - \frac{x_i - \hat{x_u}}{\hat{r_i}} \Delta x_u - \frac{y_i - \hat{y_u}}{\hat{r_i}} \Delta y_u - \frac{z_i - \hat{z_u}}{\hat{r_i}} \Delta z_u + ct_u \tag{1.7}$$

where the value $\hat{r_j}$ is the geometric range between the linearization point and the j^{th} satellite.

$$\hat{r_j} = \sqrt{(x_j - \hat{x_u})^2 + (y_j - \hat{y_u})^2 + (z_j - \hat{z_u})^2} \tag{1.8}$$

The derived system can then be written as:

$$\Delta\rho = H \cdot \Delta x \tag{1.9}$$

where:

- $$\Delta\rho = \begin{bmatrix} \hat{\rho}_1 - \rho_1 \\ \hat{\rho}_2 - \rho_2 \\ \hat{\rho}_3 - \rho_3 \\ \hat{\rho}_4 - \rho_4 \end{bmatrix}, H = \begin{bmatrix} a_{x1} & a_{y1} & a_{z1} & 1 \\ a_{x2} & a_{y2} & a_{z2} & 1 \\ a_{x3} & a_{y3} & a_{z3} & 1 \\ a_{x4} & a_{y4} & a_{z4} & 1 \end{bmatrix}, \Delta x = \begin{bmatrix} \Delta x_u \\ \Delta y_u \\ \Delta z_u \\ \Delta b_{ut} \end{bmatrix} \tag{1.10}$$

- The values: a_{xj}, a_{yj}, a_{z_j} are the Taylor coefficients

$$a_{xj} = \frac{x_j - \hat{x_u}}{\hat{r_j}}, a_{yj} = \frac{y_j - \hat{y_u}}{\hat{r_j}}, a_{zj} = \frac{z_j - \hat{z_u}}{\hat{r_j}} \tag{1.11}$$

Hence, the solution of the positioning problem is:

$$\Delta x = H^{-1}\Delta\rho \tag{1.12}$$

When the number of available satellites n is larger than 4, then the method of least squares can be used to solve 1.12; multiplying both sides of the expression 1.9 by H^T and then multiplying again both sides of the obtained equation by $(H^T H)^{-1}$, the value of Δx can be determined as:

$$\Delta x = (H^T H)^{-1} H^T \Delta\rho \tag{1.13}$$

The PVT problem can then be solved by starting from a linearization point at the center of the Earth. Typically, an iterative algorithm will converge to a solution within tens of iterations.

To understand how the result is affected by the error in the pseudoranges values, the quantities $\Delta\rho$ and Δx can be expressed as follow:

$$\begin{aligned} \Delta\rho &= \rho_T - \rho_L + d\rho \\ \Delta x &= x_T - x_L + dx \end{aligned} \tag{1.14}$$

So, the quantity $\Delta\rho$ is composed of three components: the vector of the true pseudoranges values ρ_T; the vector of the pseudoranges computed at the linearization point ρ_L; and the vector of the pseudoranges net error $\delta\rho$. The vector Δx can be expressed in a similar way. From 1.14, assuming that the components of $\delta\rho$ are identically distributed, independent, and have a variance equal to the square of the satellite UERE, it follows that :

$$\delta x = (H^T H)^{-1} H^T \delta\rho \tag{1.15}$$

$$cov(\delta\rho) = I_{n\times n}\sigma^2_{UERE} \tag{1.16}$$

$$cov(\delta x) = (H^T H)^{-1}\sigma^2_{UERE} \tag{1.17}$$

where σ^2_{UERE} denotes the variance attributed to the pseudorange measurement error. From the expression 1.17 it emerges that the covariance of δx is proportional to the term $(H^T H)^{-1}$, which depends solely on the geometry of the problem.

In conclusion, an expression of the standard deviation of the positioning error can be obtained as:

$$GDOP \cdot \sigma_{UERE} = \sqrt{\sigma_{x_u} + \sigma_{y_u} + \sigma_{z_u} + \sigma_{b_{ut}}} \tag{1.18}$$

$$GDOP = \sqrt{trace((H^T H)^{-1})} \tag{1.19}$$

Some relevant considerations can be made referring to 1.18, indeed the quality of the final result depends on both the geometry of the problem and on the measurement errors contributing to σ_{UERE}. This implies that, independently on the measurement quality, it may be not possible to reach values of RMSE below a given threshold due to the presence of a high $GDOP$. The $GDOP$ tends to be higher when the geometry of the problem is such that the measurements are not carrying enough information about the user position in one or more dimensions. A graphical representation of the problem is provided in Figure 1.2 and in Figure 1.3. Urban canyons exemplify scenarios with high GDOP. Buildings obstruct the receiver's view, limiting visible satellites to those within a specific portion of the sky and above a minimum elevation angle. This restricted view typically results in a non-optimal satellite geometry.

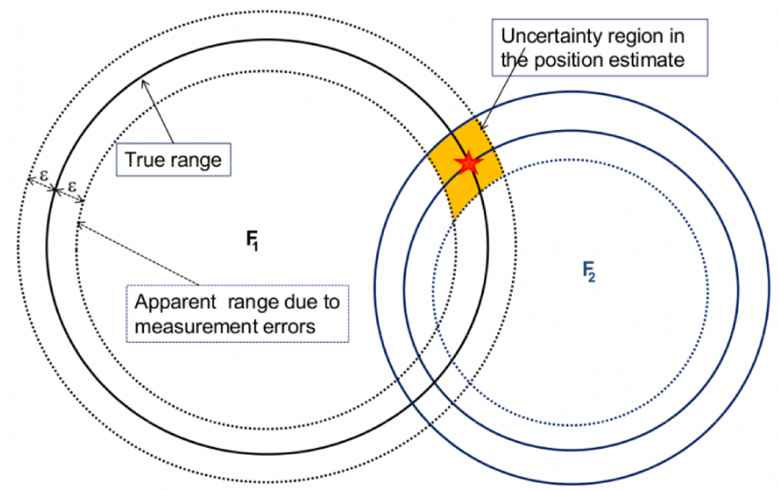

Figure 1.2: Representation of the positioning problem involving two transmitters and a user considering the range measurement errors. Source: Navipedia [12]

.

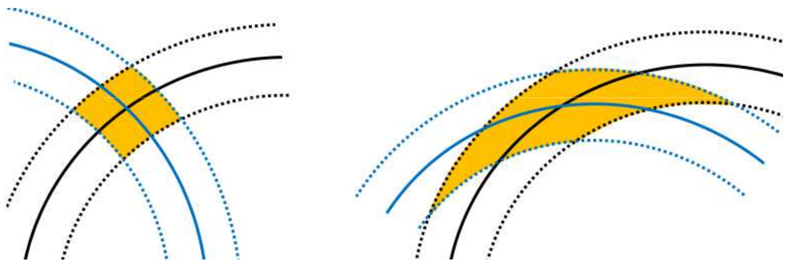

Figure 1.3: Positioning Scenarios with Different Satellite Geometries. Source: Navipedia [13]

.

1.4 GNSS Signal in Space

To perform trilateration, the receiver must process signals transmitted by GNSS satellites within line of sight. These signals are commonly referred to as the Signal in Space (SIS). Over time, specific portions of the spectrum have been allocated for GNSS by the International Telecommunication Union (ITU) for Radionavigation Satellite Service (RNSS) purposes. The upper L-band contains the GPS L1, Galileo E1, GLONASS G1, and BeiDou B1 bands, while the lower L-band includes the GPS L5, GLONASS G3, Galileo E5, and BeiDou B2 bands. A more detailed explanation of the spectrum allocation is shown in Figure 1.4.

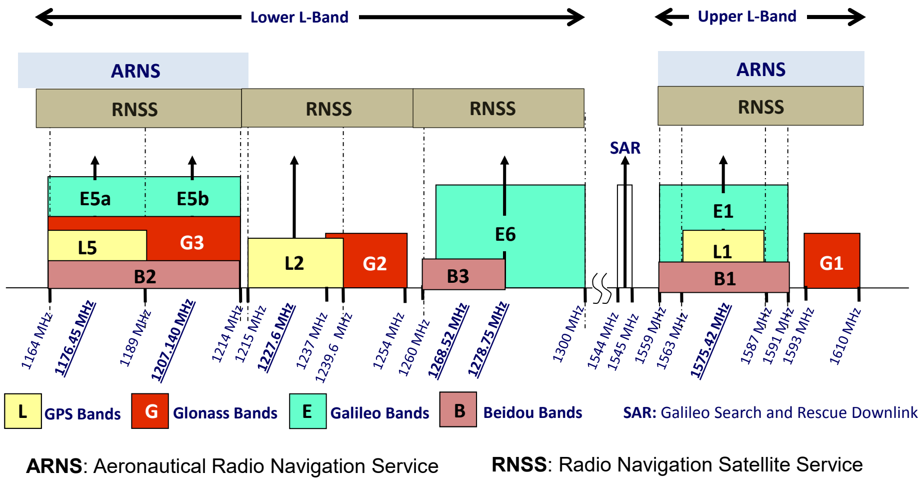

Figure 1.4: GNSS frequency bands. Source: ESA [14]

The majority of GNSS systems share common resources in the frequency domain, primarily due to practical and historical considerations. The first service for civil applications was broadcast by GPS on the L1 band, leading, subsequently, the designers of the Galileo and BeiDou systems to adopt the same carrier frequency in the L1 band. By using the same frequency, receiver manufacturers can leverage existing, reliable technology and intellectual property for the receiver's front-end.

Sharing most of the spectrum with other constellations, the resources are accessed through a CDMA scheme, facilitating each satellite to transmit on one or more carriers and concurrently provide diverse services through them. A common set of components usually present in a GNSS signal can be introduced as follows:

- **Carrier**: The sinusoidal component that modulates the signal at the desired frequency. It usually consists of an in-phase and a quadrature component.
- **Ranging Code**: the binary code sequence utilized by the user for ranging purposes. Each satellite transmits its own set of codes, each of them providing access to a specific positioning service. The codes are usually called PRN codes (Pseudo Random Noise).
- **Navigation data Bits**: In the GNSS signal, the Navigation Data Bits section provides users with essential information for determining their positions accurately. This includes the satellite's pseudo-Keplerian elements, known as ephemeris, and the almanac, containing low-resolution orbital data and predictions for the entire constellation. Additionally, it includes corrections for satellite clock biases and the related parameters.

Among all the components of the SIS, the ranging codes are the most important; the receiver, after the removal of the carrier, can perform the ranging measurements exploiting the properties of the PRN codes. The obtained spread spectrum signal has some interesting properties. For example:

- By using unique PRN sequences from a carefully chosen set, multiple satellites can broadcast signals simultaneously on the same frequency with a reduced interference.
- The selected codes typically exhibit favorable autocorrelation properties, facilitating signal acquisition even in the presence of significantly powerful noise. Simultaneously, they help minimize cross-correlation between the codes of other satellites.
- Using the spreading codes enable better rejection of narrowband interference.

In conventional Direct Sequence Spread Spectrum (DSSS) implementations, a rectangular pulse shape is typically employed. However, with the advent of newer systems such as Galileo, a shift has occurred towards utilizing pulse shaped like segments of square waves. Several key terms are utilized to describe PRN codes. These include:

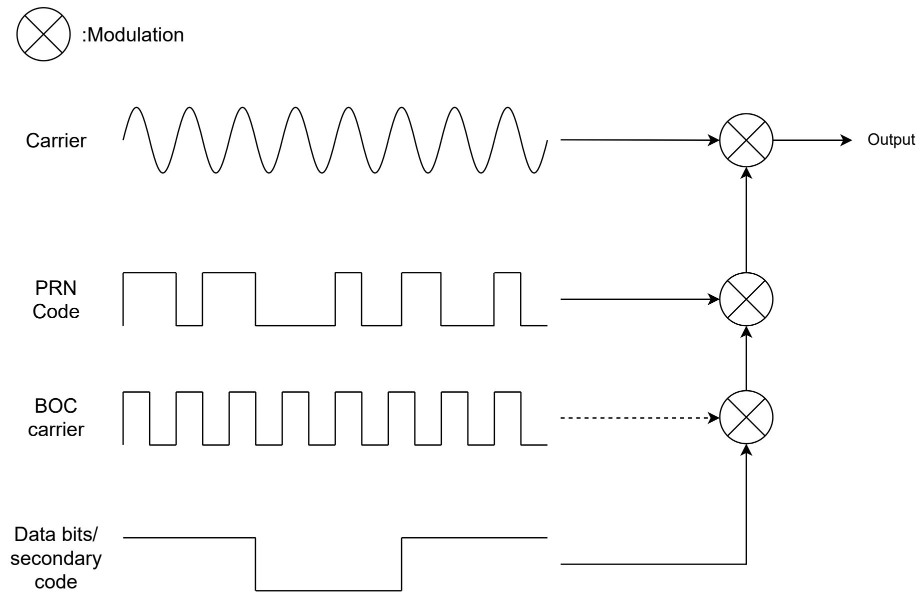

Figure 1.5: Example of GNSS broadcast signal, not to scale.

- **Chip**: This refers to a single element, or bit, within the PRN code sequence.
- **Chip period** T_c: This term signifies the minimum time interval between transitions (changes) in the PRN waveform.
- **Chip Rate** R_c: The chipping rate is the reciprocal of the chip period ($1/T_c$). It represents the rate at which these transitions, occur within the PRN code.

1.4.1 GPS signals

The operations of GPS are divided over three carriers, L1, L2 and L5. The band considered in this work is L1, centered at 1575.42 MHz, it carries primary navigation signals, including the Coarse Acquisition (C/A) code, and military codes as well. Starting from the GPS block III/IIIF, the L1 carrier is also utilized by a new signal for civil application called L1C. Table 1.2 shows some of the key parameters of the services associated to the L1 carrier; for the sake of simplicity the parameters of a fourth service, the military M-code, are not reported.

The C/A (Coarse Acquisition) service provides positioning service to civil users without the need of any kind of authentication; these codes consist of sequences of 1023-chip long Gold codes. Conversely, the Precise Positioning Service (PPS) relies on encrypted P(Y) codes, exclusively reserved for military usage. Originally conceived to assist military users in accessing P codes for precise positioning, the

C/A service ultimately emerged as the primary means for delivering positioning to civilian users worldwide.

A modernized civil signal, L1C, is also modulated by the same carrier at L1, this signal carries two component, a data component similar to the one of the C/A signal and a pilot component. The pilot component consists solely of the ranging codes, in this way the receiver does not have to deal with the extra complexity introduced by the data bits; for instance, the acquisition phase benefits from not having to address the problem of the navigation data. The two components are then modulated using a Binary Offset Carrier (BOC) modulation; more on the BOC modulation can be found in section 1.4.2 while dealing with the Galileo signals. In the context of this study, for what concerns GPS, the focus is directed towards the C/A service.

The GPS L1 signal transmitted by the $i-th$ satellite, without considering the L1C service, can be written as:

$$x_{RF,i}(t) = \sqrt{2P_C}c_i(t)d_i(t)cos(2\pi f_{L1}t+\theta_i)+\sqrt{2P_Y}c_{i,Y}(t)d_i(t)sin(2\pi f_{L1}t+\theta_i) \quad (1.20)$$

where:

- $c_i(t)$: is the C/A code associated to the $i-th$ satellite, clocked at 1.023 MHz.
- $c_{i,Y}$: is the P(Y) code associated to the $i-th$ satellite, clocked at 10.23 MHz.
- d_i: is the navigation data message clocked at 50 bps.
- P_C and P_Y: represent the power values associated with the C/A and P(Y) components, respectively.
- θ_i: is the phase of the carrier generated by the $i-th$ satellite.

Service name	C/A	L1C	P(Y)
Centre frequency [MHz]	1575.42, L1	1575.42, L1	1575.42, L1
Signal component	Data	Data and Pilot	Data
Modulation	BPSK(1)	TMBOC(6,1,1/11)	BPSK(10)
Subcarrier frequency [MHz]	~	Data 1.023 Pilot 1.023 and 6.138	~
Code frequency [MHz]	1.023	1.023	10.23
Primary code length	1023	10230	$6.19 \cdot 10^{12}$
Data rate [bps]	50	50	50

Table 1.2: L1 signal parameters.

To enhance comprehension of the signal parameters, a visual depiction is provided in Figure 1.6 and 1.7.

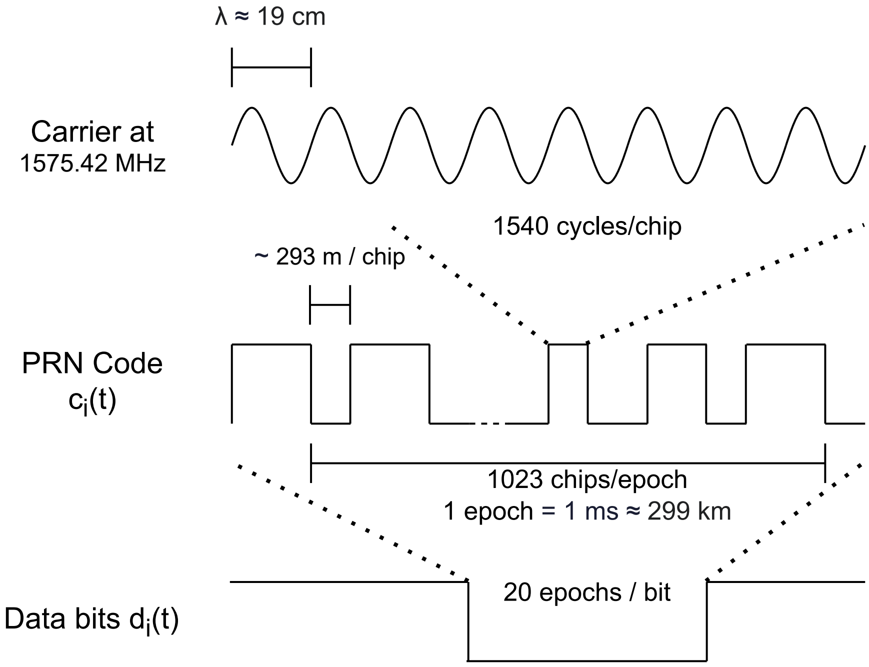

Figure 1.6: GPS C/A parameters visualization.

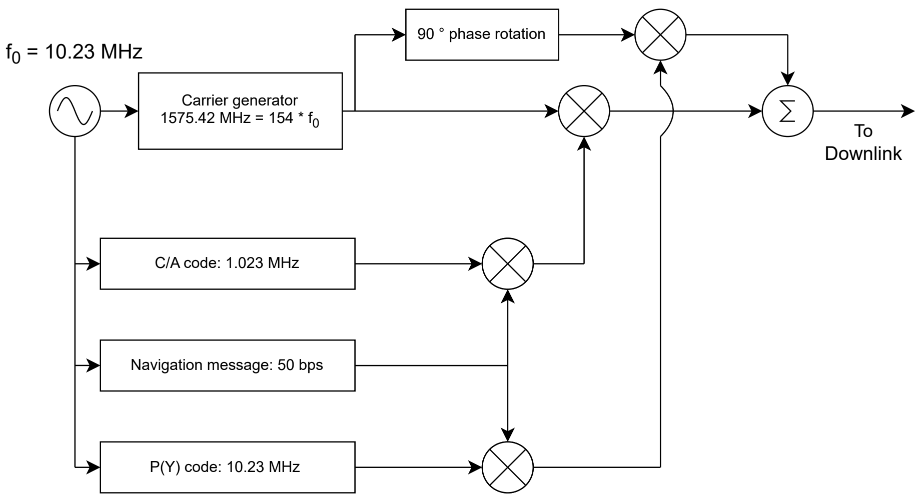

Figure 1.7: Simplified GPS modulation scheme.

1.4.2 Galileo Signals

Galileo satellites continuously emit three composite CDMA signals, identified as E1, E5, and E6. Galileo employs composite CDMA signals to deliver a variety of services tailored to different user needs. These services span a broad spectrum of applications, guaranteeing accuracy, reliability, and accessibility across diverse sectors. The service provided by Galileo are:

- **Open Service (OS)**: The Galileo Open Service provides global positioning and timing targeting mass market receivers.
- **High Accuracy Service (HAS)**: The Galileo High Accuracy Service provides to civil users free of charge high-accuracy Precise Point Positioning (PPP) corrections. [15]
- **Public Regulated Service (PRS)**: Offers position and timing services exclusively to government-authorized users, targeting sensitive applications demanding uninterrupted service. It employs encryption for enhanced security, incorporating robust anti-jamming mechanisms and dependable fault detection capabilities.

Most of the spectrum occupied by the Galileo signals is shared with other systems, so, to minimize the interference between the constellations, the BOC modulation has been introduced. This method introduces a subcarrier consisting of the sign function of a cosine or a sine waveform, as described in 1.21.

$$s_c(t) = sign[sin(2\pi f_{sub}t)] \tag{1.21}$$

where f_{sub} represents the subcarrier frequency.

When the BOC derives from the $sign()$ function of a $sin()$ is called BOC_{sin}, if instead, it derives from the $sign()$ of a $cos()$ function, is called BOC_{cos}. The notation that describes the BOC modulation is the following:

$$BOC(n, m) \tag{1.22}$$

where n and m represent, respectively, the subcarrier frequency and the chip rate, both expressed in multiples of 1.023 MHz. An expression representing the BOC modulated signal is reported in 1.23.

$$x_{RF,i} = \sqrt{2P}d_i(t)c_i(t)s_c(t)cos(2\pi f_0 t + \theta_0) \tag{1.23}$$

where:

- $c_i(t)$: is the PRN code associated to the $i-th$ satellite, clocked at 1.023 MHz.
- d_i: is the navigation data message clocked at 50 bps.

- $s_c(t)$: is the BOC subcarrier.

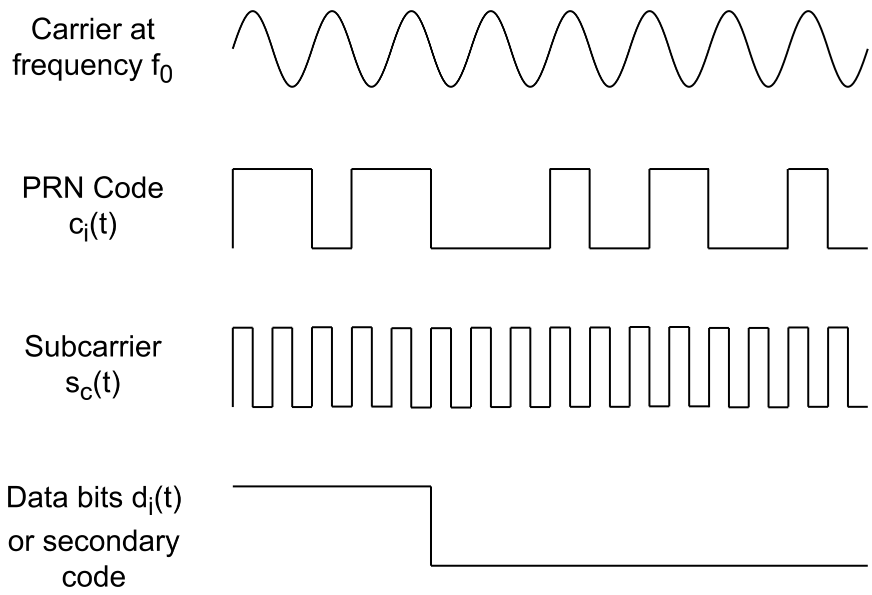

Figure 1.8: A representation of the components of a generic BOC modulated signal, not to scale.

In the context of Galileo, this study primarily focuses on the E1 signal, which is divided into three components: E1a, E1b, and E1c. E1a grants access to the PRS, while E1b and E1c distribute the OS, data and pilot channels, respectively. A description of the signals cited here is reported in 1.24.

$$\begin{aligned} e_{E1a}(t) &= d_{E1a}(t) \cdot c_{E1a}(t) \cdot s_{BOC_{cos}(15,2.5)}(t) \\ e_{E1b}(t) &= d_{E1b}(t) \cdot c_{E1b}(t) \cdot s_{CBOC_{in-phase}}(t) \\ e_{E1c}(t) &= c_{E1c}(t) \cdot s_{CBOC_{anti-phase}}(t) \end{aligned} \tag{1.24}$$

where:

- d_{E1a} is the data component associated to E1a.
- d_{E1b} is the data component associated to E1b.
- c_{E1a} is the PRN code associated to E1a.
- c_{E1b} is the PRN code associated to E1b.

- c_{E1c} is the PRN code associated to E1c.

The $E1a$ component undergoes modulation using a cosine BOC(15,2.5), so characterized by a subcarrier frequency $f_{sub} = 15 \cdot 1.023MHz$ and a chip rate $R_c = 2.5 \cdot 1.023MHz$. The $E1b$ and $E1c$ components, instead, employ Composite BOC (CBOC) modulation; this modulation consists into the combination of two BOC modulations with different parameters. In particular, the Galileo E1 CBOC can be expressed as:

$$CBOC(t) = \sqrt{\frac{10}{11}} s_{BOC(1,1)}(t) + \sqrt{\frac{1}{11}} s_{BOC(6,1)}(t) \tag{1.25}$$

where $s_{BOC(1,1)}(t)$ is a BOC(1,1) subcarrier, and $s_{BOC(6,1)}(t)$ is a BOC(6,1) subcarrier. The high frequency component is meant to enhance the tracking performance of the receiver, and can be in-phase or in anti-phase, as described in Figure 1.9.

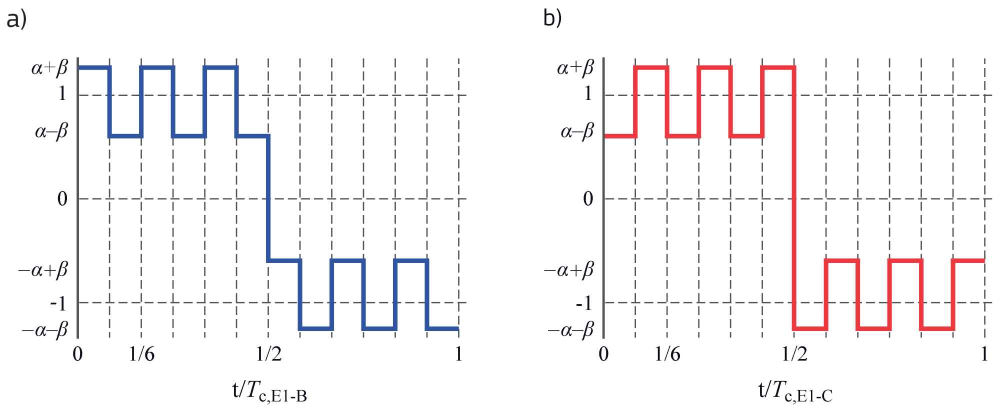

Figure 1.9: A graphical representation of one CBOC period for a) the $E1b$ component and b) the $E1c$ component. T_c represents the chip period.

A multiplexing technique called Coherent Adaptive Subcarrier modulation (CASM) is then employed to interplex the signal components, leading to the following resulting signal:

$$\tilde{s}(t) = \frac{\sqrt{2}}{3}[e_{E1b}(t) - e_{E1c}(t)] + j\frac{1}{3}[2e_{E1a}(t) + e_{E1,int}(t)] \tag{1.26}$$

where $e_{E1,int}$ is the intermodulation product, which is necessary to ensure constant envelope. After multiplexing, 44% of the power is allocated to $E1a$, while another 44% is equally distributed between $E1b$ and $E1c$. The remaining 11% is used by the intermodulation product.

The signals parameters of the Galileo $E1a$ and $E1c$ services are summarized in Table 1.3.

Service name	E1 OS		Galileo PRS
Component	E1b	E1c	E1a
Centre frequency [MHz]	1575.42, E1		
Signal component	Data	Pilot	Data
Modulation	CBOC(6,1,1/11)		BOC(15, 2.5)
Sub-carrier frequency [MHz]	1.023 and 6.138		15.345
Code frequency [MHz]	1.023		2.5575
Primary code length	4092		N/A
Secondary code length	~	25	N/A
Data rate [bps]	250	~	N/A

Table 1.3: Parameters of the signals transmitted on E1.

1.5 Signal propagation

The signal transmitted by the GNSS satellites propagates from LEO towards the user, which typically is situated on the surface of the Earth, or at an altitude of a few tens of kilometers considering civil and military aviation applications. To ensure adequate coverage, the primary lobe of the transmitting antenna is engineered to evenly distribute energy across the visible portion of the Earth's surface, considering the curvature of the Earth. Typically, GNSS satellites cover a wider solid angle compared to the angle subtended by our planet. For example, the main lobe of GPS satellites on L1 covers a solid angle of $\pm 21.3°$ [16], while the Earth subtends only an angle of $\pm 13.9°$. This allows also users in space to receive the GPS ranging signals, similarly this happens also for Galileo. GNSS coverage can be then considered split in two areas: the terrestrial service volume, and the space service volume, as shown in Figure 1.10.

In space, the signal received by the user may come from either the main lobe or the side lobe. However, transmitting signals in space consumes valuable resources, so the power available in the side lobes is reduced.

To have an estimate of the power density of the signal received by the user on L1, it is possible to apply the Friis transmission equation, subsequently it follows that:

$$PD_u = \frac{P_{tx} G_{tx}}{4\pi R^2 L_A} [watts/m^2] \tag{1.27}$$

where L_A is the atmospheric power loss and R is the propagation path length. Typical values of power density on Earth surface ranges around $-134\ dBW/m^2$. The calculation of received signal power necessitates incorporating the gain of the receiver antenna. In GNSS applications, low-gain antennas are often used to mitigate the adverse effects of GDOP associated with directional antennas.

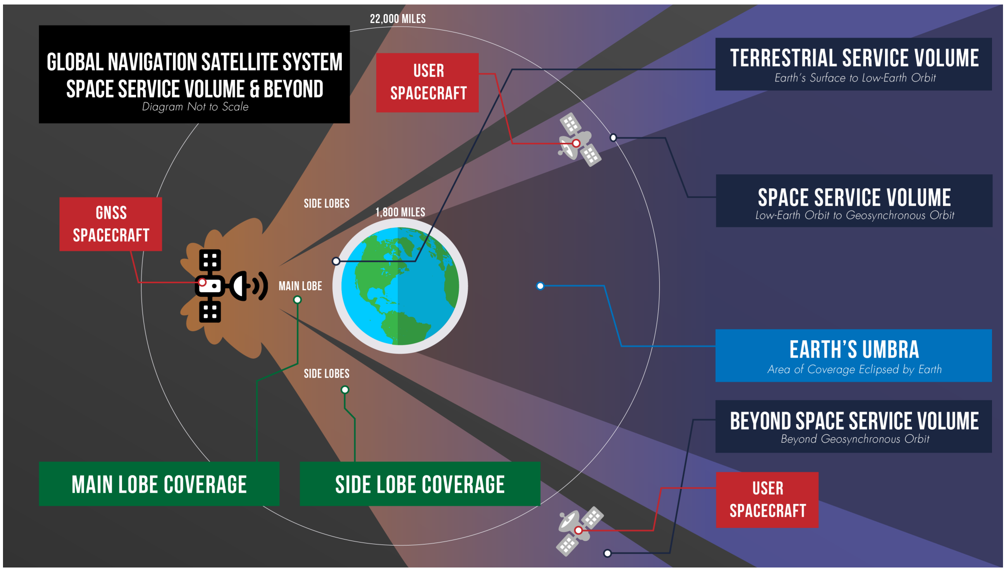

Figure 1.10: A graphic detailing the different areas of GNSS coverage. Source: NASA [17].

By orienting the primary lobe of the antenna towards the zenith, the impact of multipath signals, caused by ground reflections, is minimized. In general, the signal power can span, depending on the elevation angle, between $-160\ dBW$ and $-158\ dBW$. However, considering various levels of atmospheric attenuation and different antenna patterns, the power can drop to even lower values, potentially below $-164\ dBW$.

1.5.1 Doppler

A receiver with a non-zero relative velocity $v(t)$ with respect to a GNSS satellite will experience a shift on the carrier frequency f_{carr}:

$$f_D(t) = \frac{v(t)}{c} f_{carr} \tag{1.28}$$

As seen in expression 1.28, the relative velocity varies over time, which in turn affects the Doppler shift.

Recalling the expression 1.20, reporting the GPS signal comprising the C/A and

P(Y) components, the received signal can be modeled as:

$$r_{i,RF}(t) = \sqrt{2P_{C,RX}(t)}c_i(-\tau + t/k_D(t))d_i(-\tau + t/k_D(t))cos(2\pi f_{L1}t/k_D(t) + \theta_{i,RX}) + w_I(t) + \sqrt{2P_{Y,RX}(t)}c_{i,Y}(-\tau + t/k_D(t))d_i(-\tau + t/k_D(t))sin(2\pi f_{L1}t/k_D(t) + \theta_{i,RX}) + w_Q(t) \tag{1.29}$$

where:

- $P_{C,RX}(t)$ and $P_{Y,RX}(t)$: are the values of the received power for the C/A and the P(Y) components, respectively.
- $k_D(t) = 1 - \frac{f_D(t)}{f_{L1}}$: models the effect of the Doppler on the signal.
- $f_D(t)$: is the the value of the Doppler on the carrier.
- $w_I(t)$ and $w_Q(t)$: represents the noise on the In-phase and on the Quadrature components of the signal.
- τ: the code shift.

The Doppler shift does not affect only the carrier frequency, but it distorts the PRN code and, as a consequence, also the data bits. The expression of the chip rate in presence of a Doppler shift is:

$$R_D = R_{chip}(1 + \frac{f_D}{f_{carr}}) \tag{1.30}$$

where R_{chip} is the nominal chip rate.

1.5.2 Multipath

Multipath occurs when GNSS signals arrive at the receiver via several different paths due to reflections off surfaces like buildings, bodies of water, or the ground. This can cause substantial errors in position estimation, as the reflected signals cover greater distances than the direct line-of-sight signals, resulting in inaccurate pseudorange measurements.

Having at the receiver several delayed copies of the same signal, delayed in time, with different power levels and with a different carrier phase, may introduces errors in the estimate of the pseudorange. This happens because of some deformation of the peak of the correlation function exploited at the acquisition, and then also at the tracking stage, to evaluate the carrier phase. Most of the techniques employed in modern GNSS receivers to mitigate multipath typically employs particular tracking loop architectures like the narrow correlator [19], the pulse aperture correlator [20] and the Multipath Estimating Delay Locked Loop [21]. A study of the theoretical limits of the accuracy of the pseudorange estimation is reported in [22].

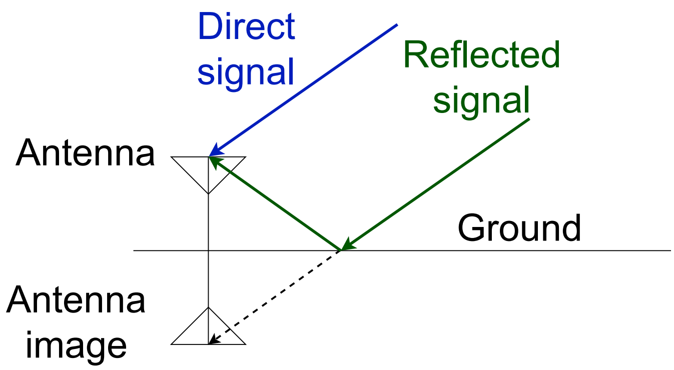

Figure 1.11: A pictorial representation of the multipath effect.

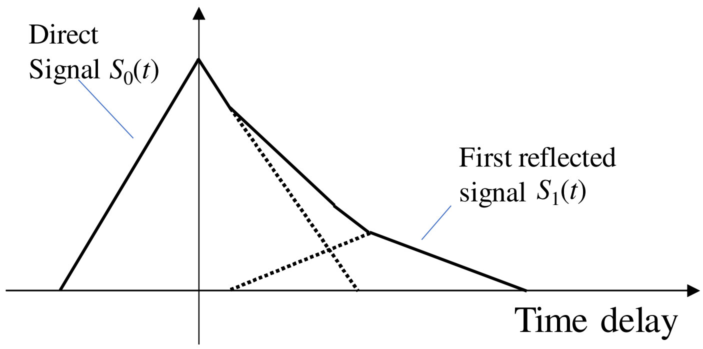

Figure 1.12: A pictorial representation of the effect of multipath on the correlation peak at the correlator. Source: [18].

1.6 The GNSS receiver

This section provides a concise introduction to GNSS receivers, focusing on the key aspects of signal processing. Given the broad scope of this topic, the section will only cover aspects relevant to this thesis, particularly the processing that occurs before the tracking stage. A more comprehensive overview of GNSS processing is reported in [10]. The expression reported in this section refers to the processing of a GPS signal on L1, anyway a similar discussion can be done for other GNSS signals.

1.6.1 The antenna

GNSS signals are right-hand circularly polarized and the GNSS antennas are also right hand circularly polarized. An optimal GNSS antenna present a low gain of about 3 dB [23]. For a user on the Earth surface, this allows to reject the signals reflected by the ground and to receive most of the power from signals propagating in line of sight by orienting the antenna upwards. In some cases, for scientific or signal quality monitoring purposes, the receiver antenna utilized may be characterized by a particularly high gain. For instance, [24] presents results obtained by processing signals received using the Green Bank Telescope. This fully steerable radio telescope, which is the largest in existence as of July 2024, with a 100-meter dish, has a gain of approximately 70 dB in the L-band.

1.6.2 Front end

The front end of the receiver has the task to amplify, downconvert and filter the received signal. The first step involves amplifying the weak signal received by the antenna while adding the least amount of noise possible. For this reason, a Low Noise Amplifier (LNA) is utilized. Typically, the LNA is employed together with a Variable Gain Amplifier (VGA) controlled by an Adaptive Gain Control (AGC) loop, to control the level of the power prompted to the successive processing steps, and to avoid saturation. This amplification is performed only on the band of interest, which for the case of GNSS is the L-band.

After amplification, the signal is downconverted to either baseband or an intermediate frequency (IF). According to the study [25], 88 % of the receivers surveyed in literature perform downconversion to a low intermediate frequency, typically below a few tens of MHz. This process may be carried out in multiple steps, gradually reducing the carrier frequency.

Before sampling the downconverted signal, a bandpass filter is utilized to remove out-of-band components and perform image rejection. The filters used can be either passive, such as Surface Acoustic Wave (SAW) filters, or active.

After filtering, the signal can be sampled with an Analog to Digital Converter (ADC). While low-cost receivers may use 1-bit ADCs, multi-bit ADCs should be used to achieve better performance.

Thermal noise, combined with the noise introduced by various components in the processing chain, significantly degrades the SNR.

The contribution to the total noise of each component can be modeled as an additive random process at the input of the receiver. The processing performed by the front end impact both the desired signal and inherent noise. As a consequence, when comparing receivers with different filter characteristics, relying solely on the power of the signal and of the noise might be inadequate for a comprehensive evaluation. To address this limitation, the field of GNSS adopts Carrier to Noise Density ratio (C/N_0) as a more suitable metric compared to Signal to Noise Ratio

(SNR). Hence, the expression defining the SNR is:

$$SNR = \frac{P_R}{N_0 B} = \frac{C}{N_0} \cdot \frac{1}{B} \tag{1.31}$$

where:

- P_R: represents the power of the received signal in the whole bandwidth.
- N_0: is the noise power spectral density.
- B: is the filter bandwidth.

The $C/N0$ is expressed in $dBHz$.

The C/A component of the model reported in the expression 1.29, can be approximated without considering the Doppler on the code and on the data components as:

$$r_{i,RF,I} = \sqrt{2P_{C,RX}(t)}c_i(t-\tau)d_i(t-\tau)cos(2\pi(f_{L1}+f_D)t+\theta_{i,RX})+w_i(t) \tag{1.32}$$

After the downconversion the IF version of the signal can be written as:

$$r_{i,IF,I} = \sqrt{2P_{C,RX,IF}(t)}c_i^b(t-\tau)d_i(t-\tau)cos(2\pi(f_{IF}+f_D)t+\theta_{i,RX})+w_I^b(t) \tag{1.33}$$

where the apex 'b' represents the filtered version of the reported quantities. The sampled version of the signal can be then expressed as:

$$r_{i,IF,I}[n] = \sqrt{2P_{C,RX,IF}[n]}c_i^b(nT_s-\tau)d_i(nT_s-\tau)cos(2\pi(f_{IF}+f_D)nT_s+\theta_{i,RX})+N[n] \tag{1.34}$$

where T_s is the reciprocal of the sampling frequency f_s and $N[n]$ represents the noise affecting each sample. A similar expression can be obtained also for the P(Y) component, anyway, the discussion of this signal is out of the scope of this work.

1.6.3 The acquisition stage

Acquisition provides an approximate estimate of the code shift τ and Doppler frequency values for the received signals. These estimates are then utilized to initiate the successive processing steps. As mentioned in the previous sections, the received signal is extremely weak, so to perform this evaluation the GNSS receiver correlates demodulated versions of the received signal with the local replica of the PRN codes associated to the satellite to be acquired. This allows to the correlation peak to retrieve the estimate of the shift of the code with respect to the local code replica $\bar{\tau}$. In Figure 1.13 is reported the auto-correlation between a GPS C/A PRN code and a replica of the same code delayed by 512 chips.

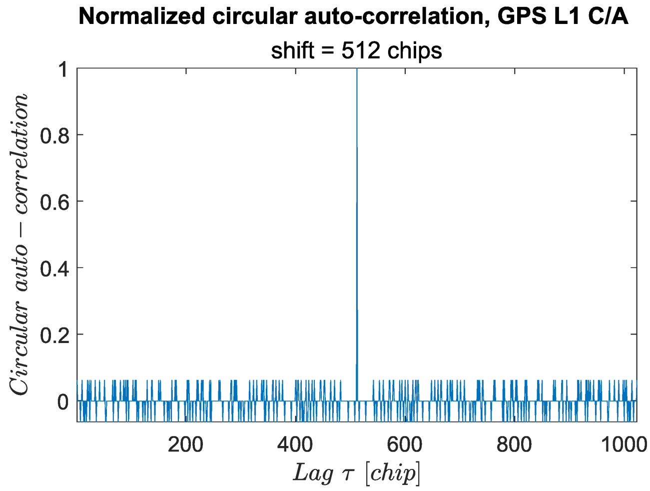

Figure 1.13: Normalized circular correlation of a GPS C/A code, with its own replica delayed by 512 chips.

Considering the sampled signal $r_{IF}[n]$, the correlation with a local code replica can be obtained exploiting the Fast Fourier Transform (FFT) based correlator reported in Figure 1.14

Before computing the correlation, the received signal $r_{IF}[n]$ is demodulated with a local complex carrier $F_{local}[n]$ at the frequency $f_{carr} + \bar{f}_D$; in this discussion the carrier frequency is $f_{carr} = f_{L1}$. The correlation can be then performed by applying the FFT to the local code replica and to the demodulated signal, then the complex conjugate of the frequency domain version of the local code is multiplied with the frequency domain version of the demodulated signal. To obtain the circular correlation for all delay values $\bar{\tau}$, with a resolution of one sampling period, the Inverse Fast Fourier Transform (IFFT) must be applied to the resulting product. Typically, the squared modulus of the correlation is considered. To evaluate the Doppler frequency f_D it is possible to test different values of $\bar{f}_D$ while performing the demodulation, the frequency leading to the largest peak may be considered an estimate of the Doppler shift value. Computing the values of correlation (typically the modulus square) obtained for different delays $\bar{\tau}$ (obtained in one shot with the FFT-based correlator) and for different Doppler shift values $\bar{f}_D$, it is possible to obtain the so called Cross Ambiguity Function (CAF). In this work the CAF is also referred to as S^2.

An example of a CAF is shown in Figure 1.15. A receiver can use the CAF to evaluate the presence of a given PRN in a signal by applying a threshold to the CAF values. If the receiver detects a signal, the Doppler and delay values corresponding to the highest CAF value can be considered as estimates of these parameters. The definition of the Doppler search space boundaries is reported in

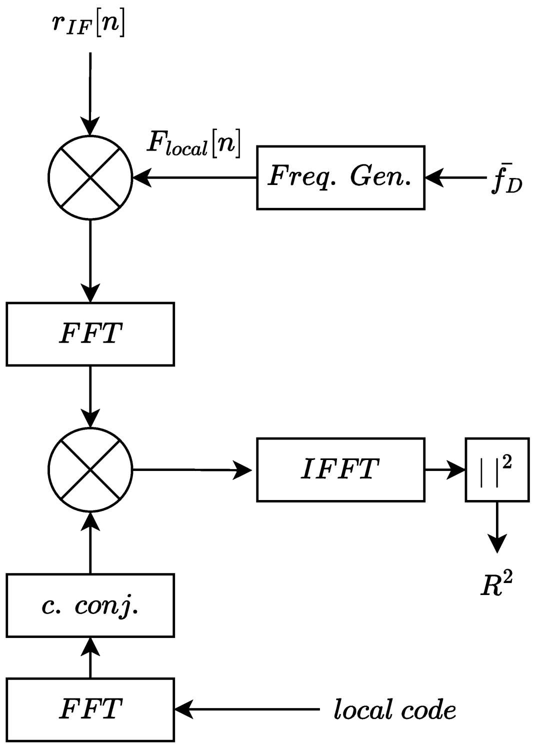

Figure 1.14: The FFT-based correlator.

Chapter 3.

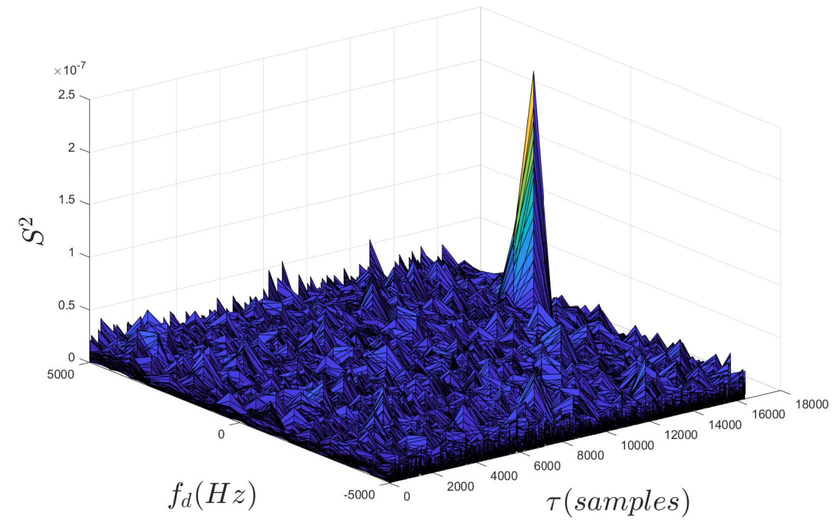

Figure 1.15: Example of the CAF obtained correlating a synthetic GPS C/A signal, sampled on 8 bits at 16.368 MHz, whit a local code replica. $C/N0$: 50 dBHz.

Chapter 2

Averaging and Dithering techniques

This chapter provides an overview of the averaging techniques employed to improve signal observability. Following a brief review of the relevant literature, the chapter includes a theoretical discussion on the noise reduction achieved through these processing methods. The primary aim of this chapter is to introduce these techniques, elucidating their fundamental principles and highlighting the most significant aspects. The practical implementation of the proposed methods is detailed in chapter 3.

2.1 Physical signal integrity

The concept of integrity in GNSS is multifaceted and spans different layers of the receiver stack. This thesis primarily focuses on enhancing the signal observability, this should allow to facilitate the evaluation of the physical integrity of the signal. Signal corruption can lead to integrity issues also to the observables and the afflict the integrity of the positioning solutions provided by the receiver.

The 1993 signal anomaly on GPS Block II Space Vehicle 19 (SV 19), caused by a fault in the satellite itself, is widely regarded as a pivotal event in the development of signal quality monitoring [26]. During this event in July 1993, the Wisconsin Department of Transportation reported a pseudorange bias of approximately 4 meters between the C/A and P(Y) code measurements on SV 19. Trimble Navigation performed static differential position measurements, which confirmed the presence of significant positioning errors for GPS users under certain conditions [27]. The tests showed that differentially corrected vertical position errors reached up to 8 meters when SV 19 was included in the solution set, compared to approximately 50 centimeters when the satellite was not in view.

These discrepancies highlighted the need for improved monitoring and correction methods, ultimately advancing the field of GNSS signal integrity monitoring. More importantly, an offset of this size consumes nearly the entire vertical error budget allocated to precision approach systems, underscoring the critical impact such anomalies can have on aviation safety [28]. In this scenario, Mr. Clyde Edgar, from Aerospace Corporation, utilized a 20-meter high-gain antenna stationed at Camp Parks to receive the C/A and P(Y) code waveforms from SV 19 and several other satellites. As reported in [28], the gain of the antenna allowed to receive the signal with a positive SNR, and so to visualize the received signal using an oscilloscope.

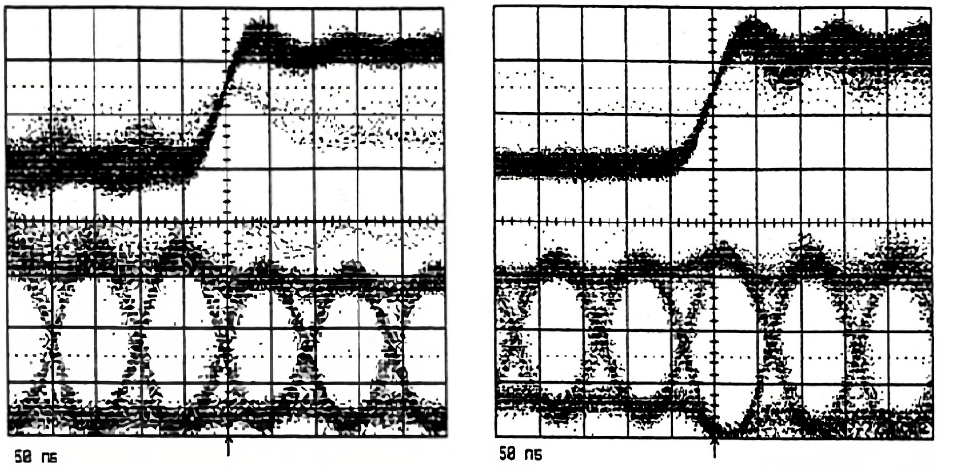

Figure 2.1: Oscilloscope capture of the signal obtained using the Camp Parks antenna in 1993. The C/A and P(Y) code rising edges (top and bottom part of the Figure respectively) of a healthy satellite (SV 26, left) are compared with those of the faulty SV 19 (right). Source: A. Mitelman [28]

As shown in Figure 2.1, the high gain of the antenna enabled a clear visualization of the code chip shape in the time domain. Specifically, it was possible to highlight a delay between the C/A code and the P(Y) code (shown in the top-right and bottom-right plots, respectively) transmitted by the SV 19. Furthermore, the plot also reveals a distortion in the C/A chip shape.

Following this event, several research studies were conducted on signal anomalies and, more broadly, on signal quality monitoring. In his dissertation, Ndili [29] examined various sources of potential signal impairments, including narrowband interference, broadband interference, and multipath. Specifically, several methods were proposed based on correlator output power, correlator output power variance, carrier phase jitter, and AGC gain. Jakab discusses in [30] the challenges of distinguishing satellite-based signal anomalies from multipath effects. The author proposes a method involving multiple evenly spaced correlators around the correlation peak to detect these anomalous signals. Phelts, in his dissertation [26], offers detailed discussions on the International Civil Aviation Organization (ICAO) threat model and methods for mitigating multipath effects. His study also includes an exploration of quality monitoring in relation to multipath. Additionally, the study highlights the impracticality of pseudorange-based anomaly detection due to pseudorange differences among various receiver configurations using the same signal. Indeed, this approach would require deploying a large number of receivers to cover the specified user receiver configuration space.

Prior to the emergence of the anomaly, the majority of research on distortion analysis concentrated on examining the output of the correlator. This methodology was already employed in the investigation and mitigation of the multipath effect, as indicated in [19]. In his dissertation [28], A. Mitelman introduced a technique that enhances the visualization of the GNSS code by reducing noise through averaging. This method allows for a clearer observation of the effects of various distortions on the signal. Subsequently, numerous studies [31] [32] [28] [33] [34] [35] [36], utilized this innovative technique not only to investigate signal anomalies, as demonstrated in [37], but also to unveil the codes of the novel GNSS constellations, Beidou [38] and Galileo. Many studies focus on chip transitions because signal distortions are particularly pronounced during these periods. The study [1] highlights that analyzing the shape of the chip of the PRN ranging code allows for better visualization of certain distortions. It also states that this approach can be extended to other GNSS signal modulations.

This thesis will focus on the GPS C/A signal, but this kind of approach may be extended also to the other GNSS signals.

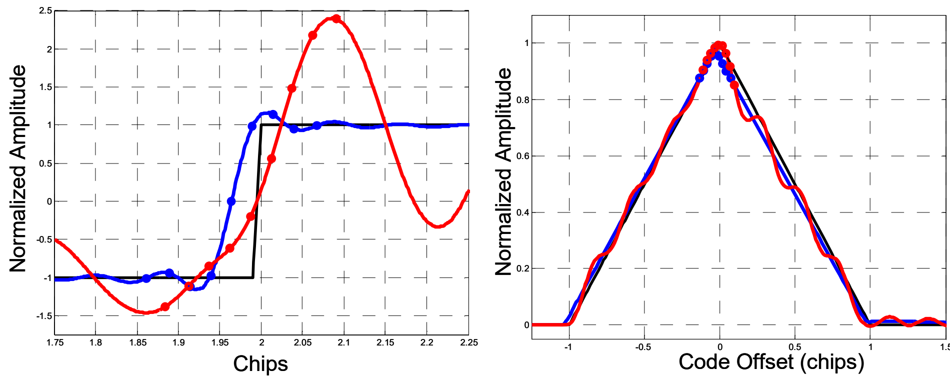

Figure 2.2: Example of comparison between the correlation peak and chip shape of a GPS C/A signal, both in nominal conditions (blue) and in presence of an anomaly in the signal (red). Source: [1]

2.2 Averaging

The averaging process, overlap several code epochs together to obtain a single code chunk with an improved SNR.

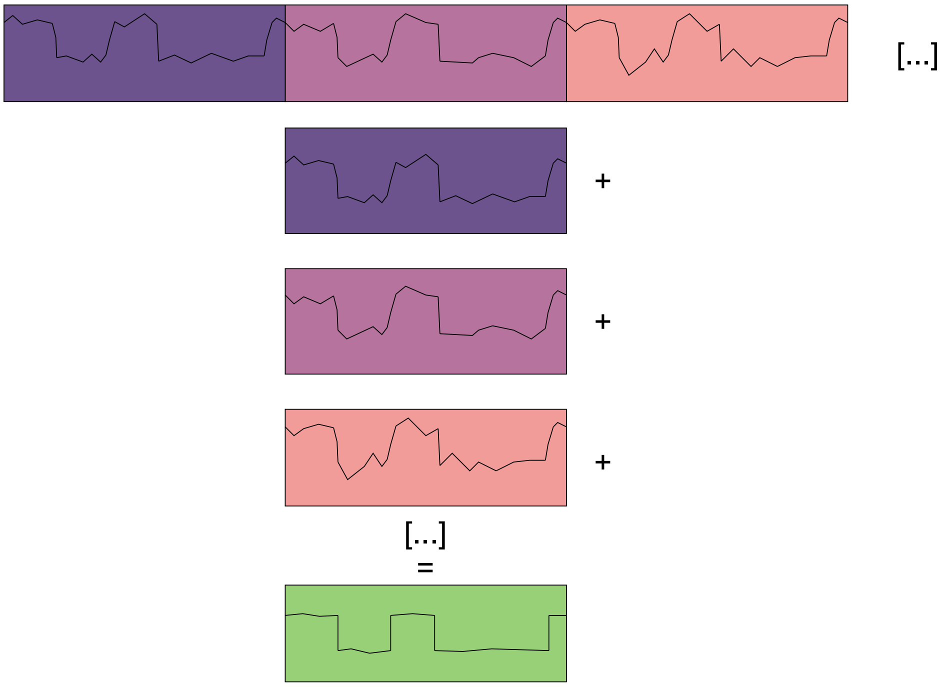

Figure 2.3: The code averaging concept, not to scale.

Recalling 1.34, and considering the C/A component while assuming ideal removal of the data bits and Doppler effects, the expression for the accumulated signal can be written as:

$$a[m] = \sum_{i=0}^{N_{code}-1} A \cdot c[m+iL] + n[m+iL], \ \forall m \in [0, L-1] \tag{2.1}$$

where:

- A is scalar representing the amplitude of the signal. For the sake of simplicity, it is supposed to be constant over time, anyway this is an approximation, indeed the received power tends to vary over time.
- L defines the length in samples of one code epoch.
- N_{code} is the number of code epochs considering for the accumulation process.

The equation 2.1 can be also expressed as:

$$a[m] = \sum_{i=0}^{N_{code}-1} A \cdot c[m+iL] + \sum_{i=0}^{N_{code}-1} n[m+iL] \tag{2.2}$$

Typically, the noise component $n[k]$ is assumed to be a $i.i.d$ zero mean Gaussian random variable with variance σ_n^2. Accumulating samples from different epochs allows to assume independence between the samples. Furthermore, this study focuses on short batches of samples, with a duration of a few hundred milliseconds, under these conditions the noise properties may be assumed to be constant over the observation window, anyway the $C/N0$ has a trend that characterize the variance on the long term. The signal power $P_{s,avg}$ equals $(N_{code}A)^2$, while the noise power can be then expressed as:

$$E[(\sum_{i=0}^{N_{code}-1} n[m+iL])(\sum_{j=0}^{N_{code}-1} n[m+jL])] = N_{code}\sigma_n^2 \tag{2.3}$$

Hence, the SNR expression becomes:

$$SNR = \frac{(N_{code}A)^2}{N_{code}\sigma_n^2} = \frac{N_{code}A^2}{\sigma_n^2} \tag{2.4}$$

An expression describing the relative standard deviation of the noise affecting the averaged signal can be expressed as:

$$\sigma_{avg} = \frac{\sigma_n}{\sqrt{N_{code}P_s}} \tag{2.5}$$

Additionally, considering also the effect of an ideal front end filter with bandwidth BW, the expression of the relative standard deviation becomes:

$$\sigma_{avg,BW} = \sqrt{\frac{N_0 BW}{2P_s N_{code}}} \tag{2.6}$$

This last expression, as reported in [34], is valid if the power loss due to the filtering of the useful signal is small (i.e. $BW >> R_c$).

Nevertheless, several aspects are not accounted for in this analysis, such as the presence of Doppler shift in the signal. The following section will provide a detailed explanation on how to address Doppler effects and other time-related factors.

2.2.1 Addressing the Doppler Effect

Typically, GNSS-oriented receivers correct biases introduced by users' clocks and Doppler shifts. However, in post-processing scenarios where positioning solutions are not computed on the fly, these corrections become crucially important. As a result, the receiver clock bias and Doppler shift affecting the received signal remain unknown until addressed during the post-processing stage.

A receiver with a non-zero relative velocity with respect to a GPS satellite will then receive a signal affected by a Doppler shift, so a simplified version of 1.29 becomes:

$$G(t) = c(t/k_d)cos(2\pi f_{L1}t/k_d) + p(t/k_d)sin(2\pi f_{L1}t/k_d) \tag{2.7}$$

defining $k_d = 1 - \frac{f_{Dop}}{f_{L1}}$. Equation 2.7 accounts for the presence of Doppler in an idealized continuous signal, assuming a Doppler shift that remains constant over time. To accurately process the received signal, the receiver must perform a downconversion step. However, the local clock used in this process can introduce a frequency bias, which may compromise the quality of the conversion. To account for these potential issues, the following expressions incorporate the effects of the local clock bias. The analysis is conducted in the continuous-time domain. However, the receiver may perform parts of the downconversion in the discrete-time domain. Therefore, in this context, operations are initially conducted in the continuous-time domain for simplicity, followed by sampling.

The down-conversion term can be introduced as:

$$L_c(t) = exp(j(2\pi(f_{L1} + f_u)t + \phi)) \approx exp(j(2\pi f_{L1}t/k_v + \phi)) \tag{2.8}$$

where, considering the approximation $1 + x \approx 1/(1 - x)$ for small values of x:

- f_u represents the local oscillator shift from L1 caused by the user clock bias.
- ϕ represents a residual phase term
- k_v is defined as $1 - \frac{f_u}{f_{L1}}$

Consequently, the expression of the down-converted signal, without the aliased components (the terms containing $2\pi f_{L1}(1/k_d + 1/k_v)$) becomes:

$$\begin{aligned}&G_{down}(t) = L_c(t) \cdot G(t)\\&G_{down}(t) = \tfrac{1}{2}[c(t/k_d)cos(2\pi f_x t - \phi) + p(t/k_d)sin(2\pi f_x t - \phi)]-\\&\tfrac{j}{2}[c(t/k_d)sin(2\pi f_x t - \phi) - p(t/k_d)cos(2\pi f_x t - \phi)]\end{aligned} \tag{2.9}$$

where $f_x = f_{L1}(1/k_d - 1/k_v)$. In the expression 2.9, it can be highlighted the presence of a residual frequency modulation together with a phase error. Additionally, the residual frequency shift due to the Doppler and the residual introduced by the local oscillator are modeled by a single frequency component f_x, so are indistinguishable from the receiver point of view. After downconversion and residual compensation, the receiver samples the processed signal. However, the sampling frequency is influenced by the shift caused by the local clock. Additionally, the PRN code is also affected by the Doppler shift. So, as derived by Mitelman in [28], the number of samples per epoch is:

$$\begin{aligned} N_e &= \tfrac{T_e}{T_s} \\ &= \tfrac{(T_{code})(1-f_{Dop}/f_{L1})f_{L1}}{M(1-f_u/f_{L1})} \\ &\approx \tfrac{T_{code}}{M}(f_{L1}+f_{res}) \end{aligned} \tag{2.10}$$

where:

- $f_{res} = -f_x$ is the frequency utilized to compensate the residuals presented in 2.9.
- $M \in \mathbb{Q}$, is the coefficient of the fractional frequency synthesizer such that the sampling frequency can be defined as $f_s = \frac{f_{L1}+f_u}{M}$
- T_e represents the effective code duration

The results reported in 2.10 are particularly important, indeed, the effects of both f_u and f_{Dop} are all modeled in f_{res}, also for what concerns the sampling. From now on, for the sake of simplicity, in this work the frequency shift will be called f_D, even if it does not depends only on the Doppler shift.

2.2.2 Sampling Strategies: Real-time sampling

Considering the averaging technique reported by the expression 2.1, to achieve noise reduction without blurring the underlying features in the waveform, it is necessary to have an integer number of samples per epoch. This averaging must be executed accurately, including compensation for local clock errors and Doppler shifts. Indeed, an integer number of samples per epoch allow to align all the samples of each epoch with the same code phase, without introducing any distortion in the averaged signal. A graphical representation of this concept is shown in Figure 2.4.

Anyway, the Doppler shift, as denoted in the expression 2.7, affects also the PRN ranging code. As a consequence, the code may be stretched or shortened in the time domain, so the receiver, to meet the requirements of having an integer number of samples per code epoch, should properly select the sampling frequency. This may be a difficult task, indeed, it may be not possible to have a priori a good estimate of the Doppler shift. Additionally, it may be not always possible to select the desired sampling frequency. In Figure 2.5 is reported an illustrative example where a Doppler-shifted code is sampled at a frequency that is an integer multiple of the original (nominal) code rate, but not of the actual, shifted code rate. To effectively process signals affected by Doppler shifts, it is essential that users have an accurate estimate of the Doppler shift induced by each satellite. This information can then be used to select a suitable sampling frequency for optimal

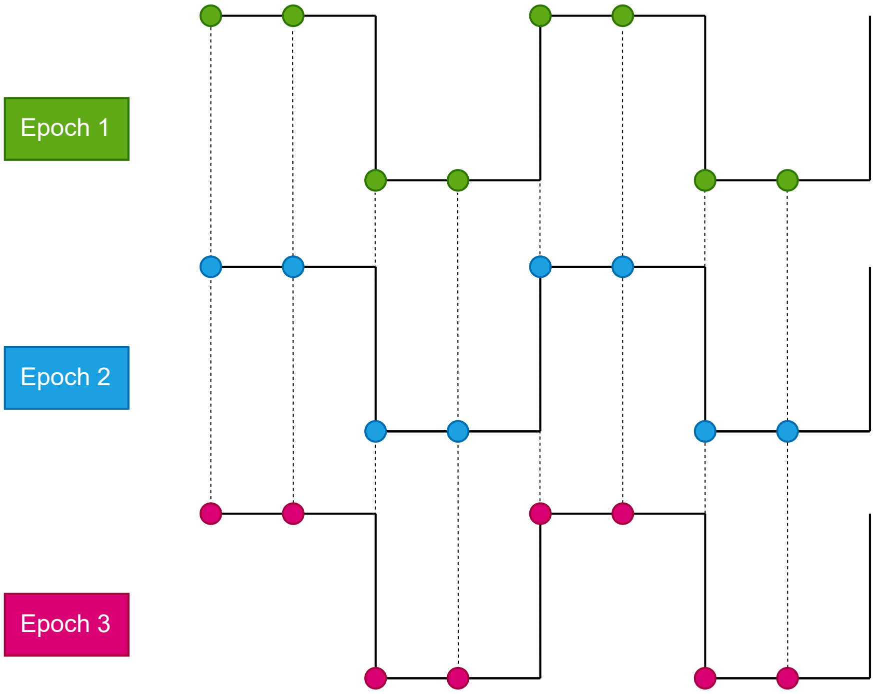

Figure 2.4: Sampling an ideal code with a sampling frequency which is a integer multiple of the code rate.

signal reception. However, this approach has a significant limitation: only one satellite's signal will be correctly sampled at any given time, while signals from other satellites with distinct Doppler shifts will exhibit characteristics similar to those depicted in Figure 2.5.

2.2.3 Sampling Strategies: Dithered Sampling

Several solutions have been proposed to address the challenges posed by Doppler-shifted signals and non-ideal sampling frequencies. One approach, initially suggested by Mitelman [28] involves resampling the signal; however, this method has its own limitations. In response, the author also introduced an alternative technique known as dithered or virtual sampling. By adapting this methodology, commonly used in oscilloscopes [39], it is feasible to improve the temporal resolution of sampled signals without necessitating an increased sampling frequency. While this approach still relies on the ability to set arbitrary sampling frequencies, subsequent sections will introduce a comparable technique that relaxes this requirement.

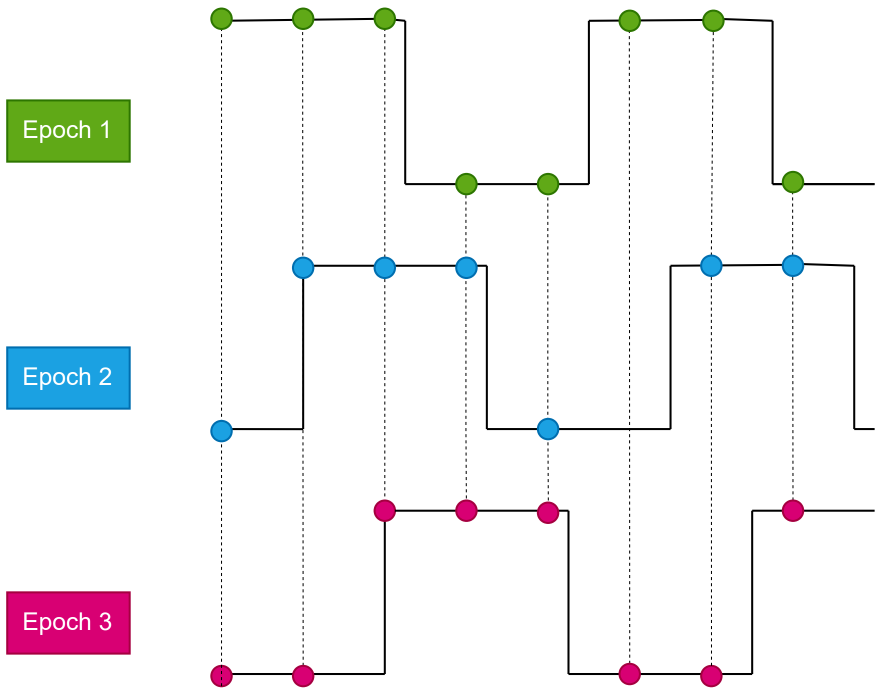

Figure 2.5: Sampling the Doppler shifted code with a sampling rate which is a multiple of the nominal code rate.

A repetitive code sequence permits selection of a sampling frequency that captures different sets of code phase values at each epoch, thereby enabling the acquisition of more code features at each iteration.

The technique can be described as follows. The receiver samples the signal at f_s, then the arrival time associated to each sample is relabeled with the modulus after division operator:

$$t_{re} = moduloAD(t_{arrival}, T_{code}) \tag{2.11}$$

where:

- the $moduloAD(x, y)$ operator returns the modulus after division of x by y , where x is the dividend and y is the divisor
- $t_{arrival}$ is the arrival time of the sample
- T_{code} is the code duration in seconds

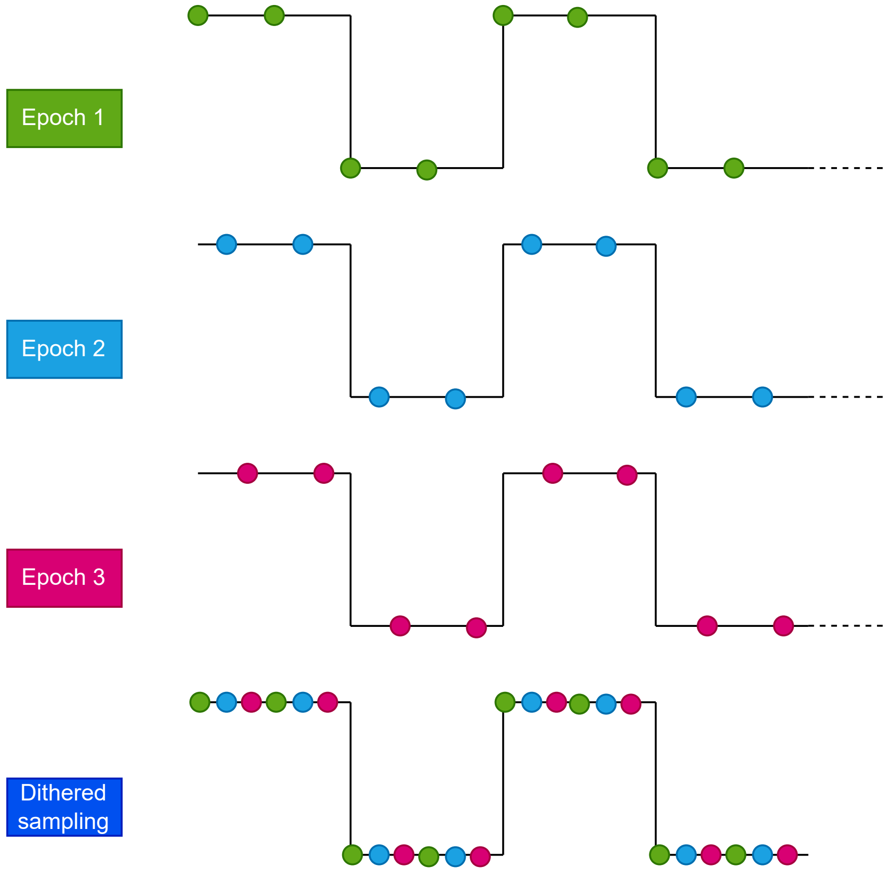

Figure 2.6: Pictorial representation of the Dithered sampling, also known as virtual sampling.

All the relabeled data from the sampled epochs are then combined to form a high-resolution representation of the underlying signal. This process is somewhat equivalent to increasing the sampling frequency, but it trades record length for time resolution. As a result, this methodology is also known as virtual sampling. A pictorial representation of the process is reported in Figure 2.6.

The user, can implement dithered sampling by selecting the sampling frequency f_s in the following way:

$$f_s = \frac{\lfloor T_e f_{s,MAX} \rfloor - \frac{1}{D}}{T_e} \tag{2.12}$$

where:

- $f_{s,MAX}$ is the max frequency allowed at the receiver

- T_e is the effective code period, defined as: $T_e = T_{code}(1 - \frac{f_{Dop}}{f_{L1}})$
- D is the Vernier ratio [28].

A unitary Vernier ratio enables synchronous sampling, ensuring that the sampling frequency consistently captures the same set of code phases across all code epochs. Conversely, a value of $D > 1$ allows for higher virtual sampling frequencies. However, this methodology does not implement noise reduction; instead, it trades longer record duration for higher temporal resolution. Observing code features with finer resolution is crucial for evaluating signal anomalies. If the signal exhibits an adequate SNR, this approach offers certain advantages. However, noise remains a concern, even when the signal is received with a high-gain antenna. To address this issue, various techniques that hybridize averaging and dithered sampling have been proposed [37].

2.2.4 Dithering and Averaging hybridization

The primary disadvantage of the previously proposed techniques is the need to sample the signal at a frequency dependent on the Doppler shift. This can be impractical for several reasons: the Doppler shift may be unknown, the receiver might be unable to select arbitrary sampling frequencies, and the receiver may need to process signals from multiple satellites within the same recording.

The receiver should be able to set a frequency that depends solely on its own implementation, without being influenced by any external factors. Starting from this assumption, combining the principles of averaging and dithering enables the mitigation of low SNR issues, thereby enhancing the temporal resolution of the sampled signal.

To obtain such a result, the receiver should perform the following steps:

- Downconvert the signal to baseband.
- Sample the signal at a fixed sampling frequency f_s.
- Use the sampled signal to estimate the Doppler shift, or alternatively, utilize prior knowledge of the Doppler shift affecting the signal.
- Compensate for the residual modulation caused by the Doppler shift.
- Correct the effects of Doppler on the ranging code.

It is important to note that the signal considered is not modulated by navigation data bits. This issue will be addressed in the following chapters, where the proposed implementation of the averaging technique is discussed.

After the sampling step, the user can estimate the Doppler shift by processing the signal with a GNSS receiver. The GNSS receiver can utilize a tracking loop to track the Doppler shift affecting signals from different satellites. Consequently, the results can be utilized to accurately compensate for the residual frequency shift, as proposed in [37]. Alternatively, the user may be able to predict the Doppler effect in each signal by estimating it based on their own position and the time of the recording, utilizing the almanac as proposed in [28].

After removing the residual modulation, the receiver can compensate for the Doppler shift affecting the ranging code. One method involves relabeling each received sample's arrival time with a time that compensates for any stretching or shortening of the code. This approach is equivalent to having a new sampling frequency that depends on the Doppler shift. In particular, the expression 2.10 evaluates the number of samples per code epoch, N_e, in the presence of Doppler. With this information, it is possible to obtain a new virtual sampling period. This period ensures that all N_e samples fit within the nominal code duration. This approach does not require any operation on the samples; it simply adjusts the time of arrival of each sample to account for the Doppler effect. Importantly, each sample maintains its code phase. A pictorial representation of this process is presented in Figure 2.7.

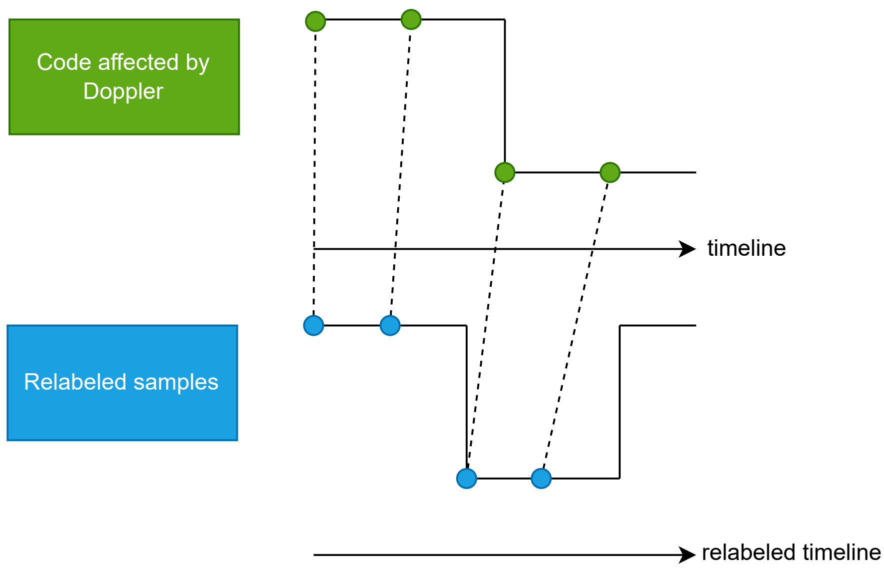

Figure 2.7: Sample relabeling

For instance, if the Doppler stretches the code duration, the receiver will obtain a larger number of samples per code epoch, then this is equivalent to sampling the code with a nominal duration with a higher frequency. The same principles work also for the codes with a shorter duration. However, this technique alone does not implement the averaging step; it is similar to the dithered sampling presented in Section 2.2.3. The primary advantage, in this case, lies in not needing to select the receiver sampling frequency, which enables performing Doppler compensation during post-processing. To facilitate averaging, it is essential to relax the requirement that samples from different epochs must have identical code phases.

Relaxing this requirement enables the averaging process to include samples from different epochs that have similar code phases. An implementation of this concept is presented in [32] and [37]. The methodology is described as follows. The user first relabels the samples. Following this, the modulo operation reported in the expression 2.11 is performed considering the recomputed arrival times. One code period is then divided into an arbitrary number of bins, denoted as N_{bins}. Each sample is associated with the corresponding code phase bin. This allows all samples within a bin to be summed together, resulting in an averaged code epoch of length N_{bins}. The proposed method increases both the SNR and the time resolution when the number of bins exceeds the original number of samples obtained within one code epoch. A pictorial representation of a possible implementation scheme is reported in figure 2.9.

The gain resulting from the accumulation of several samples from different epochs remains consistent with the expression reported in 2.4, with the primary difference being that the SNR obtained from the accumulation of samples within a single bin depends on the number of samples in the bin $N_{samp,bin}$, rather than on the number of code epochs considered.

$$SNR_{bin} = \frac{N_{samp,bin} A^2}{\sigma_n^2} \tag{2.13}$$

The number of samples per bin is typically lower than the number of samples accumulated when code epochs are directly superimposed after sampling. This is similar to the ideal scenario where the sampling frequency is an integer multiple of the code rate and the signal is unaffected by Doppler shift, as shown in Figure 2.4. For example, in the case of ideal dithered sampling, where the virtual sampling frequency is twice the actual sampling frequency, and the bin width is chosen to be half the original sampling period, each bin will contain a number of samples equal to half of the total accumulated code epochs. A graphical representation of this is reported in Figure 2.10.

2.2.5 Chip Domain Observable

The approach presented in the section 2.2.4 represent a realistic and feasible methodology of the averaging technique, anyway the increment of the temporal

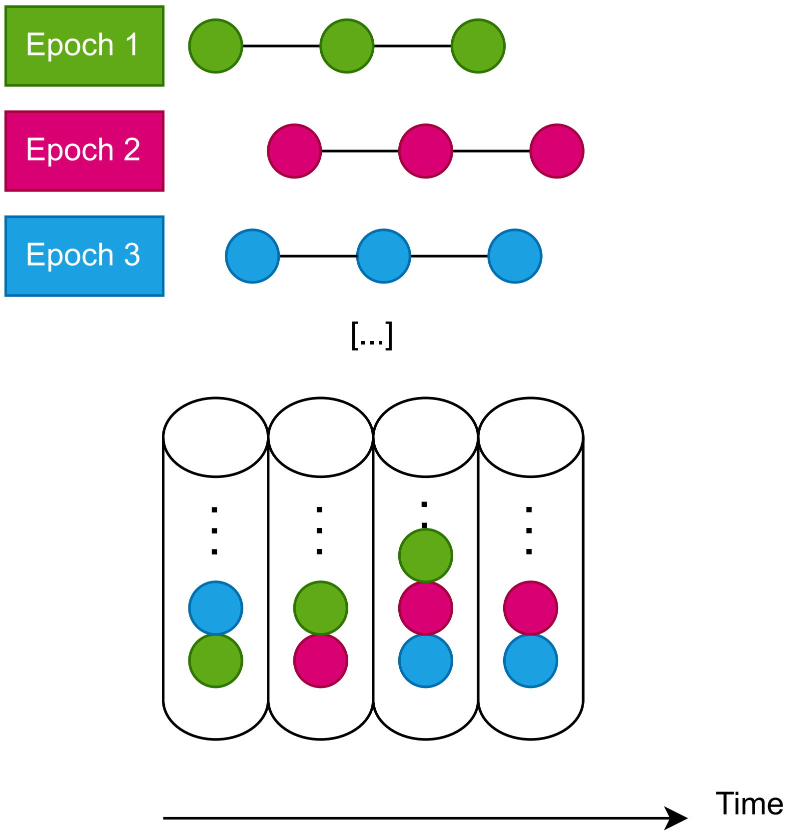

Figure 2.8: Pictorial representation of the averaging process utilizing the code phase bins. All the samples, from different epochs are mapped to the corresponding code phase bins.

resolution may result into a reduction of the noise averaging effect of the sample accumulation. In some scenarios, it may be necessary to further reduce the effect of noise to evaluate the underlying signal features accurately. To achieve this, the user can increase the number of epochs considered for accumulation. However, this may not always be possible due to certain restrictions at the receiver. Moreover, anomalies and features of interest that affect signal processing at the receiver typically impact small portions of the chip, especially the rising and falling edges. Consequently, several studies have proposed techniques that focus specifically on analyzing the chip shape.

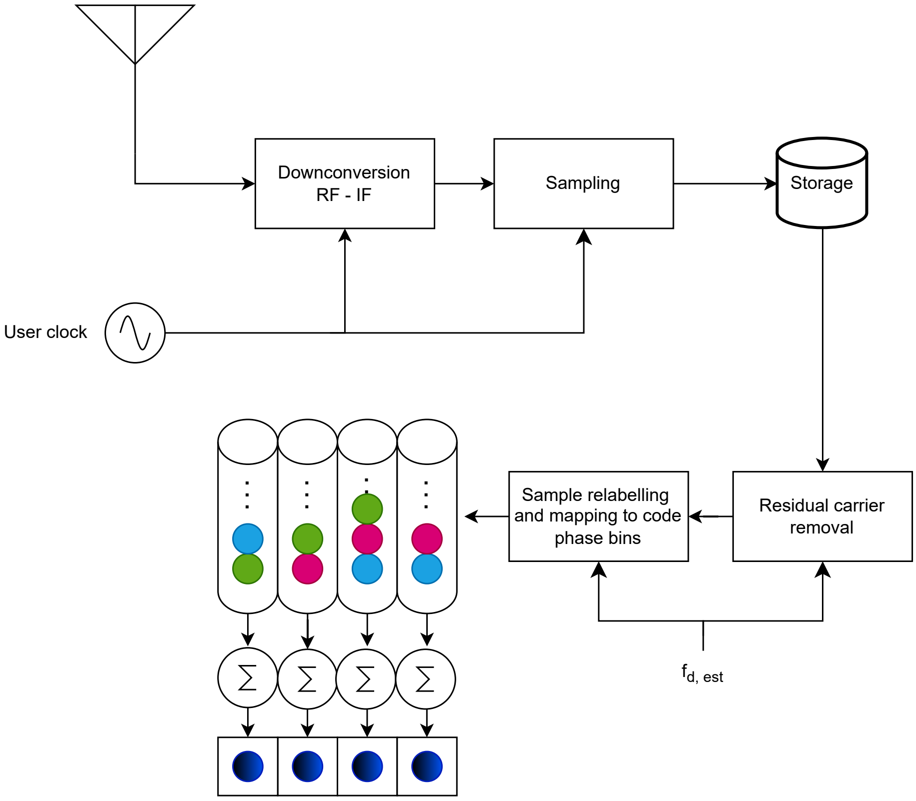

Figure 2.9: Diagram of a possible averaging implementation.

To average out the noise affecting the temporal samples of the GNSS signal, an 'average' chip transition is constructed by superimposing all spreading code transitions within a specified observation time window. A pictorial representation of this concept is reported in Figure 2.11.

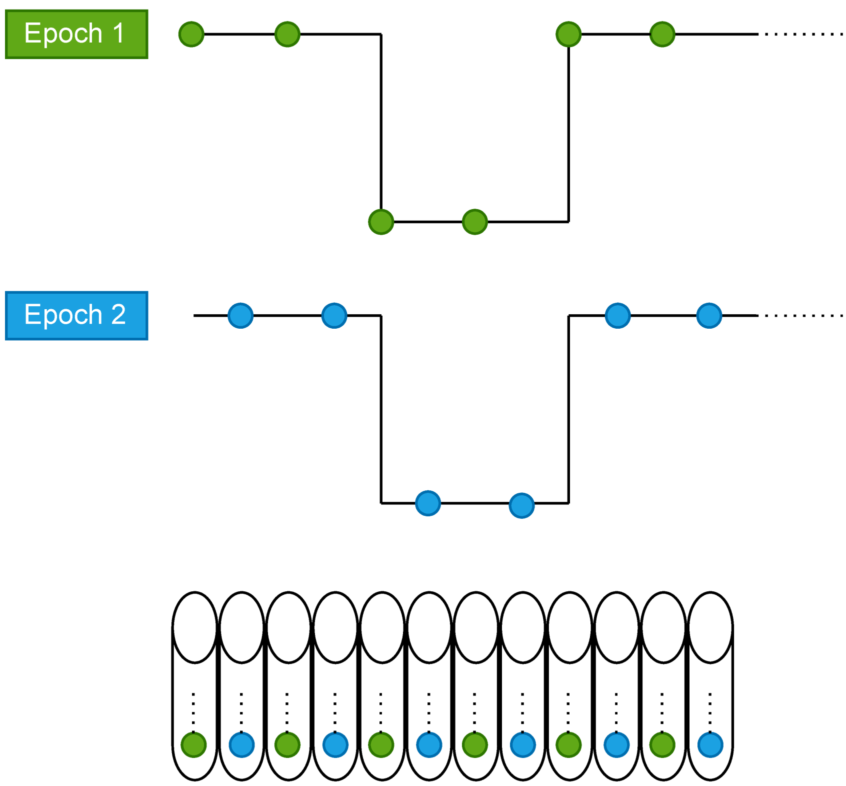

Figure 2.10: Example of dithered (virtual) sampling.

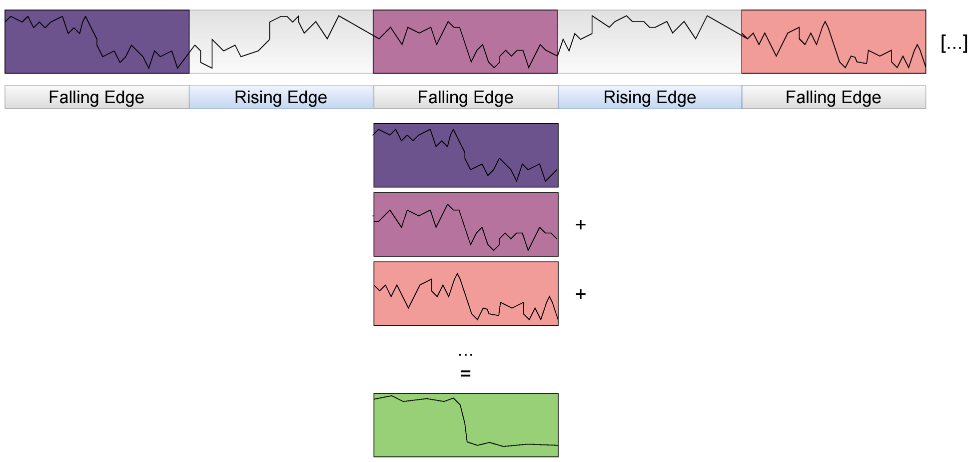

Figure 2.11: Pictorial representation of the Chip Domain Observable estimation. In this case only the falling edges of the PRN code are accumulated together.

The implementation of this technique is similar to that described in Section 2.2.4. The main difference is that, instead of accumulating entire code epochs, only the chip transitions are accumulated while considering their polarity. Given that a GPS C/A code may contains approximately 250 transitions per code epoch, this approach allows for increased temporal resolution and SNR. The trade-off is that only an 'average' chip is observed, rather than an averaged version of the entire code. As in the previous case, the number of samples per bin depends mainly on the bin width and on the number of chips averaged together. In this case, it is particularly advantageous to leverage the frequent chip transitions within a code epoch to decrease the bin width, thereby achieving better temporal resolution.

2.2.6 Chip Domain Observable vs. Correlator

In GNSS receivers, the acquisition stage enables the receiver to estimate the delay τ of the received PRN code by utilizing the correlation function. Correlation acts as an effective compression algorithm, concentrating most of the signal's energy into the correlation peak when the local replica of the code is correlated with the incoming signal. Assuming a correct estimate of the Doppler shift, the peak of the correlation function carried the information about the delay of the received PRN code with respect to the local replica. Furthermore, the shape of the correlation peak also provides information about the presence of distortions in the signal, as denoted in [26].

One of the advantages of the correlation function is that each correlator output leverages the coherent accumulation of all the recorded signal samples. When the local replica and the received signal are correctly aligned in the time domain, the samples are coherently accumulated. The gain achieved behaves similarly to the accumulation techniques proposed in 2.4 and 2.13. However, the SNR gain of the resulting observable is proportional to the number of samples considered in the signal recording, and is therefore, by definition, higher than the two aforementioned techniques. The expression of the correlation function can be written as:

$$R[n] = \frac{1}{N_{sam}} \sum_{m=0}^{N_{sam}-1} a[m]r[n+m] \tag{2.14}$$

where:

- $r[n]$ is the received signal, properly processed and downconverted accounting for the presence of the Doppler shift
- $a[n]$ is the local code replica
- N_{sam} is the total number of samples utilized for the correlation

Aside from any potential misalignment issues, assuming perfect synchronization between the replicated code and the incoming signal, the phase transitions induced by the PRN code are effectively eliminated, as illustrated in Figure 2.12. This allows to coherently accumulate all the samples. Therefore, the obtained observable has a relative noise standard deviation:

$$\frac{\sigma_{corr}}{\sqrt{Ps}} \propto \frac{1}{\sqrt{N_{sam}}} \tag{2.15}$$

where Ps is the signal power.

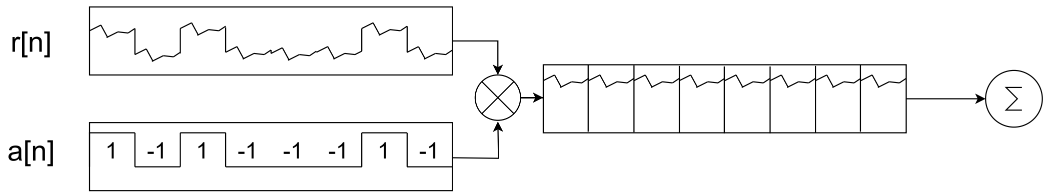

Figure 2.12: Pictorial representation of the computation of the correlation value obtained aligning the local code replica a[n] with the received signal r[n].

The received signal, after an ideal downconversion, can be written as:

$$r[n] = Ac[n] + w[n] \tag{2.16}$$

where:

- A is the signal amplitude
- $c[n]$ is the PRN code
- $w[n]$ is the noise, modeled as a zero mean White Gaussian random variable with standard deviation σ_n

The coherent sum performed in the correlator, assuming an ideal alignment between the received signal and the local code replica is:

$$R[\tau_{opt}] = \sum_{n=0}^{N_{sam}-1} A + \hat{w}[n] \tag{2.17}$$

where $\hat{w}[n]$ is the signal noise correlated with the local code replica [34]. Assuming that $\hat{w}$ is derived from the process $\hat{W}$ and $w[n]$ is derived from the process W, and that $\hat{W} \approx W$, the resulting SNR can be computed using equations 2.2 - 2.4 as follows:

$$SNR = \frac{(AN_{sam})^2}{N_{sam}\sigma_n^2} = \frac{N_{sam}A^2}{\sigma_n^2} \tag{2.18}$$

In general, the CDO tends to have a lower SNR compared to the correlator output observable. This is because the processing gain of the CDO is proportional to the number of samples in the averaging bins, which is typically smaller than the total number of samples.

Extending the coherent integration time increases the number of samples considered by the correlator N_{sam}, thereby enhancing the SNR.

Furthermore, it is worth noting that performing ideal averaging, where samples from N_{avg} epochs are perfectly superimposed before correlation, is almost equivalent to extending the coherent time over the same number of epochs.

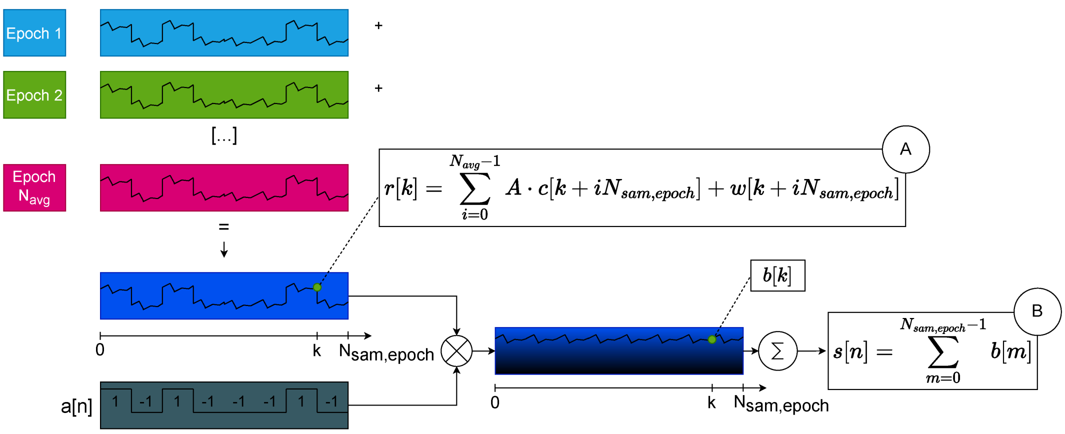

Figure 2.13: Averaging of N_{avg} code epochs and correlation of the averaged output with the ideally shifted local code replica.

Indeed, considering the expression $b[k]$ from Figure 2.13:

$$b[k] = \sum_{i=0}^{N_{avg}-1} A + w[k + iN_{sam,epoch}] \cdot a[k] = \sum_{i=0}^{N_{avg}-1} A + \hat{w}[k + iN_{sam,epoch}] \quad (2.19)$$

Where:

- N_{avg} is the number of code epoch considered during the averaging process.
- $N_{sam,epoch}$, is the number of samples in one code epoch. (The averaging is performed accumulating the samples with the same code phase).

Consequently:

$$s[n] = \sum_{m=0}^{N_{sam,epoch}-1} b[m] = \sum_{m=0}^{N_{sam,epoch}-1} \sum_{i=0}^{N_{avg}-1} A + \hat{w}[m + iN_{sam,epoch}] \approx \sum_{m=0}^{N_{sam}-1} A + w[m] \quad (2.20)$$

The results from expression 2.20 lead to the same SNR expression as in 2.18.

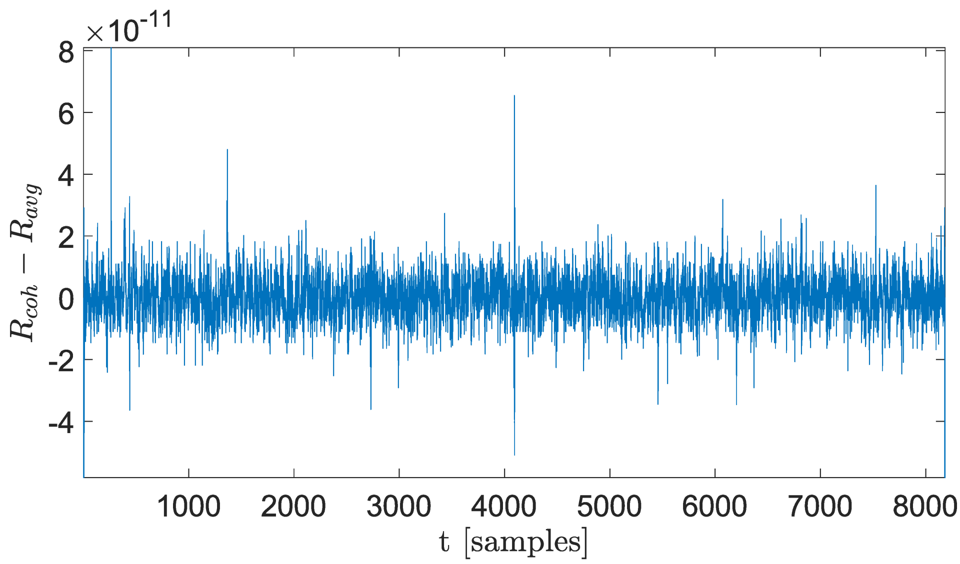

Figure 2.14: Example of difference between the correlation R_{coh}, achieved by extending the coherent integration time to 50 code epochs, and the correlation R_{avg}, obtained by averaging 50 code epochs and then performing the correlation. The input signal is a GPC C/A code affected by noise with $\sigma_n^2 = 10$

Chapter 3

Averaging technique implementation

This chapter presents the implementation of the averaging techniques proposed in the previous chapter. It is organized as follows: Sections 3.1 and 3.2 discuss the values of $C/N0$, Doppler shift, and Doppler rate in various scenarios, with a particular focus on extreme conditions such as those encountered by a receiver in space. These sections also define the requirements of the desired processing technique and briefly outline the architecture of the proposed method. The subsequent sections provide a detailed description of the processing steps performed by all the processing elements.

3.1 GNSS in space

To design a processing technique that enhances the observability of signal shape in the time domain, especially under the extreme conditions faced by a receiver in space, it is essential to quantify the ranges of parameters such as Doppler shift, Doppler rate, and $C/N0$ potentially affecting a signal. This section provides a brief review of pertinent literature to explore these aspects.

The use of GNSS at Low Earth Orbit (LEO) and Geostationary Earth Orbit (GEO) altitudes has already been a topic of research, as reported in [40], [41] and in [42]. Currently, several LEO satellites are equipped with onboard GNSS receivers, often used for scientific research or dedicated scientific missions [43]. For higher orbits, the NASA Magnetospheric Multiscale (MMS) mission demonstrated the possibility of tracking GNSS satellites at 25 RE. This mission consisted of four spacecraft, each equipped with specialized GPS receivers. During the first phase of the mission, which involved lower orbits, the spacecraft achieved a relative speed of 35,406 km/h, marking the highest known speed reached by a GPS receiver [44].

Each satellite in the MMS mission was equipped with two GPS receivers and four antennas, with a nominal acquisition threshold of 25 dB-Hz [45] [46].

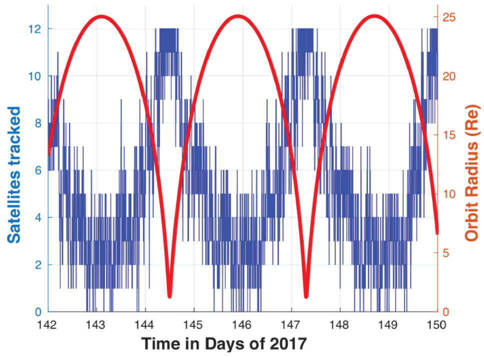

Figure 3.1: Number of tracked signals (blue), and radial distance (red). Source: [46]

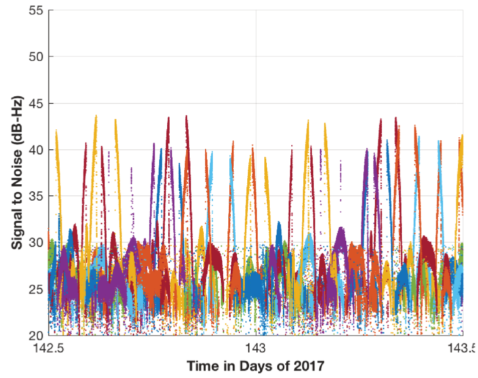

Figure 3.2: C/N_0 of the received signals as a function of time near apogee. Source: [46]

Figures 3.1 and 3.2 depict respectively, the number of tracked satellites and the C/N_0 experienced during the second phase of the MMS mission in 2017. According to [46], the received signal predominantly originates from the side lobes, with C/N_0 values rarely exceeding 30 dB-Hz.

Figure 3.1 shows that the number of tracked signals falls below four during certain time windows.

The MMS mission demonstrated the feasibility of utilizing GPS in space, even at moderately large distances from Earth, and suggests the potential for exploiting GPS at lunar distances as well. The low C/N_0 appears to be the major limiting factor for reliable signal acquisition and tracking, which may affect the overall performance of GNSS-based navigation under such conditions.

A model characterizing the link budget profile as a function of the distance from Earth's center is reported in [47] and is depicted in Figure 3.3. The study reported in figure 3.3, was conducted in preparation of the upcoming Lunar GNSS Receiver Experiment (LuGRE) mission [48].

The LuGRE mission is a collaboration between NASA [49], the Italian Space Agency (ASI) [50], Quascom [51], which is also the responsible for the design and the manufacturing of the receiver, and the Navigation Signal Analysis and Simulation (NavSAS) group of Politecnico di Torino [52]. It aims to demonstrate GNSS-based positioning, navigation, and timing (PNT) at lunar distances. During the mission, a GNSS receiver on Firefly's Blue Ghost Lunar Lander [53], will attempt to determine its location using GNSS. Additionally, it will transmit batches of signal samples,

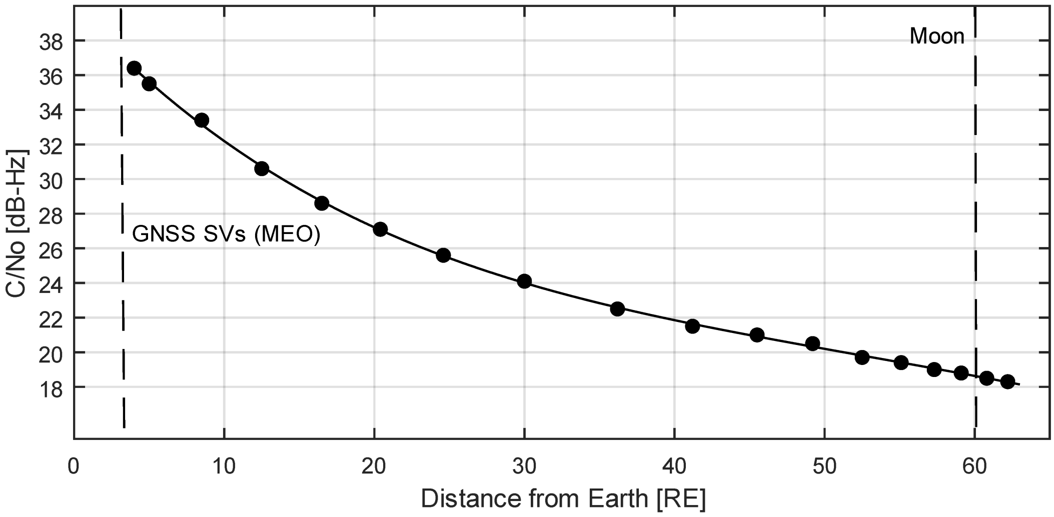

Figure 3.3: Estimated Link budget along the LuGRE mission trajectory. Source: [47]

each lasting a few hundred milliseconds. This data will aid in characterizing the signal in the Moon's transfer orbit and on the lunar surface. As it is possible to notice in Figure 3.3, in the worst case scenario the C/N_0 at 60 RE, so at Earth-Moon distance, is around 18 $dBHz$.

Another crucial factor to consider in these conditions is the significant relative velocity component, which results in a substantial Doppler frequency shift. A study detailing simulations of the Doppler shift experienced by a spacecraft in High Earth Orbit (HEO) is provided in [54]. This study simulated an HEO orbit with the parameters outlined in Table 3.1, and took into account both the GPS and Galileo constellations.

Semi-major axis	198613.5 km
eccentricity	0.966991166 °
inclination	5 °
period	10days 5h 20min 55s
perigee	185 km
apogee	390671 km
Max Orbital velocity	10.94 km/s
Min Orbital velocity	0.18 km/s

Table 3.1: Parameters of the HEO orbit simulated in [54]

The results of these simulations are presented in Figures 3.4 and 3.5. Specifically, Figure 3.5 illustrates that the Doppler shift experienced in HEO can exceed 50 kHz. Additionally, Figure 3.4 demonstrates that the Doppler rate ranges approximately between -5 Hz/s and 5 Hz/s. These findings underscore the significant Doppler effects encountered in HEO, which are critical for precise navigation and signal tracking.

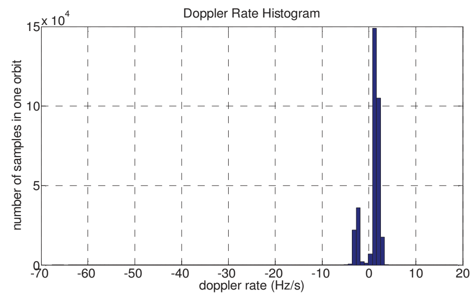

Figure 3.4: Doppler rate, histogram of the values obtained simulating a HEO orbit. Source: [54].

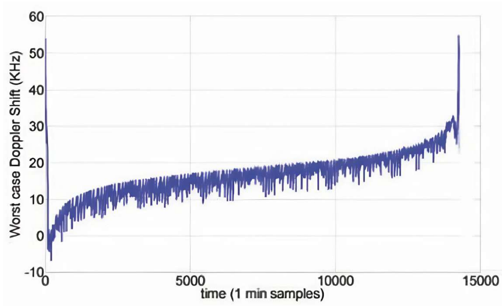

Figure 3.5: Values of Doppler shift vs. time. Simulation of a HEO orbit. Source: [54].

The study [55], shows that an airborne user at Mach 5 can reach a Doppler rate of almost -7.5 Hz/s. For what concerns terrestrial users, assuming a maximum speed of 200 km/h, the Doppler rate can reach values of 1 Hz/s.

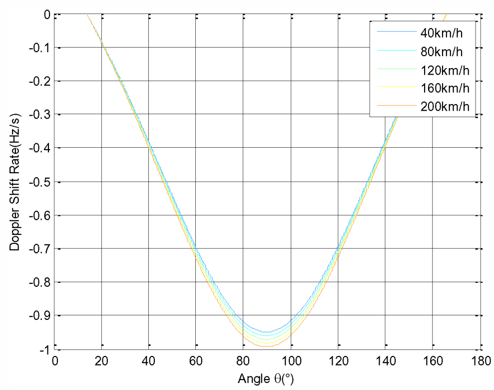

Figure 3.6: Simulated Doppler rate for a terrestrial user as a function of the elevation angle θ. Source [55]

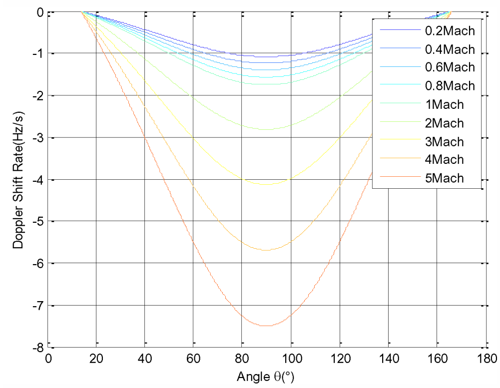

Figure 3.7: Simulated Doppler rate for a airborne user as a function of the elevation angle θ. Source [55]

Nevertheless, the study [55] reports also the simulation of receivers in space, in this case the Doppler rate can be much more relevant. As denoted in Figure 3.8, a receiver in MEO orbit can experience Doppler rates of approximately -1800 Hz/s

in the worst case scenario. Figure 3.8 shows the Doppler shift rate values for orbital altitudes ranging from 17,000 km to 20,000 km. Variations in orbital altitude significantly impact the absolute value of the Doppler rate.

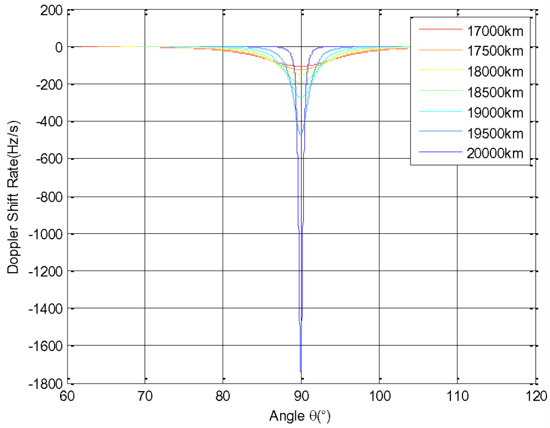

Figure 3.8: Doppler shift rate vs. elevation angle θ. Source: [55].

3.2 Requirements and architecture

Chapter 2 delineates the working principles of averaging techniques as proposed in the literature. It highlights that implementing an averaging technique suitable for realistic scenarios requires addressing several challenges, such as accurately compensating for the Doppler effect. However, for the sake of simplicity, the discussion in Chapter 2 does not account for data bit transitions or a non-zero Doppler rate. The scope of this section is to propose the implementation of an averaging technique capable of overcoming the following challenges:

- **Processing short batches of signal samples**. Certain applications may require to process only a few hundred of milliseconds of signal recordings. This is the case of the aforementioned LuGRE mission, in which there will be available only short batches of signal samples, due to the limitation of the system memory and of the downlink rate [56]. As a consequence, the applied processing methods should be able to efficiently extract information from the available samples. The time domain output of the processing technique should furnish the user with valuable data to ascertain the type and extent of distortion affecting the signal.

- **Dealing with low values of C/N_0**. The averaging process should efficiently retrieve the best possible results by leveraging all available samples, even in scenarios with low C/N_0 values.

- **Compensating for large Doppler shifts and Doppler rates**. The processing technique must effectively compensate for Doppler effects, which requires obtaining accurate estimates of both the Doppler shift and the Doppler rate.

- **Performing the processing with minimal or no external aiding**. Some methods depend on external assistance, such as prior knowledge of the Doppler shift, like in [28]. However, it is preferable to perform processing with minimal or no such assistance.

This thesis proposes an implementation of an averaging technique capable of meeting all these requirements. A comprehensive description of this processing methodology is presented in the following sections, while Figure 3.9 provides a graphical representation of the processing steps of the proposed method.

The processing begins with estimating the Doppler and Doppler rate values using a high-sensitivity acquisition stage. This stage evaluates an initial portion of the received signal, ranging from a few tens of milliseconds to over one hundred milliseconds. These estimated Doppler parameters are then used in the next stage, which estimates the Doppler value for the entire signal. Simultaneously, it identifies the transitions of data bits, which is essential for removing the navigation message bits. After removing the carrier by demodulating the signal with a linear chirp and eliminating the data bits by multiplying the signal by the bits identified in the previous steps, averaging can be performed. The signal, obtained by coherently accumulating several code epochs, is then processed by the Chip Domain Observable generator.

The analysis of the output of the processing technique proposed is reported in Chapter 4.

3.3 Acquisition stage

As with a standard GNSS receiver, the first step of processing involves acquiring the received signals, as detailed in section 1.6.3. To address low C/N_0 values, a high-sensitivity technique must be employed to achieve a correlation peak that is sufficiently prominent for detection. The primary objective of the acquisition stage is to estimate the Doppler shift affecting a given GNSS signal and the PRN code delay. This is accomplished by analyzing the peak of the CAF function, as described in section 1.6.3. If the peak is hidden by noise, it is impossible to accurately evaluate these quantities exploiting only the CAF. Among the high-sensitivity techniques reported in [57], the coherent time extension appears to be the best solution. Theoretically, it offers the highest performance compared to other techniques. For example, non-coherent time extension suffers from squaring

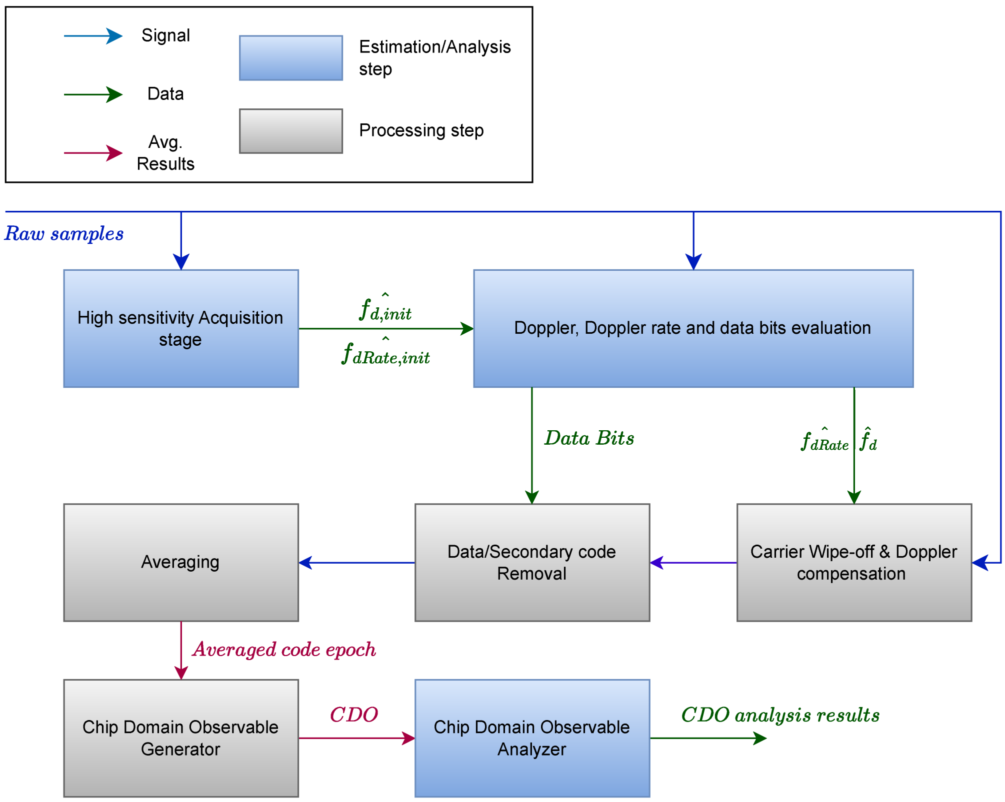

Figure 3.9: Diagram of the proposed processing technique.

loss, which limits the number of code epochs available for integration. The coherent time extension allows to increase the SNR of the correlator observable as described by the expression 2.18. In the following are reported the typical issues associated to the coherent integration time extension, together with the proposed solutions.

3.3.1 Coherent integration in presence of bit transitions

When extending the coherent integration time, it is crucial to account for bit transitions. These transitions can diminish or nullify the effect of coherent integration by introducing sign changes. Since the multiplication performed by the correlator does not eliminate all the sign changes introduced by the PRN code, the output of the sum is consequently reduced. A graphical representation of this behavior is presented in Figure 3.10.

When bit transitions occur, as in the case of the GPS C/A signal, it is necessary to evaluate and compensate for the bit values to achieve the maximum value of the

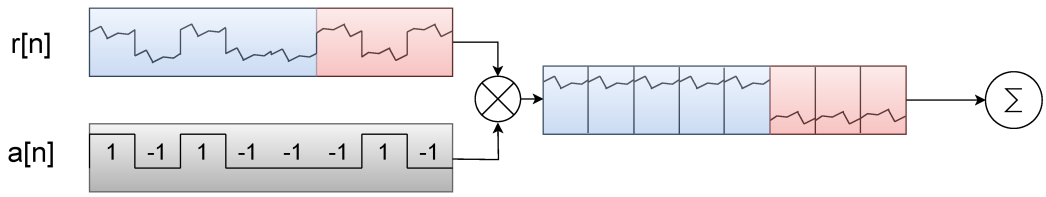

Figure 3.10: A graphical representation of the computation of the correlation value obtained when the received signal and the local code replica are ideally aligned in the time domain, but affected by a bit transition. Segments of the signals are highlighted in different colors to indicate data bits with opposite signs.

correlation function. Conversely, when dealing with a pilot channel, the secondary code is known, allowing the local code replica to compensate for it in advance. When evaluating bit values, it's beneficial to exploit the synchronization of the bit transitions with the PRN code initiation. Specifically, for the C/A signal, each bit persists for 20 consecutive epochs of the PRN code, corresponding to a duration of 20 milliseconds. Consequently, within this 20-millisecond interval, only one transition can occur, and it will be situated between the termination of one code epoch and the initiation of another. It is important to note that the absolute value of the bit sign is not relevant; what matters is the transition itself. As observed in Figure 3.11, when the sign of the local code is the opposite of the received signal's sign, the coherent accumulation sums all the samples with a negative sign. However, since the correlation value is typically squared, having the local code replica with the opposite sign of the received signal is equivalent to having the same sign.

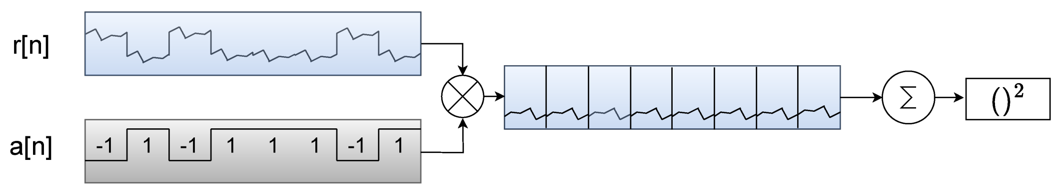

Figure 3.11: A graphical representation of the computation of the correlation value obtained when the received signal and the local code replica are ideally aligned in the time domain but exhibiting opposite polarity. The output of the correlator considered in the CAF is typically squared.

Accurately estimating the data bits requires identifying their correct combination and alignment. By focusing exclusively on transitions, the search space can be effectively reduced by half. For example, the sequence "-1 1 -1" is equivalent to the sequence "1 -1 1". In addition, utilizing a parallel approach for the correlation process enables simultaneous testing of all delay values. Furthermore, considering that the correlator performs circular correlation, it is possible to further constrain the search space. The number of distinct bit sequences requiring testing can be substantially diminished by recognizing that certain sequences are equals to the shifted version of other sequences. For instance, the sequence "-1 1 -1" is equal to the circularly shifted version of "1 -1 -1". Multiplying the local code replica with a given bit sequence, when the received signal is modulated by a sequence that corresponds to a shifted version of the local bit sequence, only changes the correlation peak delay τ by an integer number of code epochs. The bit sequence of the received signal can be derived considering the delay τ.

So, the CAF can also be extended to the bit search, utilizing the aforementioned properties to reduce the search space. The local replica can be multiplied by the reduced set of bit sequences for all the bins of the search space, then the combination of Doppler parameters and bit sequence leading to the highest correlation value can be selected to provide the correlator output, as described in section 3.3.4.

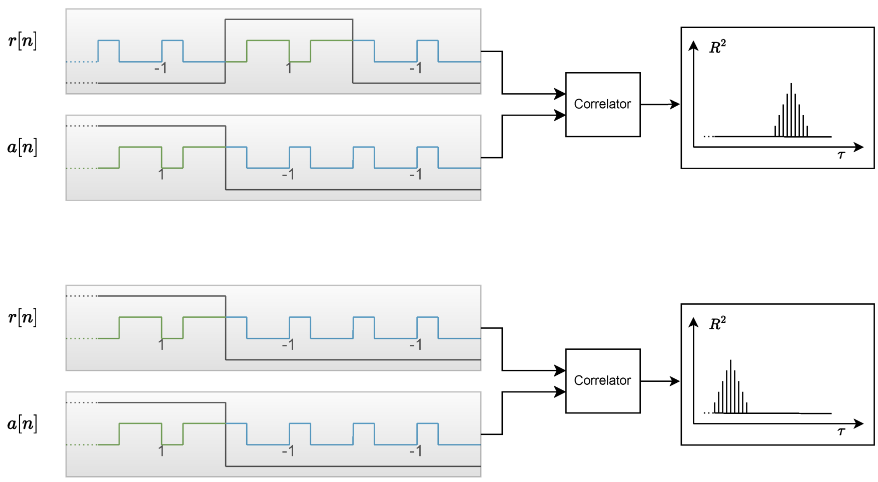

Figure 3.12: Pictorial representation of the circular correlation in presence of bit transitions. The code is represented by blue or green lines indicating bit polarity. The bits are reported in black.

A representation of the number of reduced bits with respect to the total number of bits in the search space is reported in Figure 3.13.

3.3.2 Acquisition in presence of a large Doppler shift on the code

The Doppler shift affecting the signals, also impacts the PRN code. Therefore, especially when dealing with high Doppler shift values, and with and extended coherent

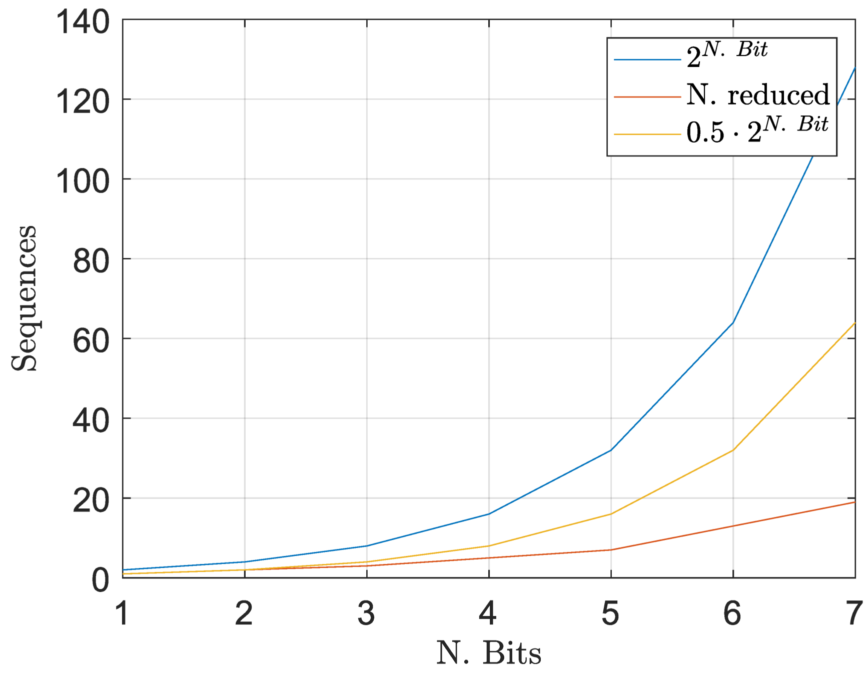

Figure 3.13: Comparison between the number of possible bits and the reduced set obtained without considering the sign and the circular shift.

integration time, it becomes necessary to adjust the local code replica to account not only for Doppler on the carrier but also for Doppler on the code. The presence of an uncompensated Doppler shift in the PRN code causes a misalignment between the local code replica and the received signal's code. This misalignment reduces the peak value of the correlation function, resulting in decreased performance of the acquisition stage. Figure 3.14 presents a graphical representation of the impact on the correlator of an uncompensated code Doppler shift on the received signal code. The illustration emphasizes the difficulty in correctly aligning the local code with the received signal, resulting in a compromised correlation value. The acquisition stage can compensate for the Doppler shift on the code adapting the rate of the local code replica.

The expression of the code rate affected by Doppler is:

$$R_D = R_{chip}(1 + \frac{f_D}{f_{carr}}) \tag{3.1}$$

where:

- R_{chip} is the nominal chip rate

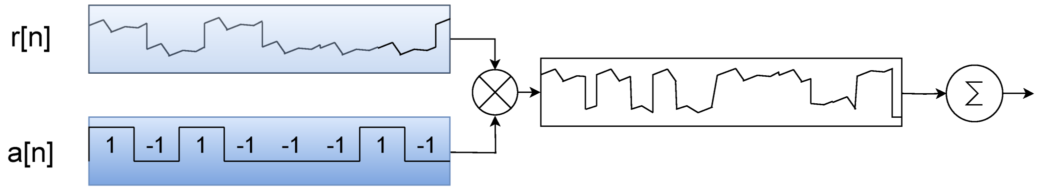

Figure 3.14: Visual representation of the correlation value computation process, performed aligning the received signal r[n] and the local code replica a[n] from the beginning, when the received signal has a chip rate lower than the nominal rate due to the presence of the Doppler shift.

- f_D is the Doppler shift affecting the carrier
- f_{carr} is the carrier frequency which in this thesis is f_{L1}.

Defining the Doppler on the code $f_{D,code}$ as:

$$f_{D,code} = \frac{f_D}{f_{L1}} R_{chip} \tag{3.2}$$

it is possible to state that the local code accumulates a shift, with respect to the received signal, of one sampling period T_s every $\frac{1}{f_{D,code} N_{sam/chip}}$. To compensate for the Doppler on the code, in the acquisition stage, it is enough to generate a local code replica with a chip rate defined accordingly to the expression 3.1. This can be done for all the Doppler shift values in the search space. Figure 3.15 presents a comparison of the correlation peaks for a GPS C/A complex signal with a C/N_0 of 50 dB-Hz, sampled at 25 MHz, excluding the presence of noise the signal is ideal and does not present the effects of the filtering. One peak is obtained by compensating for a constant 50 kHz Doppler shift on the carrier and on the local code, while the other is obtained without applying the correction of the Doppler on the local code. In both the cases, the coherent integration time is equal to 100 ms. Figure 3.15 highlights that compensating for the Doppler shift on the code yields a higher correlation peak. Additionally, the correlation peak obtained without Doppler compensation exhibits a noticeable shift in the delay τ. The peak of the correlation function obtained performing the Doppler compensation presents a much sharper peak, and an amplitude almost an order of magnitude larger with respect to the uncompensated case. The study [58], presents an extended analysis of the effects of the Doppler on the PRN code.

3.3.3 Acquisition in presence of a large Doppler rate

In the previous sections, the Doppler shift is assumed to be constant over time, anyway this is an approximation that holds only for short integration time values

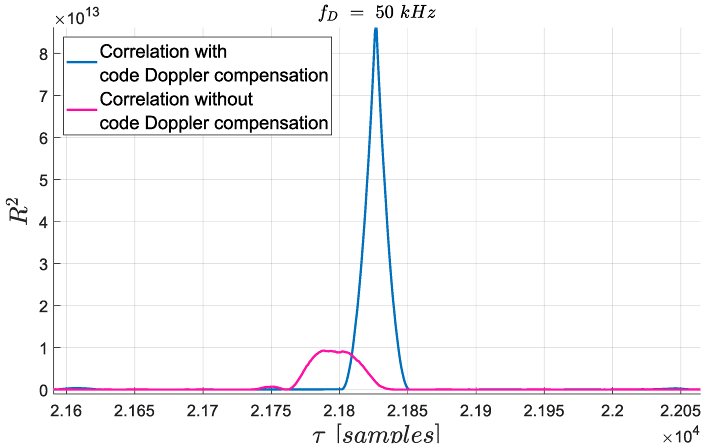

Figure 3.15: Comparison between the correlation function R^2 obtained with and without the code Doppler shift compensation. GPS C/A signal, sampled at 25 MHz, quantized on 8 bits.

and for a user with little or no dynamic on the Earth surface. The relative motion between the receiver and the GNSS satellites is characterized also by an acceleration component, leading to a change of the Doppler shift over time. A standard acquisition stage typically neglects the presence of the Doppler rate component, this because on Earth, terrestrial and airborne users rarely experience Doppler rate values higher than a few tens of Hz/s, as reported in [55]. For a terrestrial user, the effect of the Doppler rate is generally negligible. Extending the coherent integration time to half a second, for a static user on the surface of the Earth results in a maximum variation of 0.5 Hz in the worst case (assuming a Doppler rate of 1 Hz/s). According to the empirical rule, which sets the Doppler shift bin size to $\Delta_{f_D,bin} = \frac{2}{3 \cdot T_{coh}}$ (when estimating the CAF), the bin size in this instance would be $\approx 1.33\ Hz$, which is more than twice the variation in Doppler shift.

A robust acquisition stage may include a technique for Doppler rate compensation, which is crucial for signals with a low C/N_0 requiring long integration times under high Doppler rates. Instead of using a constant-frequency carrier for demodulation, the acquisition stage can utilize a linear chirp, as detailed in [59]. This extends the search space not only to the Doppler shift, but also to the Doppler rate. Using a linear chirp as the local carrier allows the carrier frequency to change linearly, matching the frequency variation of the received signal's carrier.

The expression of the linear chirp can be found considering the desired instantaneous frequency as:

$$f(t) = f_{init} + f_{D,rate}t \tag{3.3}$$

where:

- f_{init}: is the initial frequency: $f_{init} = f_c + f_{D,init}$, where $f_{D,init}$ is the initial Doppler shift.
- $f_{D,rate}$: is the Doppler rate in Hz/s.

Starting from expression 3.3, the phase ϕ of the chirp is:

$$\begin{aligned} \phi &= \phi_{init} + \textstyle\int_0^t f_{init} + f_{D,rate}t \; dt \\ \phi &= \phi_{init} + 2\pi(\tfrac{1}{2}f_{D,rate}t^2 + f_{init}t) \end{aligned} \tag{3.4}$$

The expression of the complex linear chirp can be written as:

$$C_{linear}(t) = exp[j2\pi(\frac{1}{2}f_{D,rate}t^2 + f_{init}t) + \phi_{init}] \tag{3.5}$$

The acquisition stage can compensate for the Doppler rate by employing FFT-based parallel code phase correlation, testing various values not only of Doppler shift but also of Doppler rate.

The CAF obtained by considering the Doppler rate, Doppler shift and the delay τ, can be visualized by plotting only the maximum value of correlation obtained for each combination of Doppler shift and Doppler rate. Figures 3.16 and 3.17 depict a slice of the CAF for a GPS C/A signal subjected to a Doppler rate of 800 Hz/s and an initial Doppler shift of 500 Hz. The signal is complex, has a C/N_0 of 60 $dBHz$, is sampled at 25 MHz, and is quantized to 8 bits. Excluding the presence of noise, the signal is considered ideal, meaning the effects of filtering are not taken into account. The coherent integration times utilized in Figures 3.16 and 3.17 are 60 ms and 100 ms, respectively.

The CAF exhibits a peak in the correct bin corresponding to $f_{D,rate} = 800\ Hz/s$ and $f_{D,init} = 500\ Hz$. As the coherent integration time, T_{coh}, varies, the behavior of the CAF changes, the tilt present in Figure 3.16, with respect to the Doppler and Doppler rate axis, is more evident when extending the coherent integration time, as shown in Figure 3.17. The behavior of the obtained function illustrates how a variation in the initial Doppler shift value $f_{D,init}$ influences the estimate of the Doppler rate, and conversely. For example, when the coherent integration time is smaller, a small variation of the initial Doppler can be compensated by choosing a Doppler rate with a larger absolute value, with respect to the case in which the coherent integration time is longer.

3.3.4 Complete acquisition scheme

The proposed acquisition stage is illustrated in Figure 3.18. As it is possible to notice, this stage compensates for Doppler effects on both the code, by adapting the local code rate, and on the carrier, by utilizing a linear chirp $C_{linear}(t)$. Additionally, to extend the coherent integration time, it addresses the presence of navigation

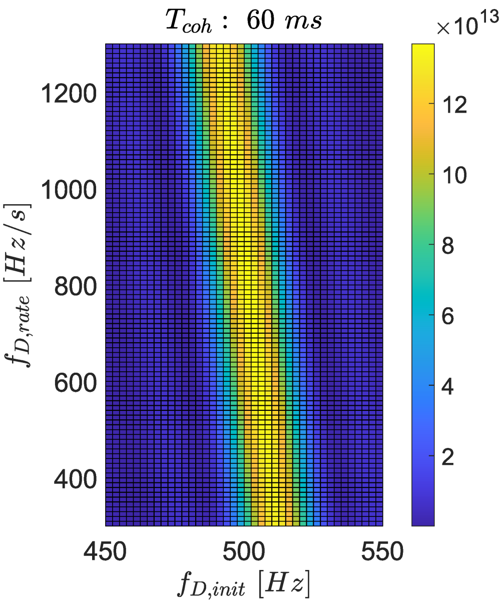

Figure 3.16: Maximum correlation value R^2 for the shown Doppler and Doppler rate values, with resolutions of 2.5 Hz and 10 Hz/s, respectively. The coherent integration time T_{coh} is 60 ms.

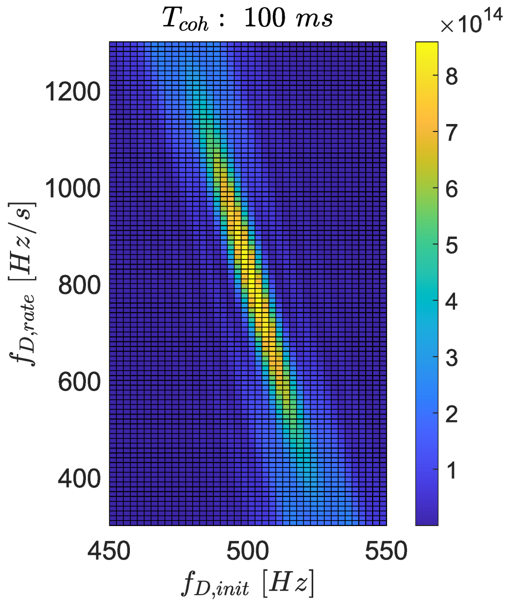

Figure 3.17: Maximum correlation value R^2 for the shown Doppler and Doppler rate values, with resolutions of 2.5 Hz and 10 Hz/s, respectively. The coherent integration time T_{coh} is 100 ms.

message bits by multiplying the local code by a bit sequence from the reduced set of possible bit sequences. The combination of Doppler shift, Doppler rate, and bit sequence that results in the highest correlation peak value is then used as the estimate for these quantities. The size of the search space depends on the specific application use case. For example, for a stationary user on the Earth's surface, extending the search space in the Doppler rate domain may be unnecessary. A static receiver is unlikely to encounter Doppler rate values exceeding 1 Hz/s in absolute terms.

Additionally, if the receiver can utilize some sort of augmentation system the search space can be reduced by exploiting additional data, for instance the receiver may define a smaller search space for the Doppler shift if an estimate is already provided by an external source.

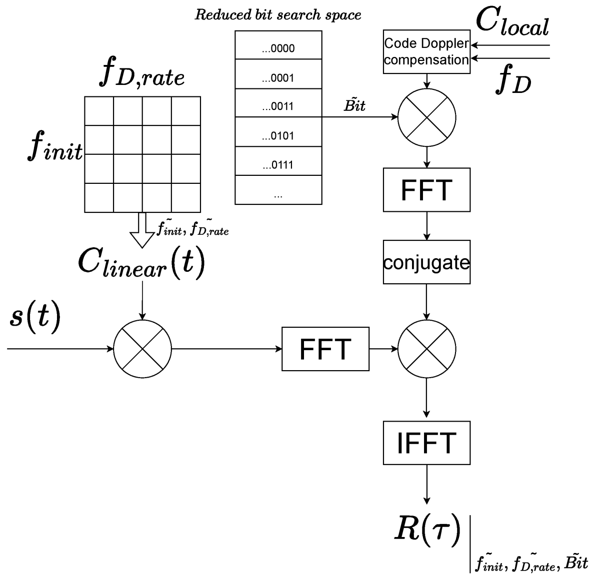

Figure 3.18: Schematic view of the proposed acquisition stage.

3.4 Data bit removal and Doppler shift estimation

The procedure carried out during the acquisition stage can be extended to the entire signal to obtain estimates of the data bits, as well as the Doppler shift and Doppler rate. This procedure is necessary to be able to properly remove the residual carrier and the data bits, such that the signal can be then processed through the averaging stage. The signal can be segmented into chunks, with each chunk being processed using the acquisition stage outlined in earlier sections. The size of these chunks is determined by the desired coherent integration time. Particular attention should be given to the obtained bits, as independently estimating the bits for each chunk may result in sign ambiguity between consecutive signal blocks.

To address this issue, a correlation is performed for each new block of bits, also taking into account the previous signal chunk. This involves concatenating the bit sequence of the previous signal block with the current bit sequence in two ways: once without any changes and once with a sign inversion of the current bit sequence, resulting in two sequences. The correlation is then computed two more times, using both sequences: one obtained by concatenating the new bits with an inverted sign, and the other without sign inversion. The sequence that yields the highest correlation indicates the correct sign. A graphical representation of this process is reported in Figure 3.19. In particular, the figure shows two sample batches of the received signal, $r_1[n]$ and $r_2[n]$. The bit modulating the $r_1[n]$ and $r_2[n]$ signal are, $bit_1[n]$ and $bit_2[n]$. Each block is processed independently by the acquisition process. The correct bit sequence is determined by considering the sign hypothesis that leads to the maximum peak value of the correlation R.

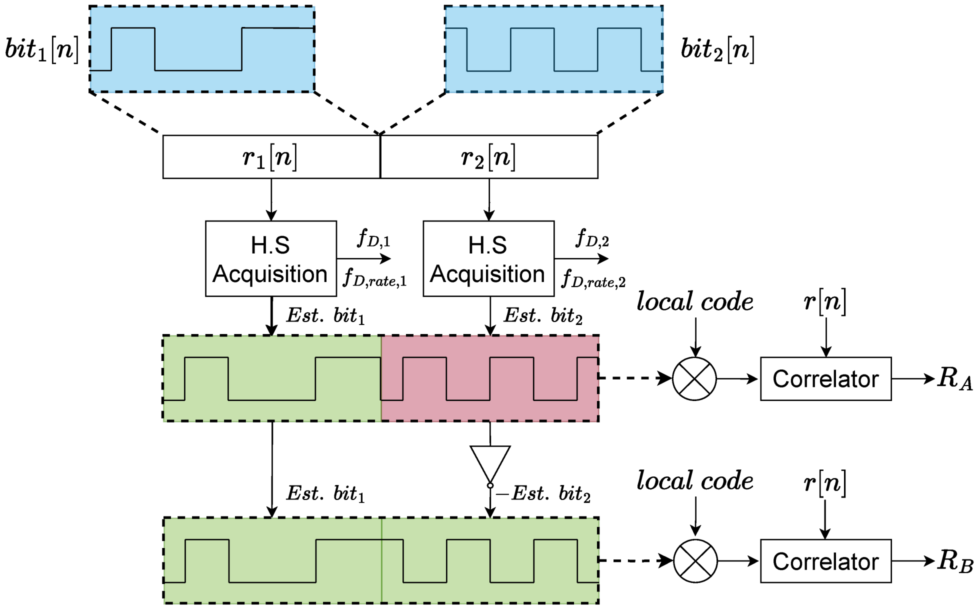

Figure 3.19: Resolution of the sign ambiguity.

The signal chunks can be processed sequentially. This allows each step in the acquisition stage to leverage the output of the previous step to reduce the Doppler search space. When the coherent integration time is around 100 ms, many Doppler rate values produce high correlation peaks, as it is possible to notice from Figure 3.17. This means that the Doppler rate estimate may be particularly noisy. However, high correlation peak values for various combinations of Doppler rate and Doppler shift, not just the optimal bin pair, allow for compensation of both Doppler rate and Doppler shift. This is effective even when the selected pair of values is not the true value bin but a close one.

A pictorial representation of the search space, for what concerns the Doppler and Doppler rate, is shown in Figure 3.20. Each pair of Doppler and Doppler rate values can be represented as a line in the Time-Frequency plot. During the first coherent integration time period, the acquisition stage can conduct a search within a specified search space. For the second signal block, spanning from T_{coh} to $2T_{coh}$ a narrower range of Doppler shift values can be selected based on the estimate obtained in the previous step. Some margin should be considered to accounts for

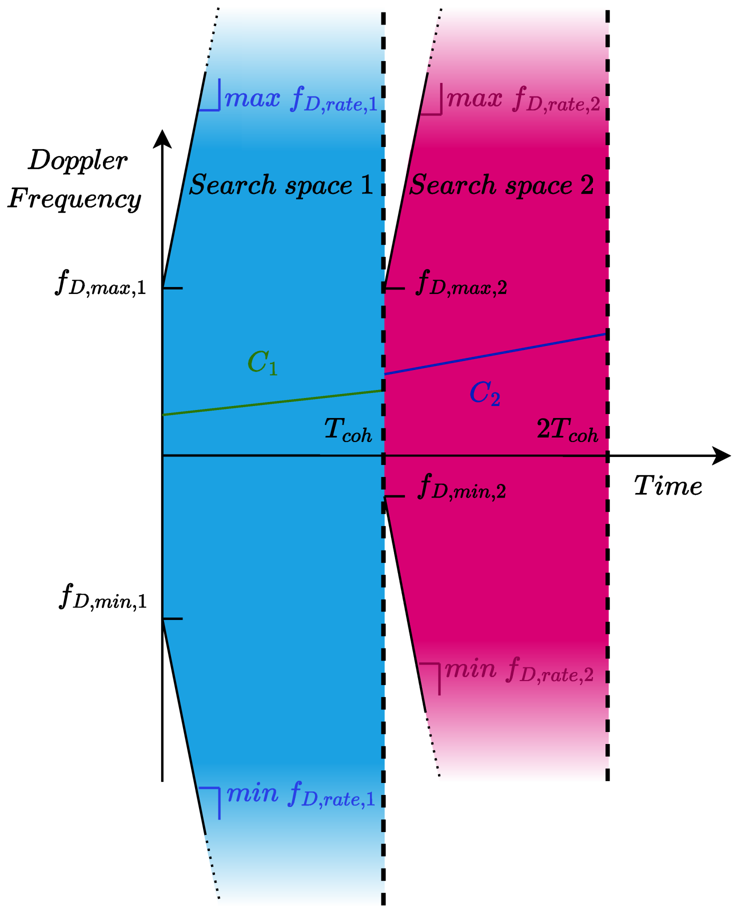

Figure 3.20: Pictorial representation of the search space reduction principle. The green and blue lines, C_1 and C_2, represent the optimal carriers found by the acquisition stage for the first and second signal blocks, respectively.

the possible errors on the estimates obtained at each step. This method can also be applied to the search spaces of other signal chunks.

The estimated Doppler values can then be used to construct the local carrier for the de-chirping process. For coherent integration times spanning a few hundred milliseconds, the Doppler shift can be assumed to vary linearly over time. Consequently, the carrier can be generated by selecting Doppler and Doppler shift values $\bar{f}_D$, and $\bar{f}_{D,rate}$, derived from a linear fit of the estimated Doppler values. Subsequently, it is possible to start the averaging process.

3.5 Averaging stage

The first processing step to be performed on the raw signal is the carrier wipe-off. Leveraging the knowledge of the Doppler rate and Doppler shift obtained in the previous steps ($\bar{f}_D$ and $\bar{f}_{D,rate}$), the carrier wipe-off can be performed demodulating the received signal utilizing a linear chirp. Anyway, to evaluate in the time domain the signal it is also necessary to assess the presence of a residual phase shift ϕ_0. An estimate of the residual phase shift can be found by testing several values of the initial phase $\hat{\phi}_0$ and performing the carrier wipe off. This process is represented graphically in Figure 3.21. The demodulated signal ($r_{base}[n]$), leading to the highest value of correlation with the local code replica, is then prompted to the successive processing steps.

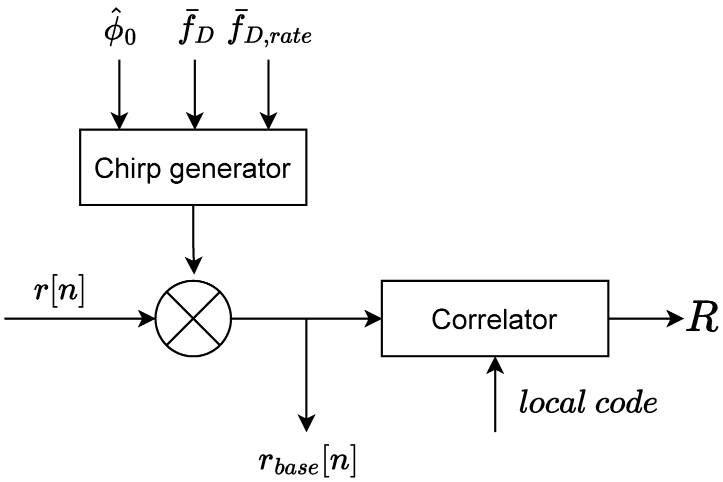

Figure 3.21: Demodulation of the whole received signal performed utilizing a linear chirp with initial phase shift $\hat{\phi}_0$.

After the carrier wipe-off, it is possible to remove the bit transition by multiplying the obtained signal with the bits found in the previous steps. Anyway, the signal obtained may be still affected by a Doppler shift on the code, so all the samples are relabeled, such that each code epoch in the signal has a nominal duration.

Averaging can be conducted using the binning technique reported in section 2.2.4. After selecting the desired bin width, the relabeled samples can be stored in the code-phase bins and then accumulated. To do so, the re-computed (Doppler compensated) time of arrival of each sample is prompted to a modulus after division operator (introduced by the expression 2.11). In this way, if a sample presents a

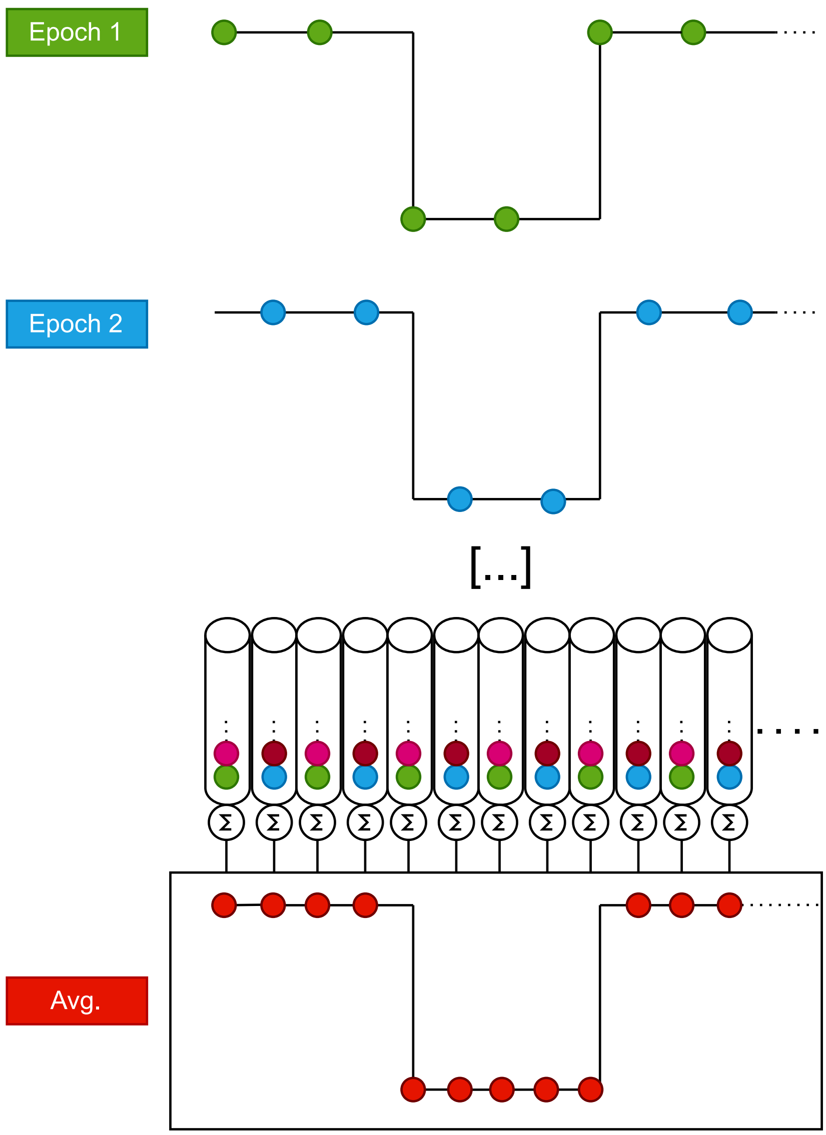

Figure 3.22: Graphical representation of the code averaging process. The relabeled samples from different code epochs are overlapped and mapped to the corresponding code-phase bins, the sum of the values in each bin represent the sample of the de-noised code epoch with the corresponding code phase.

time of arrival $K \cdot T_{epoch} + \delta t$, where K is integer and T_{epoch} is the duration of one code epoch, the code-phase of the sample computed by the modulus after division operator is δt. The sample will then be mapped to the appropriate code-phase bin.

This process produces a single code epoch with an improved SNR, and depending on the code-phase width, also enhanced time resolution. Time resolution can be increased by selecting smaller bin widths; however, this reduces the number of samples per bin. If the total number of processed samples remains the same, this will result in a noisier output. Assuming a good estimation of the Doppler values, the user can control the maximum code-phase error introduced by the binning process by selecting accordingly the bin width.

3.6 Chip Domain Observable (CDO) generation

The chip domain observable, discussed in section 2.2.5 facilitates additional noise reduction. To achieve this, averaging chip transitions involves coherent alignment of transitions with the same polarity, such as grouping all rising edges together. By knowing the PRN code and having an estimate of the delay τ obtained through correlation of the local code with the averaged sequence, it becomes possible to identify all rising and falling edges present in the averaged signal, even when individual chips are not distinctly visible. In this implementation the CDO is obtained starting from the output of the code averaging process, so the obtained averaged code can be correlated with a replica of the local code to obtain the estimate of the code delay $\hat{\tau}$, and so the positions of the transitions of the chips.

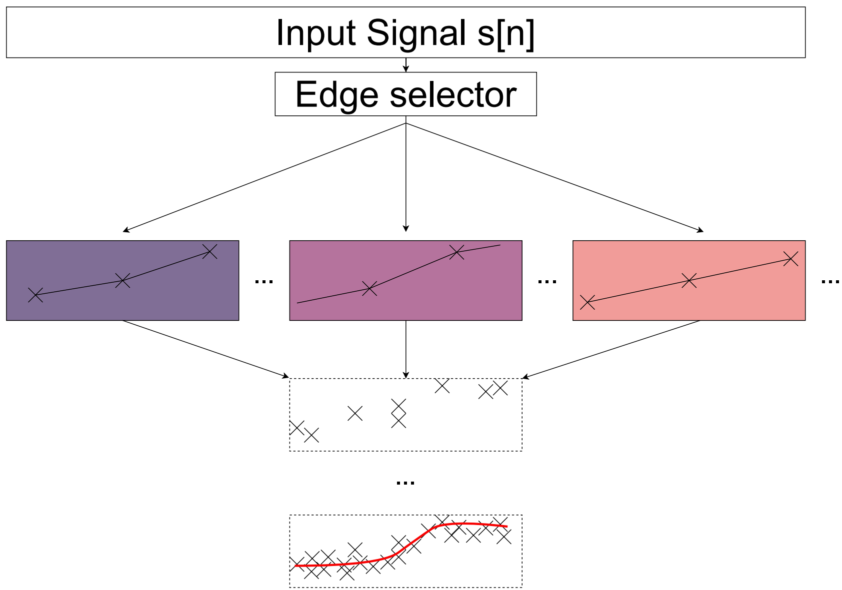

Figure 3.23: Pictorial representation of the chip domain observable generation process starting from a generic input signal s[n]. The red curve represents the sliding mean of the overlapped samples.

After having selected the rising and falling edges, it is possible to overlap them together as described in Figure 3.23. As it is possible to notice from Figure 3.24, where an example of the possible obtained result is shown, the samples does not overlap perfectly, resulting in a sort of cloud of points.

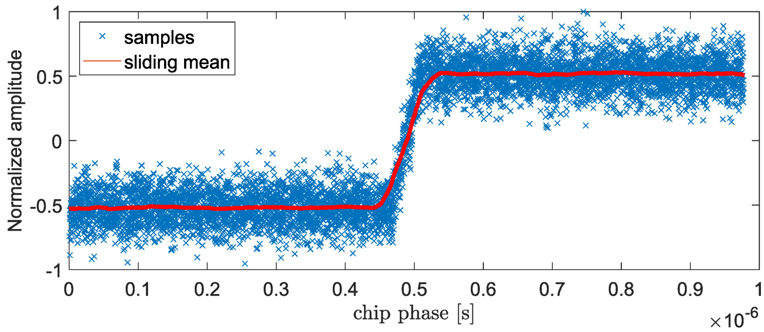

Figure 3.24: Example of a possible chip domain observable obtained processing the output of the code averaging process. The samples of the chip transitions of the code obtained averaging N code epochs are reported in blue, while the sliding mean of the obtained samples is reported in red. Original signal: GPS C/A, Bin width: 0.5 *samples*, sliding window length: 400 samples, f_s of the original signal: 25 MHz, $C/N0$ of the original signal: 60 dBHz.

To obtain an increased SNR is necessary to perform some kind of averaging, so for this reason, in this thesis, it is proposed to utilize a sliding mean to average the obtained set of points. The sliding mean window can be selected considering the desired level of dynamic of the output and the desired noise reduction. The user can now process the averaged output to obtain the chip domain observable. The primary parameters the user can adjust are the size of the bins used in the code averaging process and the length of the sliding mean window used for generating the chip domain observable. Using very narrow bins in the code averaging phase introduces a small error due to the binning process. However, this comes at the cost of a noisier output compared to using larger bins in the time domain. On the other hand, selecting a larger sliding mean window allows to obtain a smooth CDO, at the cost losing the high frequency features. Therefore, the user must balance noise reduction with the ability of visualizing high frequency features.

It is crucial to note that in the proposed processing chain, the input raw samples undergo no filtering prior to averaging. This approach is justified by the removal of carrier residuals and other spurious frequencies through both the averaging process and the sliding mean used to derive the chip domain observable. Filtering has a harmful effect on signal quality analysis by altering signal characteristics and complicating the observation of high-frequency features. Being able to control the amount of filtering applied to the signal during processing is essential to obtain optimal results.

Chapter 4

Experimental results

In this chapter are reported the results obtained processing both synthetic and real signals with the proposed signal processing chain.

4.1 Averaging Technique: Results

This section, along with the following ones, presents the findings obtained by averaging GNSS signals using the previously described methodology, in particular, it focuses on the analysis of a set of synthetic GNSS signals generated using the N-FUELS tool [60]. This program enables the generation of GNSS signals with a wide variety of selectable parameters, such as sampling frequency, Doppler shift, Doppler rate, and the $C/N0$ value. The N-FUELS tool has been developed by the Navigation Signal Analysis and Simulation (NavSAS) group.

The first signal reported is a GPS C/A signal with a $C/N0$ of 60 $dBHz$ and affected by a constant Doppler shift of 500 Hz. For all the signals discussed in this section, the sampling frequency is 25 MHz. The generated signal is complex, and the quantization is performed on 8 bits, emulating an 8-bit ADC. The Intermediate Frequency (IF) at which the signal is centered is 0 Hz, so the only component of the carrier is due to the presence of the Doppler shift. The receiver front-end effect is omitted for simplicity during signal generation. Subsequent sections present results obtained from processing signals sampled using a Software Defined Radio (SDR), and so also considering the effects of front-end filtering. Before presenting the results of the averaging process, Figure 4.1 displays the first 300 samples of the signal, which is entirely buried in noise.

A portion of the obtained averaged code epoch is reported in Figure 4.2. As shown, the chip transitions are highly distinct and visible after the accumulation of 200 code epochs.

Generating a signal with a $C/N0$ of 50 $dBHz$, which is 10 $dBHz$ lower compared

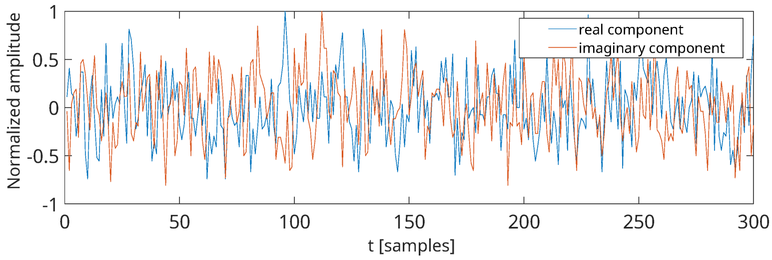

Figure 4.1: Real and imaginary component of the first 300 samples of the signal with normalized amplitude, before the processing.

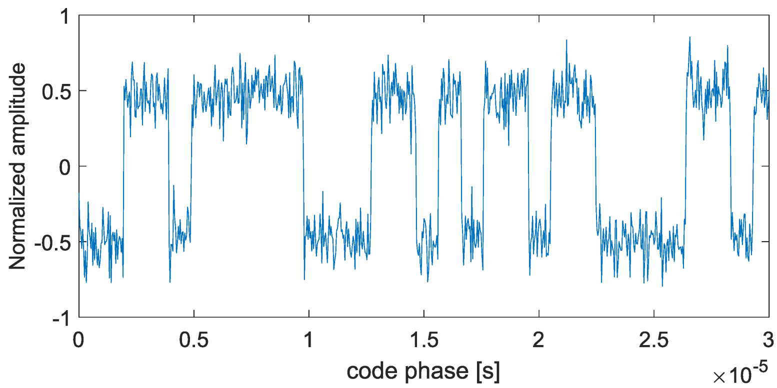

Figure 4.2: The first 0.03 ms of the average code epoch (GPS C/A 1 ms) obtained as output from the averaging process. Input $C/N0 = 60$ dBHz, $T_{acc} = 200$ ms, $f_s = 25$ MHz, $f_D = 500$ Hz, $f_{D,rate} = 0$ Hz/s.

to the previous case, and accumulating the same number of code epochs, allows to observe the influence of noise on the averaged signal, as depicted in Figure 4.3.

To counteract the effect of the noise it is necessary to increase the number of accumulated code epochs, indeed, accumulating 600 code epochs allows for a better visualization of the signal also when the $C/N0$ is lower, as shown in Figure 4.4.

Analyzing a synthetic signal with a $C/N0$ of 45 dBHz, as shown in Figure 4.5, reveals that the noise reduction achieved through code averaging might be insufficient, especially when the number of available code epochs accumulated is limited to 300.

Studying solely the averaged code may be insufficient when dealing with signals with lower values of $C/N0$, so to extract more information from the given set of samples it is necessary to generate the chip domain observable.

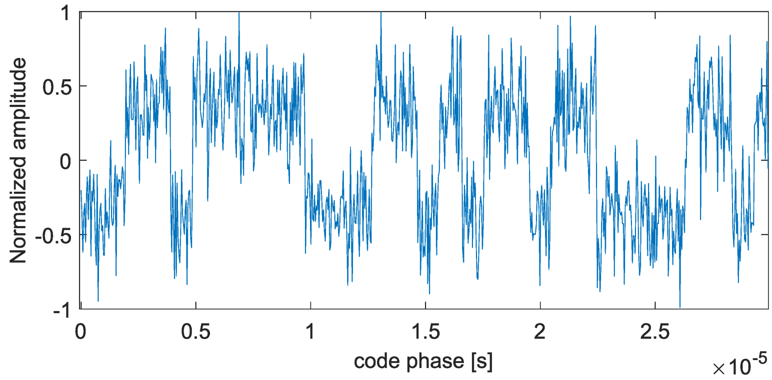

Figure 4.3: The first 0.03 ms of the average code epoch (GPS C/A 1 ms) obtained as output from the averaging process. Input $C/N0$ = 50 dBHz, T_{acc} = 200 ms, f_s = 25 MHz, f_D = 500 Hz, $f_{D,rate}$ = 0 Hz/s.

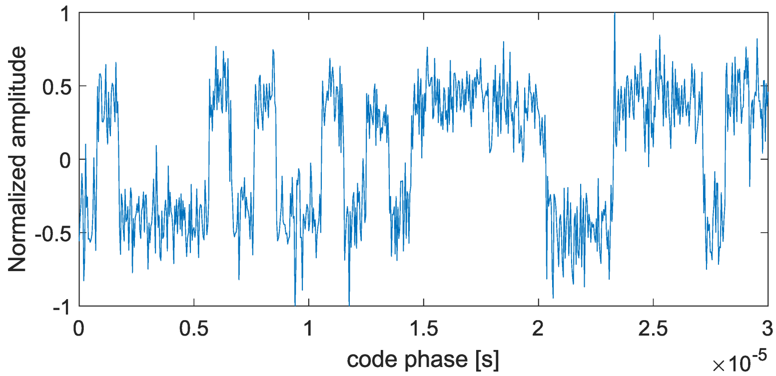

Figure 4.4: The first 0.03 ms of the average code epoch (GPS C/A 1 ms) obtained as output from the averaging process. Input $C/N0$ = 50 dBHz, T_{acc} = 600 ms, f_s = 25 MHz, f_D = 500 Hz, $f_{D,rate}$ = 0 Hz/s.

4.2 CDO: general results

This section presents the results obtained from processing both synthetic and real signals. The first part of this section analyzes a synthetic GPS C/A signal sampled at 25.575 MHz and quantized to 8 bits with a $C/N0$ of 50 dBHz, both in the presence and absence of Doppler. The second portion of the current section introduces instead the study of CDOs of real signal, obtained sampling a GNSS signal with a SDR.

Figure 4.6 reports the chip domain observable obtained processing the output of the code averaging process, the original signal is a 50 dBHz GPS C/A signal,

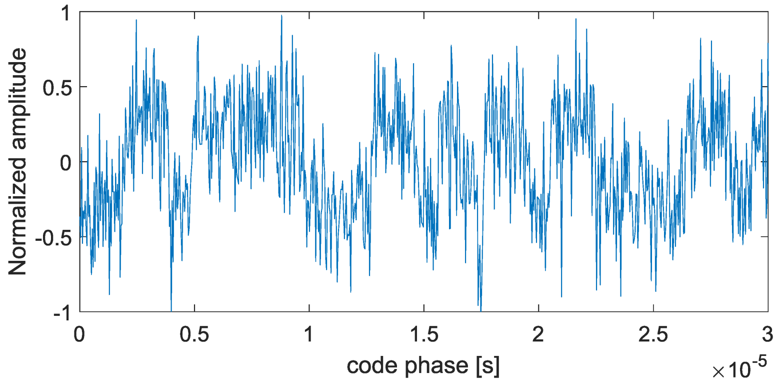

Figure 4.5: The first 0.03 ms of the average code epoch (GPS C/A 1 ms) obtained as output from the averaging process. Input $C/N0 = 45$ dBHz, $T_{acc} = 300$ ms, f_s = 25 MHz, $f_D = 500$ Hz, $f_{D,rate} = 0$ Hz/s.

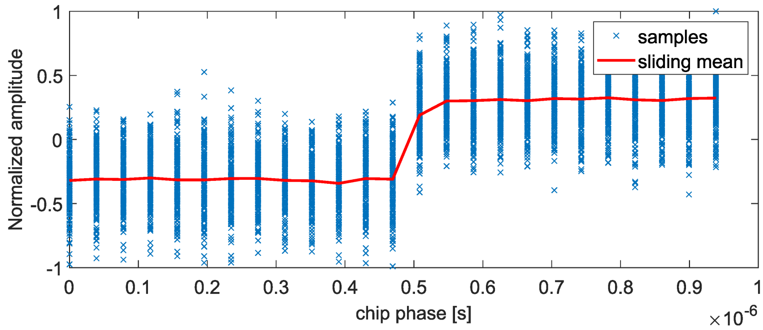

Figure 4.6: Chip domain observable obtained processing the output of the code averaging stage. Original signal: GPS C/A, $C/N0$: 50 dBHz, f_s: 25.575 MHz, T_{acc}: 300 ms, Bin width: 0.5 samples, Doppler shift: 0 Hz

sampled at a rate which is 25 times the code chip rate ($25 \cdot$ 1.023 MHz) and with a null Doppler shift. The figure shows the averaged signal samples obtained from the previous processing step in blue and the chip domain observable (CDO) in red, which is generated using a sliding mean with a 400-sample window. The picture exhibits clusters of samples, this phenomenon occurs because, in the absence of a significant Doppler component, the samples from different rising edges align perfectly, given that the number of samples per chip is an integer.

When instead a Doppler shift is present, even if the sampling frequency is a multiple of the chip rate, it is possible to enhance the resolution in the time domain by selecting a narrower bin size during the code averaging phase. Figure 4.7 shows an example where the signal under test has the same properties as the previous example, except for a Doppler shift of 2500 Hz. In this case the bin width selected is 0.2 samples. By maintaining the same sliding mean window size, the resulting observable exhibits more noise compared to the previous scenario, yet it concurrently achieves higher time domain resolution.

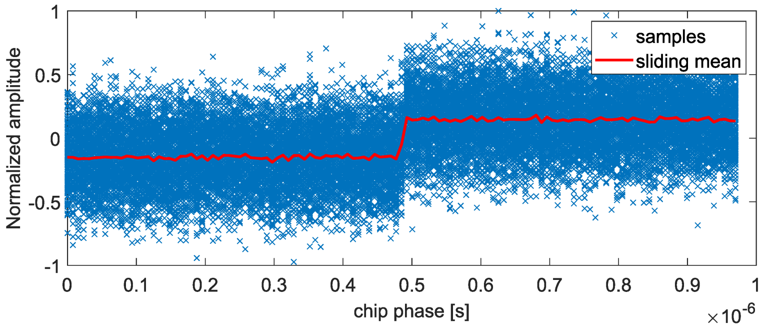

Figure 4.7: Chip domain observable obtained processing the output of the code averaging stage. Original signal: GPS C/A, $C/N0$: 50 dBHz, f_s: 25.575 MHz, T_{acc}: 300 ms, Bin width: 0.2 samples, Doppler shift: 2500 Hz

Figure 4.7 also highlights that the chip domain observable can be obtained even if the chip transitions of the averaged code, which are fed into the CDO generator (with the input samples shown in blue), are not clearly distinguishable.

To better evaluate the capabilities of the proposed processing chain, in the following are reported the results obtained generating the CDO starting from a real-world signal, sampled with a SDR. In particular, the signal has been obtained with the setup described in Figure 4.8.

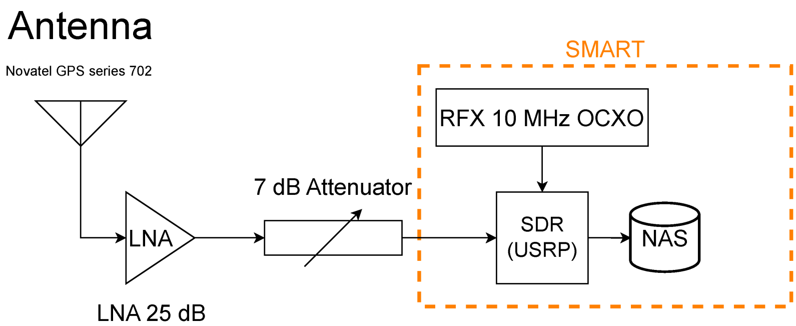

Figure 4.8: Description of the setup utilized to obtain a real GNSS signal.

The setup consists into a receiving antenna, placed on the rooftop of a building, so without impairments in the nearby area, the signal is amplified with a 25 dB gain LNA and then attenuated with a tunable attenuator to obtain a signal with a lower power. The signal is then sampled with a SDR, in particular the Ettus Research™ USRP. The description of the SMART station is reported in [61].

Figure 4.9 shows the CDO obtained processing the signal received with the SDR, sampled at 25 MHz and quantized on 16 bits. In particular, the GPS C/A PRN with the highest C/N_0 at the time of recording, which is estimated to be around 49 dBHz. The chip shape presents the typical overshoot at the end of the rising edge, and the smoothing operated by the sliding mean seems to be able to reduce the noise, while, at the same time keeping the signal features.

The averaging technique proposed is capable of extracting the different distinct signals present in the received, indeed, the orthogonality is guaranteed by the Doppler shift and by the differences in the carrier phase of the signals from different satellites. By selecting the appropriate local code replica, it is possible to retrieve the desired signal. This involves estimating the Doppler shift, Doppler rate, and initial phase of the signal, and then performing carrier wipe-off.

In Figure 4.10, and 4.11, are reported the results obtained processing two of the signals present in the recording, with a $C/N0$ of about 44 and 38 dBHz respectively. The CDO observable obtained is still smooth even if the $C/N0$ is much lower than the one of the previous case.

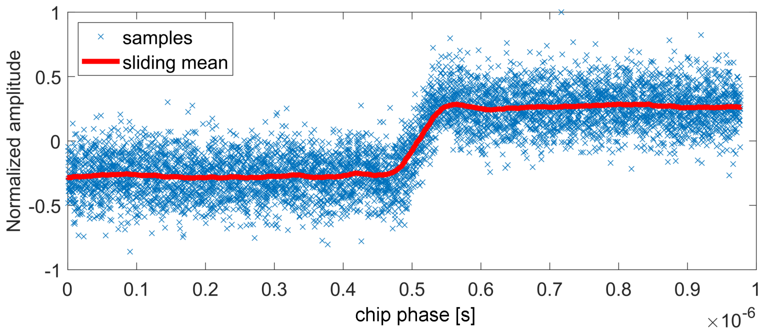

Figure 4.9: Chip domain observable, rising edge. Input signal: GPS C/A, PRN 21, f_D $\approx$ -1180.5 Hz, $C/N0$ $\approx$ 49 dBHz, f_s: 25 MHz, Bin width: 1 sample, Sliding mean window: 400 samples, T_{acc} = 300 ms.

4.3 Two ray multipath simulation

The receiver front end impacts the received signal, especially through filtering, which may obscure some features while introducing others. To study the effects of distortions like multipath, it is essential to process a realistic signal. Multipath is anticipated to cause distortions in the chip transition, which are generally influenced by filtering effects.

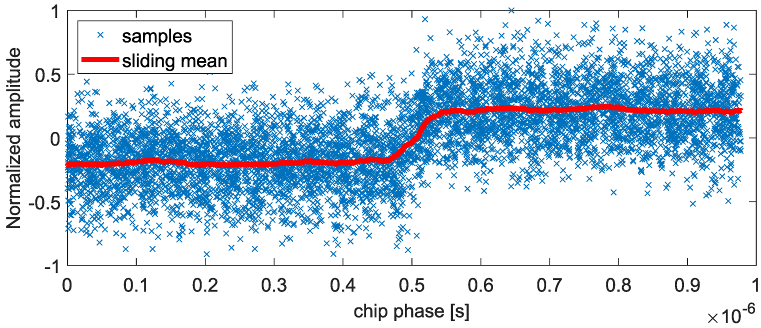

Figure 4.10: Chip domain observable, rising edge. Input signal: GPS C/A, PRN 3, $f_D \approx 1983$ Hz, $C/N0 \approx 44$ dBHz, f_s: 25 MHz, Bin width: 1 sample, Sliding mean window: 400 samples, $T_{acc} = 300$ ms.

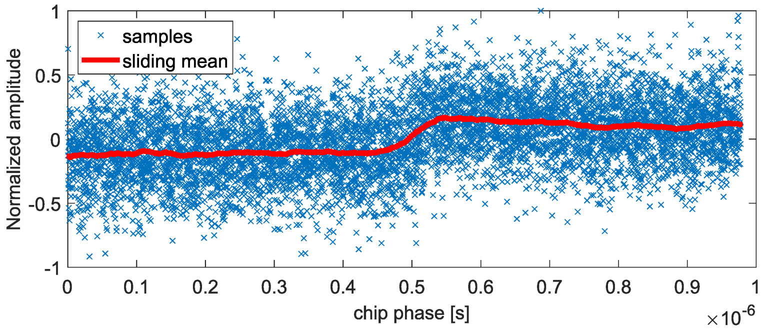

Figure 4.11: Chip domain observable, rising edge. Input signal: GPS C/A, PRN 22, $f_D \approx$ -71.3 Hz, $C/N0 \approx 38$ dBHz, f_s: 25 MHz, Bin width: 1 sample, Sliding mean window: 400 samples, $T_{acc} = 300$ ms.

To evaluate the capabilities of the proposed processing technique, in the following are reported the results obtained introducing two-ray multipath in the signal under test by altering a real signal. This should allow to include the front end filtering effects. Although the two-ray model is limited and does not account for factors such as the dynamics between the receiver and the environment or the presence of multiple delayed signal copies, it remains a good starting point for this analysis. A receiver might receive a direct line-of-sight signal and a delayed version reflected by the ground. In such cases, this model can still adequately represent the phenomenon.

To generate, in a controlled manner, the effect of a second delay copy of the signal, it is utilized the setup reported in Figure 4.13. The two antennas, positioned closely together on the rooftop of a building, placed in a way that should allow to minimize multipath, ensuring that the signals they receive are assumed to be free from multipath effects, or at least with a very small mulipath contribution. The

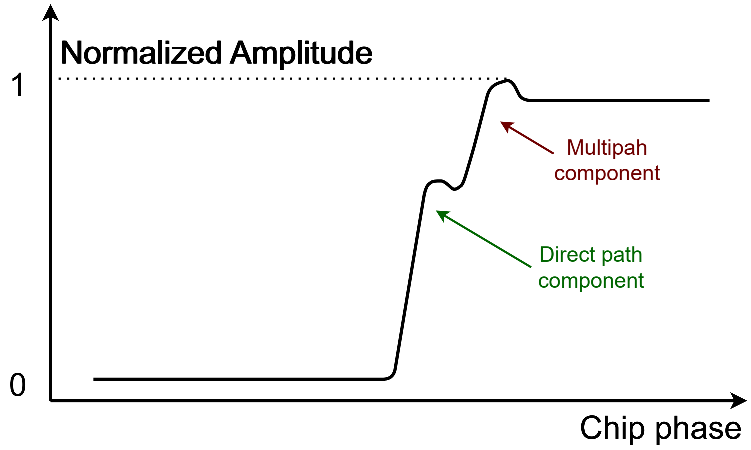

Figure 4.12: A visual representation of the expected impact of two-ray multipath on the chip shape.

signals travel through two cables of nearly equal length. One signal is amplified using an LNA with higher gain compared to the one amplifying the other signal. The signal from the second LNA travels through a 25-meter cable before being combined with the "direct" signal. A tunable attenuator is utilized to control the power of the stronger 'direct' signal. Two USRPs are used to almost simultaneously sample the 'direct' and 'multipath' signals, allowing for a comparison between the line-of-sight signal and its multipath-injected version. There may be a slight delay of a few milliseconds between the starting point of the recordings of the two SDRs. The setup of the SDRs follows the SMART architecture reported in [61], both the SDRs are disciplined by the same 10 MHz oven controlled crystal oscillator.

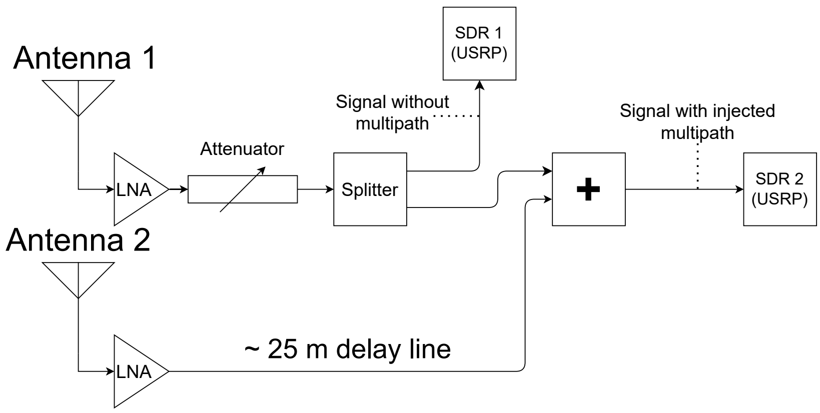

Figure 4.13: Setup employed for the multipath injection.

The tunable attenuator is adjusted so that the power difference between the line-of-sight signal and the delayed signal, both within a 4 MHz bandwidth, is about 1 dBm. In particular, the signal without multipath has a power of -84.87 dBm, while the delayed signal has a power of -85.7 dBm. The measurement is conducted by connecting a spectrum analyzer to the output of the signal adder. One measurement is performed with only the 25 m cable connected, while another is performed with only the cable coming from the splitter. It is important to remark that the received signals from the antennas include transmissions from all satellites within radio visibility, encompassing not only GPS satellites but also those from other constellations. By employing two different antennas and LNAs, two distinct signals at the input of the signal adder are obtained. These signals are influenced by different thermal noise and possess distinct random carrier phases. This setup allows the injection of a more realistic multipath effect. Table 4.1 describe briefly the datasets obtained with the aforementioned setup. The quantization is always performed using 16 bits.

Dataset	f_s **MHz**
A	25
B	12.5
C	5

Table 4.1: Overview of the datasets acquired with the aforementioned setup.

4.4 CDO of signals affected by multipath

In this section are reported the results obtained processing the signals generated with the setup previously described in section 4.3. Table 4.2 presents the C/N0 values for three GPS C/A signals, present in all the dataset acquired; specifically, those associated with the PRNs 21, 17, and 22. These values of $C/N0$ are estimated considering the dataset A. The table serves to compare the noise levels of each signal. However, C/N0 variations may arise from differences in the time periods over which the samples were taken. All datasets with different sampling frequencies were collected within the same 15-minute window. Therefore, to accurately compare the noise levels of different signals, it is still better to use signals from the same data set, to maintain consistency. Each data set is obtained fixing the value of sampling frequency f_s and the number of quantization bits.

Figures 4.14, 4.15, and 4.16 present a comparison between the CDOs obtained from processing the signal without multipath (SDR 1) and the CDOs obtained from processing the signal with the induced multipath (SDR 2). In particular, the signal is processed by accumulating 300 code epochs before the CDO generation

PRN	C/N0	f_D Hz
21	49.3 dBHz	-1180.5
17	41.7 dBHz	-2431.2
22	38 dBHz	-71.3

Table 4.2: Estimated values of C/N0 and f_D for different PRNs. Dataset: A.

process. Figure 4.14 shows that the CDO influenced by multipath of the PRN 21 from the dataset A, displays a distinct step in the middle of the rising edge, which is characteristic of multipath effects. Figures 4.15 and 4.16 show the same comparison for signals sampled at 12.5 MHz and 5 MHz, respectively, while considering the same PRN of Figure 4.14. The primary effect of lowering the sampling frequency is a reduction in the slope of the chip edges. The CDO affected by multipath may exhibits a longer rising time compared to those without multipath. The time domain misalignment observed between the CDOs in each figure results from the effect of multipath on the correlation peak. To align the signals in the time domain and position the rising or falling edges in the middle of the chip window, the delay estimate from the correlation peak is utilized.

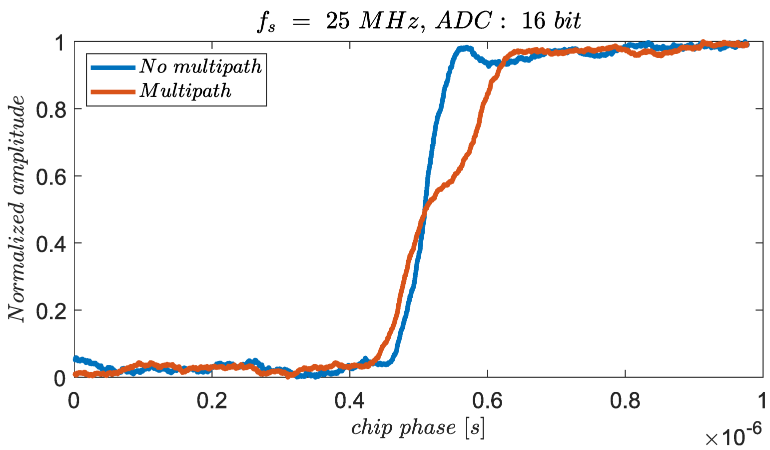

Figure 4.14: CDO comparison. $f_s = 25$ MHz, ADC: 16 bit, $f_D \approx -1180.5\ Hz$, PRN: 21, Sliding mean window: 400 samples, bin width = 1 sample, $T_{acc} = 300\ ms$.

To assess the effect of noise on the CDO in the presence of multipath, Figures 4.17 and 4.18 depict the CDOs derived from processing signals associated with PRN 17 and 22, which have C/N0 values of approximately 41.7 dBHz and 38 dBHz, respectively. Even if the effect of the noise is more evident, particularly in the case of Figure 4.18, the characteristic feature of the multipath is still present and distinguishable.

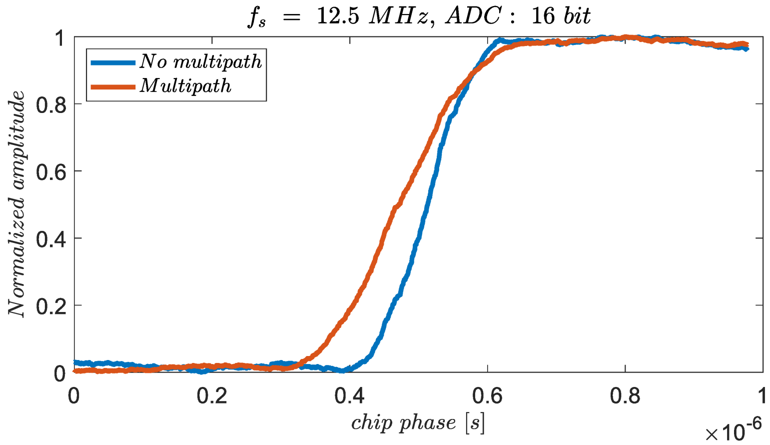

Figure 4.15: CDO comparison. f_s = 12.5 MHz, ADC: 16 bit, $f_D \approx -1294.5\ Hz$, PRN: 21, Sliding mean window: 400 samples, bin width = 1 sample, $T_{acc} = 300\ ms$.

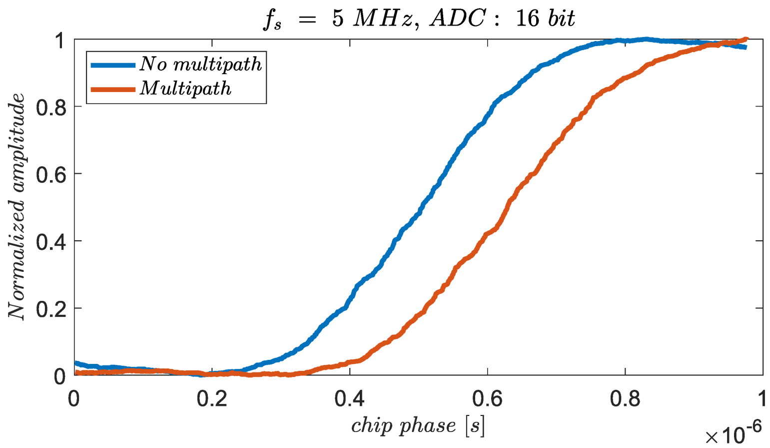

Figure 4.16: CDO comparison. f_s = 5 MHz, ADC: 16 bit, $f_D \approx -1479.5\ Hz$, PRN: 21, Sliding mean window: 400 samples, bin width = 1 sample, $T_{acc} = 300\ ms$.

Figure 4.14 shows an important result, the CDO obtained processing a signal with a sampling frequency of 25 MHz presents a clear and distinguishable feature attributed to the multipath, which can be identified as a sort of step affecting the chip edge. Averaging a relatively small number of code epochs (300), and generating the CDO, enables visualization of the multipath effect, even at lower C/N0 values as illustrated in Figure 4.18. This indicates that the proposed processing technique may enable the analysis of multipath effects on GNSS signals, particularly the GPS C/A signal, even with relatively low sampling frequencies between 25 and 12.5 MHz.

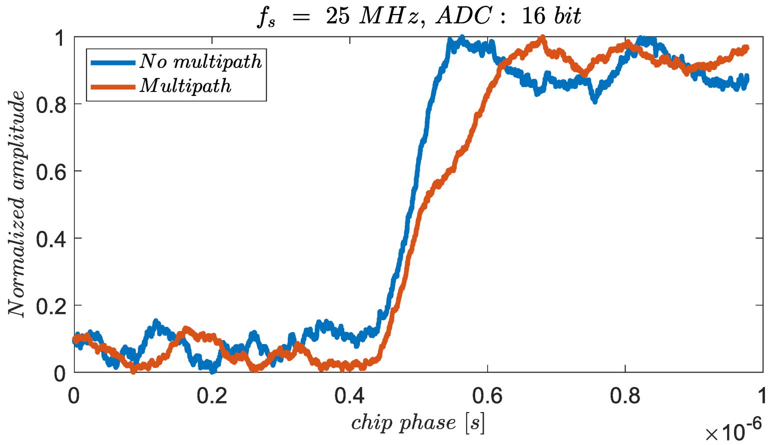

Figure 4.17: CDO comparison. $f_s = 25$ MHz, ADC: 16 bit, $f_D \approx$ 2431.2 Hz, PRN: 17, $C/N0$ $\approx$ 41.7 dBHz, Sliding mean window: 400 samples, bin width = 1 sample, T_{acc} = 300 ms.

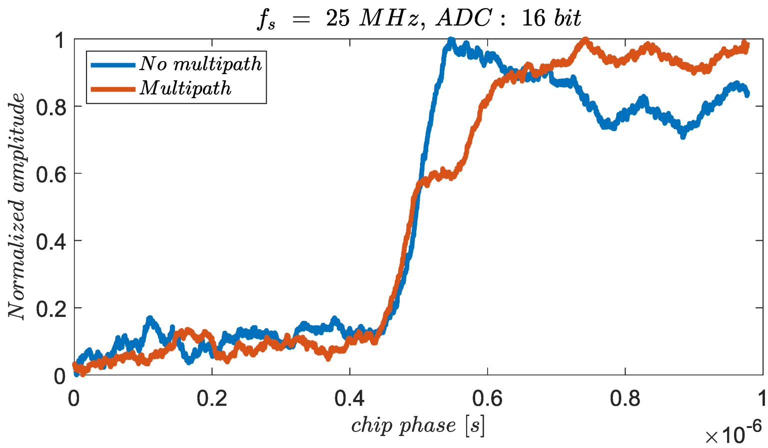

Figure 4.18: CDO comparison. $f_s = 25$ MHz, ADC: 16 bit, $f_D \approx$ -71.3 Hz, PRN: 22, $C/N0$ $\approx$ 38 dBHz, Sliding mean window: 400 samples, bin width = 1 sample, T_{acc} = 300 ms.

4.5 Method for CDO Analysis

The results obtained in section 4.4 highlights how the multipath affects the chip transitions. When the typical step-like features introduced by the delayed signal replica, as shown in figure 4.15, are not observable, the first derivative of the chip edges may still display a lower slope, resulting in a longer rise time. To evaluate signal distortion, in this thesis, it is proposed to study the estimate of the first derivative of the CDO, denoted as $\hat{D}$. Specifically, $\hat{D}$ is obtained by calculating the sliding mean of the forward finite difference of samples of CDO(t). The forward finite difference of a discrete signal $f[n]$ is defined as:

$$\Delta f[n] = f[n+1] - f[n] \tag{4.1}$$

The CDOs computed on different time windows may present some differences, for this reason the CDO is considered as CDO(W), where W is the signal observation window utilized to obtain the observable. To empathize the dependence of $\hat{D}$ on the CDO, in this work, $\hat{D}$ can be expressed as a function of the specific CDO from which it was derived, denoted as $\hat{D}(CDOx)$.

The sliding mean window Win_D utilized to smooth the forward finite difference is set to $0.025 \cdot T_{chip}$. This value should strike a reasonable balance between smoothing the forward finite difference and maintaining a good dynamic range of the resulting observable. Table 4.3 provides a description of the parameters associated with the generation of the CDOs utilized in this section. This description applies to both multipath and multipath-free CDOs. When dealing with the version of the CDO affected by multipath it is referred to as CDOxxM.

CDO	**PRN**	**CDO Sliding mean window [samples]**	**Code averaging bin width [samples]**	T_{acc} **[ms]**
A1	21	400	1	300
A2	17	400	1	300
A3	22	400	1	300
A4	21	400	1	1000

Table 4.3: Description of the parameters selected for the generation of the CDO, obtained processing the dataset A.

Figures 4.19, 4.20, and 4.21 shows how different values of Win_D impact $\hat{D}(CDOA2)$, depicting evaluations obtained with sliding mean windows of $0.015 \cdot T_{chip}$, $0.025 \cdot T_{chip}$, and $0.05 \cdot T_{chip}$, respectively. These evaluations are conducted on the multipath-free version of the CDO A2 shown in Figure 4.17.

To evaluate the distortion of the CDO, the quantity $\hat{D}$, can be compared with a model. The considered model should account for the effects of the filtering of the specific receiver setup utilized for the signal recording. The proposed implementation involves fitting a curve to the estimate $\hat{D}$ obtained from a signal with reduced noise, sampled using a specific receiver setup. By accumulating the signal for an extended period, in this case, one second, a result with minimal noise is achieved, this CDO is labelled as A4. Figure 4.22 shows $\hat{D}(CDO\ A4)$ in green and the fitted curve $\bar{D}(CDO\ A4)$ in blue, obtained by fitting $\hat{D}(CDO\ A4)$ with a Gaussian fit using five Gaussian curves. This fitting technique should help to avoid

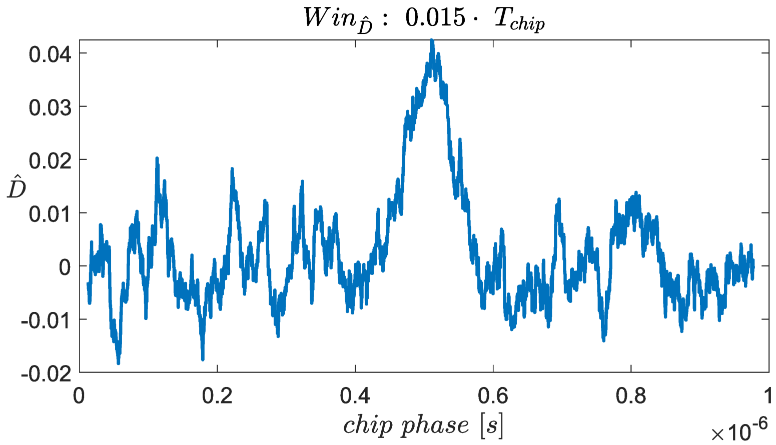

Figure 4.19: $\hat{D}$: forward finite difference of the CDO A2, smoothed with a sliding mean with window Win_D : $0.015 \cdot T_{chip}$.

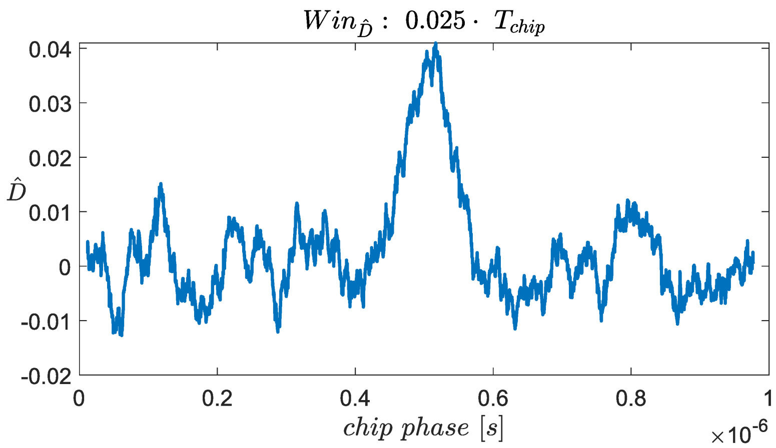

Figure 4.20: $\hat{D}$: forward finite difference of the CDO A2, smoothed with a sliding mean with window Win_D : $0.025 \cdot T_{chip}$.

overfitting and keep the implementation simple. It is important to remark that the observation window utilized to obtain $\bar{D}(W_{\bar{D}})$ can be different from the observation window utilized to estimate $\hat{D}(W_{\hat{D}})$, with $W_{\bar{D}} \neq W_{\hat{D}}$. In the time between the two observation windows, for instance, the receiver front end may present a different transfer function due to some kind of instability, but in any case, the model $\bar{D}(W)$ may present some modeling error $\bar{\delta}(W)$. So the expression of the model becomes:

$$\bar{D}(W_{\bar{D}}) = D_0(W_{\bar{D}}) + \bar{\delta}(W_{\bar{D}}) \tag{4.2}$$

where D_0 is the distortion-free and noiseless forward finite difference filtered by the receiver front end.

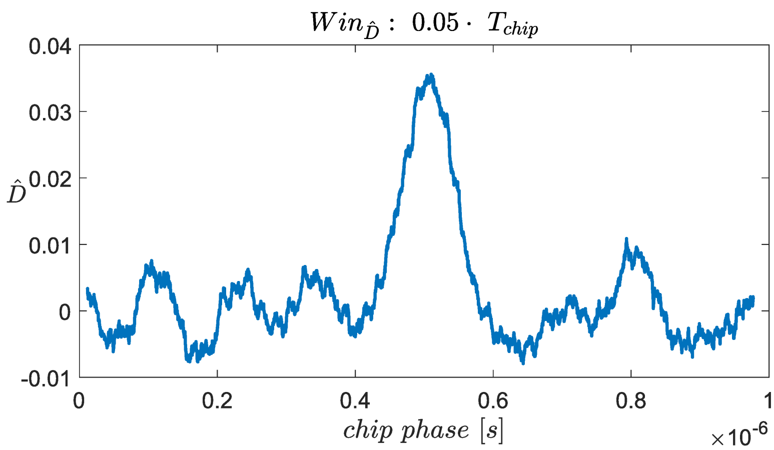

Figure 4.21: $\hat{D}$: forward finite difference of the CDO A2, smoothed with a sliding mean with window Win_D : $0.05 \cdot T_{chip}$.

As observed in Figure 4.22, $\bar{D}(CDO\ A4)$ captures key features of the CDO such as the slope of the rising edge and the small overshoot. Outside the chip transition region, the model $\bar{D}$ is zero.

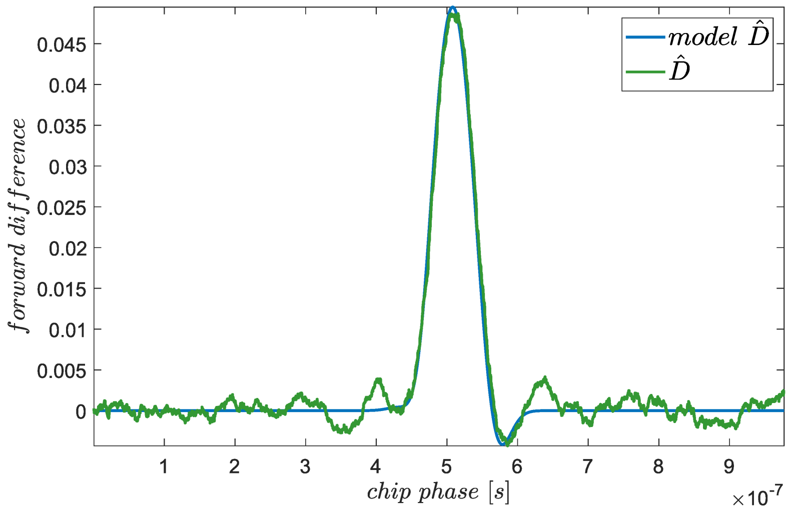

Figure 4.22: Comparison between the model $\bar{D}(CDO\ A4)$ and $\hat{D}(CDO\ A4)$. CDO A4, multipath-free.

To compare the estimated $\hat{D}$ with the model $\bar{D}$ it is possible to perform an analysis of the residual. The expression $\hat{D}$, under the hypothesis of a distortion-free signal, can be written as:

$$\hat{D}(W) = D_0(W) + N_D(W) \tag{4.3}$$

where $N_D(W)$ is a noise component affecting $\hat{D}(W)$. It is then possible to obtain the residual in the following manner:

$$R(W) = D_0(W) + N_D(W) - \bar{D}(W_{\bar{D}}) = D_0(W) + N_D(W) - D_0(W_{\bar{D}}) - \bar{\delta}(W_{\bar{D}}) \tag{4.4}$$

Under the assumption of a stable receiver, so that $D_0(W) \approx D_0(W_{\bar{D}})$, then:

$$R(W) = D_0(W) + N_D(W) - D_0(W_{\bar{D}}) - \bar{\delta}(W_{\bar{D}}) \approx N_D(W) - \delta(\bar{W}) \tag{4.5}$$

When also the distortion is present the expression of $\hat{D}(W)$ becomes:

$$\hat{D}_M(W) = D_0(W) + M(W) + N_D(W) \tag{4.6}$$

where M is the distortion. The residual, in presence of distortion, and assuming to have a stable receiver becomes:

$$R_M(W) = D_0(W) + M(W) + N_D(W) - \bar{D}(W_{\bar{D}}) \approx M(W) + N_D(W) - \bar{\delta}(W) \tag{4.7}$$

As a consequence:

$$R_M(W) \neq R(W) \tag{4.8}$$

The expression 4.7 indicates that the residual in presence of multipath is different from the multipath-free residual reported in the expression 4.5, so it may exhibit different statistical properties, especially of the distortion M is particularly pronounced. From now on, for simplicity, it is assumed that the properties of the receiver remain stable over time. Assuming that multipath introduces distortions only in a specific portion of the CDO near the chip transition, between two chip phases t_1 and t_2, the properties of the residuals within this window can be compared to those outside of it.

Figures 4.23 and 4.24 present a comparison between the model $\bar{D}$, $\hat{D}$, and the residuals. The first figure shows the multipath-free case, while the second figure illustrates the case with multipath. The CDO analyzed in this case is CDO A1. The Figures 4.23 and 4.24, show that by estimating the standard deviation of the residual outside the chip transition window between t_1 and t_2, denoted as σ, and setting two thresholds at $\sigma \cdot k$ and $-\sigma \cdot k$, it is possible to identify outliers in the case of CDO A1M, indicating the presence of multipath. For all comparisons, the threshold is set to $\sigma \cdot k$ with $k = 3$, while $t_1 = 0.35 \cdot T_{chip}$ and $t_2 = 0.7 \cdot T_{chip}$. However, defining an adequate threshold and, more generally, designing a detector is the subject of future work. This may include a more comprehensive analysis of

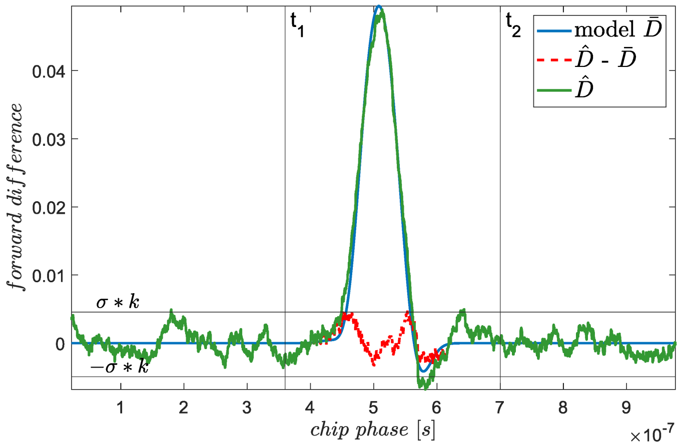

Figure 4.23: Comparison between $\hat{D}$, $\bar{D}$ and the residual. CDO A1

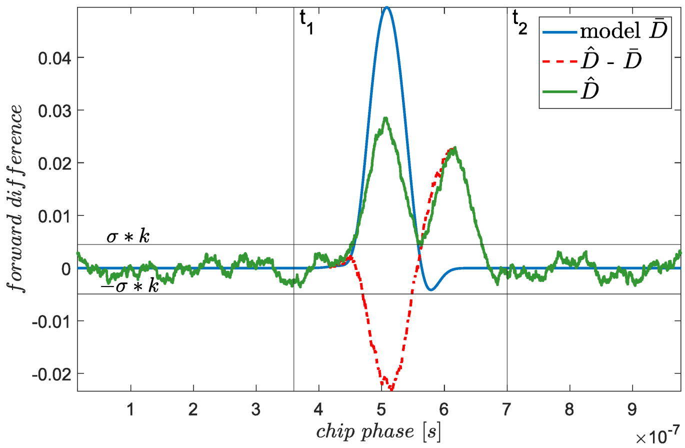

Figure 4.24: Comparison between $\hat{D}$, $\bar{D}$ and the residual when multipath is present. CDO A1M, multipath.

the behavior of signals affected by multipath, under different conditions, and using various multipath models.

This technique seems to be capable of enhancing the observability of the multipath distortion, also for lower values of $C/N0$.

Figures 4.25 and 4.26 present the same residual comparison but consider CDOs A2/A2M, which are derived from a signal with a lower C/N0 of approximately 41.7 $dBHz$.

The residual evaluation is also performed for CDOs A3/A3M, which have an even lower C/N0 of approximately 38 $dBHz$. This is shown in Figures 4.27 and

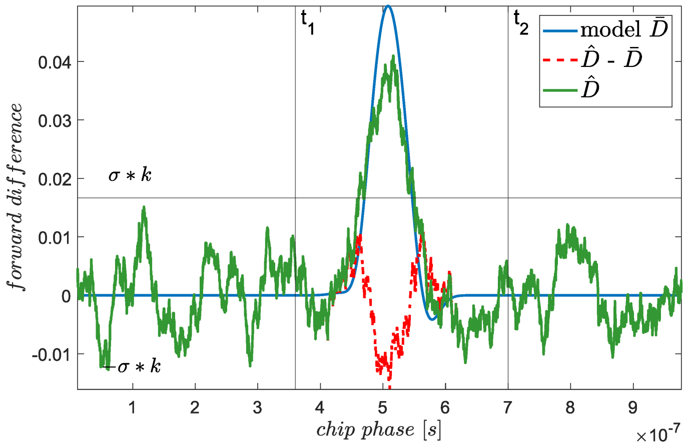

Figure 4.25: Comparison between $\hat{D}$, $\bar{D}$ and the residual. CDO A2

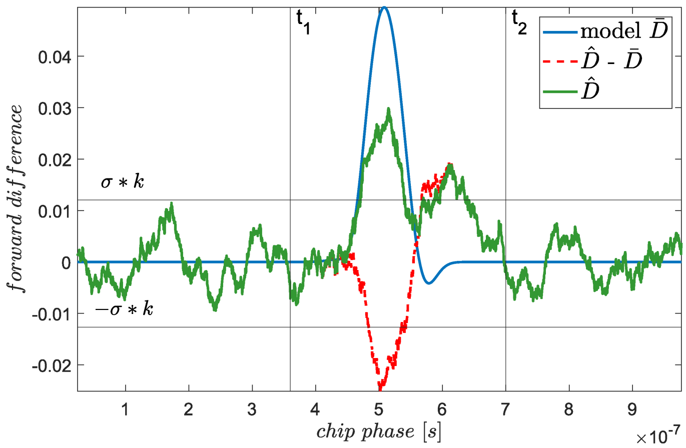

Figure 4.26: Comparison between $\hat{D}$, $\bar{D}$ and the residual. CDO A2M, multipath.

4.28, respectively.

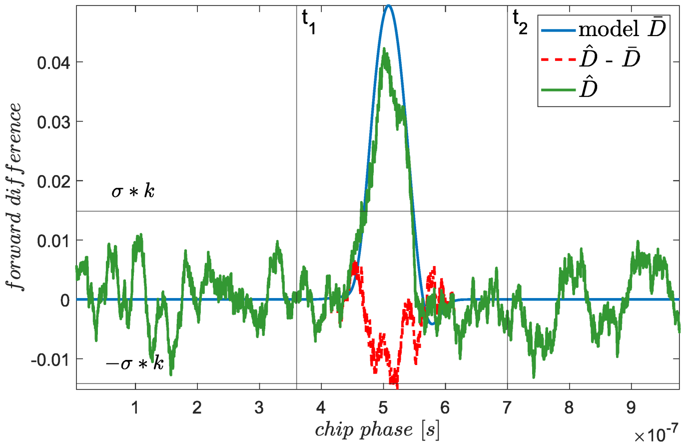

Figure 4.27: Comparison between $\hat{D}$, $\bar{D}$ and the residual. CDO A3.

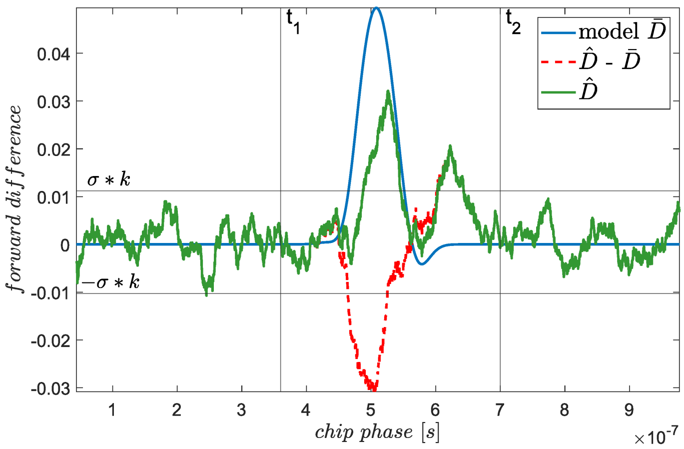

Figure 4.28: Comparison between $\hat{D}$, $\bar{D}$ and the residual. CDO A3M, multipath.

Chapter 5

Conclusions

This thesis has investigated techniques from the literature aimed at monitoring signal quality to enhance the observability of GNSS signals. The primary focus was on implementing an averaging technique to reduce noise effects on the signal. The necessity to evaluate the integrity of transmitted signals and possible distortions under extreme conditions (high Doppler dynamics, low C/N0) was emphasized throughout the study.

This study revisited several techniques and identified key adjustments to make them suitable for challenging conditions, such as high Doppler dynamics and low carrier-to-noise ratios. The research highlighted the gap between traditional signal acquisition techniques and those investigated for analyzing the physical structure of the signal.

The thesis specifically addressed multipath effects through experimental analysis, revealing the conditions that favor the identification of these phenomena. Notably, higher sampling frequencies (between 12.5 and 25 MHz) resulted in a clearer visualization of multipath effects. In this case, the multipath consisted of a two-ray model with one signal copy delayed by 25 meters and attenuated.

The study further expands the observation of chip transitions using a differential methodology that emphasizes the effects of multipath, demonstrating the effectiveness in detecting this phenomenon. The results show that the employed techniques and proposed improvements can be scientifically used to assess the physical integrity of GNSS signals through sample captures planned for the LuGRE mission.

Future work may concentrate on studying the obtained chip domain observable in the presence of signal distortions. Specifically, further research could develop methods to detect and identify the nature of these distortions and potentially measure their magnitude. This advancement could significantly improve the robustness and accuracy of GNSS signal monitoring and quality assessment, and it may help to characterize the signal in harsh environments.

Appendix A

References

[1] R Eric Phelts, Gabriel Wong, Todd Walter, and Per Enge. «Signal deformation monitoring for dual-frequency WAAS». In: *Proceedings of the 2013 International Technical Meeting of The Institute of Navigation*. 2013, pp. 93–106 (cit. on pp. iii, 28).

[2] Esper Mark, Chao Elaine, and Wolf Chad. *2019 Federal Radionavigation Plan*. Tech. rep. United States. Department of Defense, 2019, p. 221 (cit. on p. 1).

[3] *Celebrating the GPS 50th Anniversary: Recommitting to U.S. Leadership in PNT*. White Paper. NATIONAL SPACE-BASED POSITIONING, NAVIGATION, and TIMING ADVISORY BOARD, May 2023 (cit. on p. 2).

[4] Gregory D McLaughlin. *The commercialization of the global positioning system*. Tech. rep. Air Command and Staff College, 1997 (cit. on p. 2).

[5] Hecker, Bestmann, Schwithal, and Stanisak. *Galileo Satellite Navigation System: Space applications on earth*. Tech. rep. Panel for the Future of Science and Technology (STOA), 2018, p. 16 (cit. on p. 2).

[6] European Global Navigation Satellite Systems Agency (EUSPA). *EUSPA EO and GNSS Market Report*. Tech. rep. 2024 (cit. on p. 2).

[7] *Galileo Open Service Service Definition Document*. European Space Agency, Nov. 2023 (cit. on p. 3).

[8] *GPS official website*. URL: `https://www.gps.gov/systems/gps/space/` (cit. on p. 3).

[9] *BeiDou Navigation Satellite System Open Service Performance Standard*. China Satellite Navigation Office, 2018 (cit. on p. 3).

[10] Kaplan and Hagerthy. *Understanding GPS, Principles and Applications*. Norwood, MA: Artech House, 2006 (cit. on pp. 4, 20).

[11] Jimmy LaMance, Javier DeSalas, and Jani Jarvinen. «Assisted GPS: A low-infrastructure approach». In: *GPS World* 13.3 (2002) (cit. on p. 5).

[12] Timo Kouwenhoven. Jan. 2011. URL: `https://gssc.esa.int/navipedia/images/c/c5/Unknown_Offset4.png` (cit. on p. 8).

[13] Timo Kouwenhoven. Jan. 2011. URL: `https://gssc.esa.int/navipedia/images/4/4a/DOP_effect_in_positioning.png` (cit. on p. 9).

[14] J.M. Juan Zornoza J. Sanz Subirana and M. Hernández-Pajares. *GNSS DATA PROCESSING Volume I: Fundamentals and Algorithms*. ESA, 2013 (cit. on p. 9).

[15] Ignacio Fernandez-Hernandez et al. «Galileo high accuracy service: initial definition and performance». In: *Gps Solutions* 26.3 (2022), p. 65 (cit. on p. 14).

[16] Willard A Marquis and Daniel L Reigh. «The GPS Block IIR and IIR-M broadcast L-band antenna panel: Its pattern and performance». In: *NAVIGATION: Journal of the Institute of Navigation* 62.4 (2015), pp. 329–347 (cit. on p. 17).

[17] NASA. *NASA Explores Upper Limits of Global Navigation Systems for Artemis*. Jan. 2021. URL: `https://www.nasa.gov/missions/artemis/nasa-explores-upper-limits-of-global-navigation-systems-for-artemis/` (cit. on p. 18).

[18] Taro Suzuki and Yoshiharu Amano. «NLOS multipath classification of GNSS signal correlation output using machine learning». In: *Sensors* 21.7 (2021), p. 2503 (cit. on p. 20).

[19] AJ Van Dierendonck, Pat Fenton, and Tom Ford. «Theory and performance of narrow correlator spacing in a GPS receiver». In: *Navigation* 39.3 (1992), pp. 265–283 (cit. on pp. 19, 28).

[20] Jason Jones, Pat Fenton, Brian Smith, et al. «Theory and performance of the pulse aperture correlator». In: *Proceedings of ION GPS*. Vol. 2004. 2004 (cit. on p. 19).

[21] Bryan R Townsend, Patrick C Fenton, Keith J Van Dierendonck, and DJ Richard Van Nee. «Performance evaluation of the multipath estimating delay lock loop». In: *Navigation* 42.3 (1995), pp. 502–514 (cit. on p. 19).

[22] Lawrence Weill. «Achieving theoretical accuracy limits for pseudoranging in the presence of multipath». In: *Proceedings of the 8th International Technical Meeting of the Satellite Division of the Institute of Navigation (ION GPS 1995)*. 1995, pp. 1521–1530 (cit. on p. 19).

[23] B Rama Rao. *GPS/GNSS Antennas*. Artech House, 2013 (cit. on p. 21).

[24] Marco Pini and Dennis M Akos. «Exploiting GNSS signal structure to enhance observability». In: *IEEE Transactions on Aerospace and Electronic Systems* 43.4 (2007), pp. 1553–1566 (cit. on p. 21).

[25] Anupam Kumari and Darshak Bhatt. «Advanced system analysis and survey on the GPS receiver front end». In: *IEEE Access* 10 (2022), pp. 24611–24626 (cit. on p. 21).

[26] Robert Eric Phelts. *Multicorrelator techniques for robust mitigation of threats to GPS signal quality*. Stanford University, 2001 (cit. on pp. 26, 28, 42).

[27] Clyde Edgar, Frank Czopek, and Brian Barker. «A co-operative anomaly resolution on PRN-19». In: *Proceedings of the 12th International Technical Meeting of the Satellite Division of The Institute of Navigation (ION GPS 1999)*. 1999, pp. 2269–2268 (cit. on p. 26).

[28] A. M. Mitelman. «Signal quality monitoring for GPS augmentation systems». PhD thesis. Stanford, CA: Stanford University, Dec. 2004. URL: `https://www.proquest.com/docview/305440473?pq-origsite=gscholar&fromopenview=true&sourcetype=Dissertations%20&%20Theses` (cit. on pp. 27, 28, 32, 33, 36, 37, 51).

[29] A. Ndili. «Robust GPS Autonomous Signal Quality Monitoring.» PhD thesis. Stanford, CA, Aug. 1998. URL: `https://web.stanford.edu/group/scpnt/gpslab/pubs/theses/AweleNdiliThesis98.pdf` (cit. on p. 27).

[30] A Jakab. «An approach to GPS satellite failure detection». In: *Proceedings of the 12th International Technical Meeting of the Satellite Division of The Institute of Navigation (ION GPS 1999)*. 1999, pp. 751–760 (cit. on p. 27).

[31] Gao, Akos, Walter, and Enge. «Understanding the GIOVE-B broadcast codes of the Galileo system». In: *2008 42nd Asilomar Conference on Signals, Systems and Computers*. IEEE. 2008, pp. 2086–2090 (cit. on p. 28).

[32] Pat Fenton and Jason Jones. «The Theory and Performance of NovAtel Inc.'s Vision Correlator». In: 2005 (cit. on pp. 28, 38).

[33] R Eric Phelts, Todd Walter, and Per Enge. «Characterizing nominal analog signal deformation on GNSS signals». In: *Proceedings of the 22nd International Technical Meeting of The Satellite Division of the Institute of Navigation (ION GNSS 2009)*. 2009, pp. 1343–1350 (cit. on p. 28).

[34] Paul Thevenon, Jean-Baptiste Pagot, Olivier Julien, and Quentin Tessier. «Processing technique and performance of the observation of evil waveform in the chip domain». In: *ESA Navitech 2014, 7th ESA Workshop on Satellite Navigation Technologies*. 2014 (cit. on pp. 28, 30, 43).

[35] Jean-Baptiste Pagot. «Modeling and monitoring of new GNSS signal distortions in the context of civil aviation». PhD thesis. INPT, 2016 (cit. on p. 28).

[36] Xiang Wang, Yang Gao, Xiaowei Cui, Gang Liu, and Mingquan Lu. «A signal quality monitoring algorithm based on chip domain observables for BDS B1C signal». In: *Proceedings of the 2021 International Technical Meeting of The Institute of Navigation*. 2021, pp. 149–161 (cit. on p. 28).

[37] Gabriel Wong, R Eric Phelts, Todd Walter, and Per Enge. «Characterization of signal deformations for GPS and WAAS satellites». In: *Proceedings of the 23rd International Technical Meeting of The Satellite Division of the Institute of Navigation (ION GNSS 2010)*. 2010, pp. 3143–3151 (cit. on pp. 28, 36–38).

[38] Gao, A. Chen, S. Lo, D. De Lorenzo, and P. Enge. «GNSS over China: The Compass MEO Satellites Codes». In: *Inside GNSS* (2007), pp. 36–43 (cit. on p. 28).

[39] Rick Clark. *Real-Time vs. Sampling Oscilloscopes: What Are the Differences?* 2022. URL: `https://www.keysight.com/blogs/en/tech/bench/2022/05/09/real-time-vs-sampling-oscilloscopes-what-are-the-differences` (cit. on p. 33).

[40] Luke M. B. Winternitz, William A. Bamford, and Gregory W. Heckler. «A GPS Receiver for High-Altitude Satellite Navigation». In: *IEEE Journal of Selected Topics in Signal Processing* 3.4 (2009), pp. 541–556. DOI: `10.1109/JSTSP.2009.2023352` (cit. on p. 46).

[41] John Rush. «Current issues in the use of the global positioning system aboard satellites». In: *Acta Astronautica* 47.2-9 (2000), pp. 377–387 (cit. on p. 46).

[42] F. Marmet, Jerome Maureau, M. Calaprice, and J. Aguttes. «GPS/Galileo navigation in GTO/GEO orbit». In: *Acta Astronautica* 117 (2015), pp. 263–276. DOI: `10.1016/J.ACTAASTRO.2015.08.008` (cit. on p. 46).

[43] Eberhard Gill, Jade Morton, Penina Axelrad, Dennis M Akos, Marianna Centrella, and Stefano Speretta. «Overview of space-capable global navigation satellite systems receivers: heritage, status and the trend towards miniaturization». In: *Sensors* 23.17 (2023), p. 7648 (cit. on p. 46).

[44] Mitra Farahmand, Anne Long, and Russell Carpenter. «Magnetospheric multiscale mission navigation performance using the goddard enhanced onboard navigation system». In: *Proceedings of the 25th International Symposium on Space Flight Dynamics*. 2015, pp. 19–23 (cit. on p. 46).

[45] Luke B Winternitz, William A Bamford, Samuel R Price, J Russell Carpenter, Anne C Long, and Mitra Farahmand. «Global positioning system navigation above 76,000 km for NASA's magnetospheric multiscale mission». In: *NAVIGATION: Journal of the Institute of Navigation* 64.2 (2017), pp. 289–300 (cit. on p. 47).

[46] Luke B Winternitz, William A Bamford, and Samuel R Price. «New high-altitude GPS navigation results from the magnetospheric multiscale spacecraft and simulations at Lunar distances». In: *Proceedings of the 30th International Technical Meeting of The Satellite Division of the Institute of Navigation (ION GNSS+ 2017)*. 2017, pp. 1114–1126 (cit. on p. 47).

[47] Alex Minetto, Fabio Dovis, Andrea Nardin, Oliviero Vouch, Gabriele Impresario, and Mario Musmeci. «Analysis of GNSS data at the Moon for the LuGRE project». In: *2022 IEEE 9th International Workshop on Metrology for AeroSpace (MetroAeroSpace)*. IEEE. 2022, pp. 134–139 (cit. on pp. 47, 48).

[48] Joel JK Parker et al. «The lunar gnss receiver experiment (lugre)». In: *Proceedings of the 2022 International Technical Meeting of The Institute of Navigation*. 2022, pp. 420–437 (cit. on p. 47).

[49] *National Aeronautics and Space Administration (NASA)*. Accessed: July 2024. 2024. URL: `https://www.nasa.gov/` (cit. on p. 47).

[50] *Agenzia Spaziale Italiana (ASI)*. Accessed: July 2024. 2024. URL: `https://www.asi.it/` (cit. on p. 47).

[51] *Quascom*. Accessed: July 2024. 2024. URL: `https://www.qascom.it/` (cit. on p. 47).

[52] NavSAS Group. *Navigation Signal Analysis and Simulation (NavSAS) Group*. URL: `%5Curl%7Bhttps://navsas.polito.it/%7D` (cit. on p. 47).

[53] Firefly Aerospace. *Blue Ghost*. `https://fireflyspace.com/blue-ghost/`. Accessed: July 2024. 2024 (cit. on p. 47).

[54] Vincenzo Capuano, Cyril Botteron, and Pierre-André Farine. «Gnss performances for meo, geo and heo». In: *Space Communications and Navigation Symposium-Space-Based Navigation Systems and Services*. 2013 (cit. on pp. 48, 49).

[55] Zheng Chenggong, Chen Xi, and Huang Zhen. «A comprehensive analysis on Doppler frequency and Doppler frequency rate characterization for GNSS receivers». In: *2016 2nd IEEE International Conference on Computer and Communications (ICCC)*. IEEE. 2016, pp. 2606–2610 (cit. on pp. 49, 50, 57).

[56] Salvatore Guzzi. «Study of high sensitivity GNSS receivers for space applications and lunar missions». PhD thesis. Politecnico di Torino, 2022 (cit. on p. 50).

[57] Chun Yang, Mikel Miller, Erik Blasch, and Thao Nguyen. «Comparative study of coherent, non-coherent, and semi-coherent integration schemes for GNSS receivers». In: *Proceedings of the 63rd Annual Meeting of The Institute of Navigation (2007)*. 2007, pp. 572–588 (cit. on p. 51).

[58] Myriam Foucras, Olivier Julien, Christophe Macabiau, and Bertrand Ekambi. «Detailed analysis of the impact of the code Doppler on the acquisition performance of new GNSS signals». In: *Proceedings of the 2014 International Technical Meeting of The Institute of Navigation*. 2014, pp. 513–524 (cit. on p. 56).

[59] Margherita Mariani. «Study of high sensitivity GNSS receivers for space applications and lunar missions». PhD thesis. Politecnico di Torino, 2021 (cit. on p. 57).

[60] Emanuela Falletti, Davide Margaria, Mario Nicola, Gabriella Povero, and Micaela Troglia Gamba. «N-FUELS and SOPRANO: Educational tools for simulation, analysis and processing of satellite navigation signals». In: *2013 IEEE Frontiers in Education Conference (FIE)*. 2013, pp. 303–308. DOI: 10.1109/FIE.2013.6684836 (cit. on p. 68).

[61] Iman Ebrahimi Mehr, Alex Minetto, Fabio Dovis, Emanuele Pica, Claudio Cesaroni, and Vincenzo Romano. «An Open Architecture for Signal Monitoring and Recording Based on SDR and Docker Containers: A GNSS Use Case». In: *IEEE EUROCON 2023-20th International Conference on Smart Technologies*. IEEE. 2023, pp. 66–71 (cit. on pp. 73, 75).